Practical Implementation of Dosimetry for Patients with Thyroid Carcinoma Undergoing I-131 Therapy

A thesis submitted to The University of Manchester for the degree of Doctor of Clinical Science in the Faculty of Biology, Medicine and Health

2021

Fiona H. Barrack

School of Medical Sciences

Contents

The final word count, including footnotes and endnotes: 36,404

List of Figures

List of Tables

List of Abbreviations

AC	Attenuation correction
ARSAC	Administration of Radioactive Substances Advisory Committee
Bq	Becquerel, unit denoting number of radioactive decays per second
CDR	Collimator detector response
Cps	Counts per second
CT	Computed tomography
EANM	European Association of Nuclear Medicine
EMA	European Medicines Agency
ESSE	Effective scatter source estimation
FM	Fast mode, used for high count rate gamma camera acquisitions
FOV	Field of view
FWHM	Full width at half maximum height
HEGP	High energy general purpose
I-123	Iodine-123
I-131	Iodine-131
IDUG	Internal Dosimetry User Group
IR(ME)R	Ionising Radiation (Medical Exposure) Regulations 2017
MIRD	Medical Internal Radiation Dose Committee
NaI	Sodium iodide
NM	Normal mode, used for standard count rate gamma camera acquisitions
NPL	National Physical Laboratory
NURBS	Non-uniform rational B-splines
PMT	Photomultiplier tube
PV	Partial volume
PVC	Partial volume correction
PVE	Partial volume effect
RC	Recovery coefficient
RMSE	Root mean squared error
ROI	Region of interest
RR	Resolution recovery
SC	Scatter correction

Sn-113	Tin-113
SPECT	Single photon emission computer tomography
TEW	Triple energy window
TSH	Thyroid stimulating hormone
VOI	Volume of interest

Abstract

Radioactive iodine (I-131) is used to treat patients with thyroid cancer. Currently the patient radiation dose received from these therapies is not routinely calculated but could be used to optimise treatments and improve patient outcomes [1], [2]. This work investigated methods given in literature for performing dosimetry that would practical to implement clinically, applied to the systems at Royal Surrey County Hospital (RSCH).

The bone marrow is most at risk of damage from the radiation, limiting I-131 activity administered. Dosimetry for this organ requires measurements of whole body I-131 retention to calculate its residence time within the body. The impact of different whole body measurement methods was investigated using data from 39 patients, including a comparison of geometric mean and anterior measurements, background correction methods and impact of a late time point measurement at 7 days post therapy.

The doses to target tissues are calculated using gamma camera images, with calibrations required to allow I-131 activity quantification. Published methods of calibration were investigated for the GE Optima 640 gamma camera at RSCH using I-131 "fast" counting mode. A non-paralysable deadtime of 6.91±0.08μs was measured using planar triple energy window (TEW) corrected images of a large cylindrical phantom with 20 to 2800MBq I-131. The optimal OSEM reconstruction using the GE Volumetrix was found to be 60 iterations, 10 subsets, no filter with TEW and CT attenuation correction using cylinders with 7.5-60mm diameters. SPECT sensitivity of 22.3±0.9cps/MBq was measured using a large cylindrical phantom and volume of interest. Partial volume correction (PVC) curves were investigated using spheres and cylinders, with spheres scanned individually and a sigmoidal fit with no plateau constraint found to be optimal. Work was performed to characterise the "fast" mode and significant differences were seen with low deadtime sensitivity and PVC curves compared to normal mode.

A method for external validation of the tumour dosimetry process was developed in conjunction with the National Physical Laboratory. 13ml spheres were imaged with activities corresponding to different time points for a tumour biokinetic model. A 13% overestimation of dose was seen compared to a Monte Carlo ground truth, primarily due to errors with PVC at low volumes. Further areas for development of this dosimetry validation technique were identified and this could be used to provide assurance for centres performing dosimetry and harmonise procedures. Through this innovative work a practical method for performing dosimetry has been developed which once implemented will enable radiation doses to be calculated and treatments optimised for patients.

Declaration

No portion of the work referred to in the thesis has been submitted in support of an application for another degree or qualification of this or any other university or other institute of learning

Copyright

Acknowledgements

I would first like to thank my professional doctorate supervisors James Scuffham and Jennie Prince for their invaluable support and guidance during this process. I am particularly grateful for all the assistance that James has provided, your insightful feedback and suggestions are really appreciated.

I would also like to thank Ana Denis-Bacelar and all the staff at the National Physical Laboratory who have provided the assistance which enabled the dosimetry validation aspect of this project to be performed.

To my colleagues in Nuclear Medicine Physics at Royal Surrey County Hospital, thank you so much for your support and giving me time to focus on HSST work. Everyone has been overstretched during this pandemic and I am incredibly grateful.

Finally huge thanks to my husband Nick, HSST has been a long and stressful process and I appreciate your support and encouragement.

1. Introduction

1.1. Overview

In the UK around 3,700 new cases of thyroid cancer are diagnosed every year and the incidence is increasing, with a reported 164% rise since the early 1990s [3]. Of these cases, around 90% are differentiated thyroid cancers [4], which are typically treated with surgery followed by I-131 NaI (radioactive iodine) radionuclide therapy [5]. This treatment has been routine clinical practice for more than 70 years and is one of the most common treatments within the UK involving radioactivity [6]. Normal and differentiated thyroid cancer cells accumulate iodine for the production of thyroid hormones [7], [8]. I-131 has highly ionising beta emissions which can be used to kill remaining thyroid cells following surgery, along with high energy gamma emissions which can be used to image the distribution of uptake using a gamma camera [9].

Within the UK, standard therapy activities of 1.1GBq and 3.7MBq of I-131 are typically given to low and high risk ablation patients respectively, while 5.5GBq is administered for repeat therapy treatments [5], [10]. More individually tailored activities are not used due to a lack of evidence on the optimal method to use [5], [10], however an audit at Royal Surrey County Hospital (RSCH) found around 35% patients require retreatments. There is a lack of randomised control trials investigating empirical and personalised activity administrations [11]. However, as large variations in both thyroid and bone marrow absorbed dose is seen [12], [13] there is a strong theoretical basis for moving away from the one size fits all approach [1]. To gain evidence for how to tailor treatments, knowledge of the radiation dose that patients actually received and the impact of the treatment is needed [2].

Dosimetry involves the calculation of radiation dose received to target tissues and organs at risk of damage from radiation. However, it is not commonly performed for thyroid carcinoma patients and there is no consensus on the best method for practically performing it [2]. Radiation legislation requiring dosimetry for radiotherapeutic exposures, implemented in the UK in 2017 [14], [15] also gives increased incentive to start performing dosimetry.

There are a number of guidelines published for performing dosimetry [16]–[23], however they frequently give different recommendations and often require the use of complex specialist software. A 2017 survey of radionuclide therapy practice within Europe found a shortage of knowledge to be one of the main limiting factors for patient specific

dosimetry [24]. A 2020 IPEM topical report into the UK molecular radiotherapy service provision found 88% of centres were not performing MRTDosimetry and found “lack of clinical evidence”, a “lack of guidelines”, “not current UK practice”, “lack of software” and “lack of staff training/expertise” to be the main reasons sites stated for not performing dosimetry [6]. Therefore the motivation of this work was to assess practical methods of performing dosimetry within a standard hospital setting for patients undergoing I-131 NaI therapy for thyroid cancer.

At the start of this work an innovation proposal was performed assessing the different options for performing dosimetry (see Appendix 2). This found the cost for software to perform voxel level dosimetry was prohibitively expensive given the current reimbursements for these therapies. Therefore this work will focus on organ level dosimetry.

The aims of this work are given in Chapter 1.4 and a discussion regarding the legislative requirement for radiotherapeutic dosimetry is given in Chapter 2.1. A brief introduction to molecular radiotherapy dosimetry is given in Chapter 1.2 and an introduction to gamma camera quantitative imaging is given in Chapter 1.3. A literature review focussing on practical methods for performing dosimetry and areas for further research is given in Chapter 2, for each key area. There is a vast amount of literature published on performing dosimetry and a full review of all methods would be outside of the scope of a single Professional Doctorate. Therefore, this work has focussed on published guidelines and methods that may be practical to implement. Gamma camera imaging calibrations performed for I-131 dosimetry imaging are described in Chapter 4 with subsections for deadtime, SPECT reconstruction, sensitivity, partial volume correction and tumour S-factors. As each subsection builds upon the results from the previous one the methods, results and discussion are grouped for each subsection. Investigations of whole body residence time measurement methods and blood sampling calibrations were performed for use in bone marrow dosimetry and are given in Chapter 3. Details of the planned dosimetry procedure based on research work performed is given in Chapter 5 and external validation of the procedure is given in Chapter 6.

1.2. Dosimetry Introduction

For therapies involving the administration of radioactivity (molecular radiotherapies) the absorbed dose to a target tissue at time t, $D(r_T, t)$, depends the dose rate $\dot{D}(r_T, t)$ as

given in Equation 1. The dose rate depends on the energy deposited per unit mass from the target and surrounding tissues and will change over the assessment time period, T_D, due to redistribution of the radioactivity and radioactive decay.

$$D(r_T, T_D) = \int_0^{T_D} \dot{D}(r_T, t)dt \qquad (1)$$

The Medical Internal Radiation Dose (MIRD) Committee suggest that absorbed dose can be calculated from radionuclide specific S-factors, $S(r_T \leftarrow r_{s,}, t)$ and the time integrated activity ($\tilde{A}(r_s, t)$), as given in Equation 2 [25].

$$D(r_T, t) = \sum_{r_s} \int_0^{T_D} A(r_s, t)\, S(r_T \leftarrow r_{s,}, t)dt = \sum_{r_s} \tilde{A}(r_s, t)\, S(r_T \leftarrow r_{s,}, t)dt \qquad (2)$$

The time integrated activity can be determined either through patient measurements, knowledge of the population biokinetics, or a combination of both. The S-factors represent the time dependent dose rate from the radiation source, r_s, in tissue r_T and the dose is calculated by summing the contribution from all source tissues. A schematic diagram is given in Figure 1. S-factors depend on the mass of the target tissue, $M(r_T, t)$; mean energy of the ith nuclear transition, E_i; number of ith transmissions per decay, Y_i and; fraction of radiation emitted energy from the source tissue absorbed with the target tissue, $\phi(r_T \leftarrow r_{s,}, E_i\,, t)$; as given in Equation 3 [25].

$$\begin{aligned} S(r_T \leftarrow r_{s,}, t) &= \frac{1}{M(r_T, t)} \sum_i E_i Y_i \phi\left(r_T \leftarrow r_{s,}, E_i\,, t\right) \\ &= \frac{1}{M(r_T, t)} \sum_i \Delta_i \phi\left(r_T \leftarrow r_{s,}, E_i\,, t\right) = \sum_i \Delta_i \Phi\left(r_T \leftarrow r_{s,}, E_i\,, t\right) \end{aligned} \qquad (3)$$

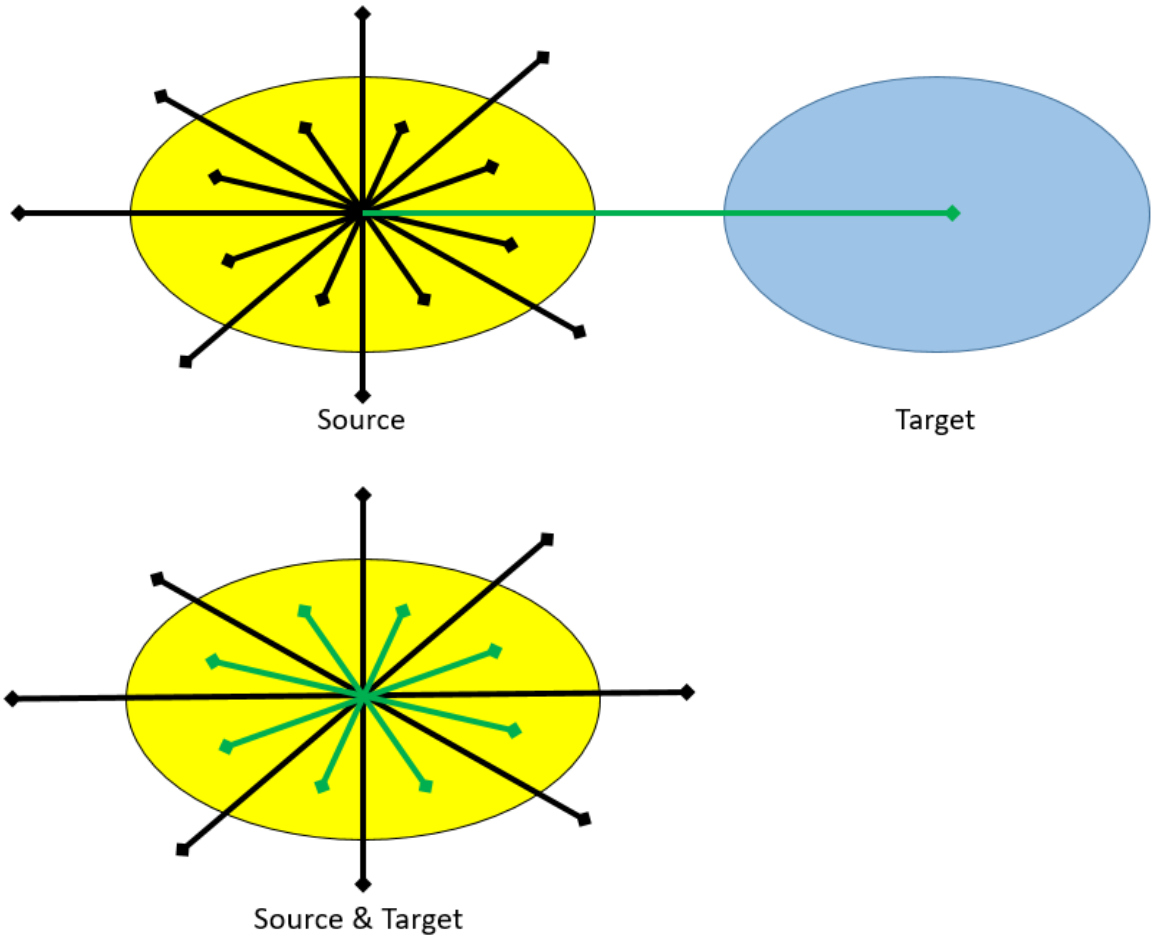

Figure 1.S-factor schematic diagram. A fraction of the radiation emitted from a source tissue during radioactive decay is absorbed by the target tissue. Shown for where the target and source are separate (top) and where target and source are the same tissue (bottom).

S-factors are typically calculated using Monte Carlo models, varying from a single sphere to model self-absorbed dose, to whole body computational phantoms for different ages and genders, to segmented images based on anatomical imaging [26]–[28]. Further discussion of S-factor models is given in Chapter 2.5 in the literature review.

For more patient specific dose calculations, voxel-based dosimetry using patient images and techniques such as Monte Carlo modelling or the less computationally intensive dose-point kernel convolution can be used. With the dose point-kernel method, quantitative patient image is convolved with a kernel representing the dose from a point source of the radionuclide, which is typically derived from Monte Carlo simulations [29]. There is now a range of software commercially available for performing voxel level dosimetry [6] and both types of methods are used. For example, Hermes have developed a semi-Monte Carlo method in which electrons are assumed to be absorbed locally and accelerated Monte Carlo simulation is used for photon transport [30]. Alternatively QDOSE® (ABX-CRO advanced pharmaceutical) and PLANET®Dose (Dosisoft) use the dose point kernel method [31]. The non-uniform distribution of uptake in a tumour can result

in some areas being over treated and others being undertreated. These voxel-based patient specific dosimetry methods can allow cumulative dose volume histograms to be computed, allowing the dose distribution to be assessed. However as voxel based dosimetry requires complex specialist software which is not available in many sites, it will not be considered further in this work.

The bone marrow is the organ within the body which may be most easily damaged by radioactivity administered systemically [20]**.** Therefore, the dose it receives is typically the limiting factor for the maximum activity that can be administered for radioiodine therapies [20]. Based on the work by Benua at al., a 2Gy limit to the blood/bone marrow is commonly used to minimise haematological complications after I-131 therapy [21], [32]. However, other studies suggest that the absorbed dose to tumour or lesions can be used to predict response and hence optimum activity to administer [33]–[35]. Therefore, this work focusses on the measurement of dose to the blood and bone marrow, as well as lesion-based dosimetry using gamma camera imaging. It is possible to perform dosimetry using PET/CT imaging with I-124. which has the advantage of improved spatial resolution compared to gamma camera imaging and a relatively long half-life of 4.16 days [35]. However, as this radiopharmaceutical is not readily available within the UK it would not be practical to implement and so is not investigated here.

1.3. Gamma Camera Imaging Introduction

Gamma camera imaging enables the distribution of radionuclides to be visualised through the detection of gamma photons emitted by the radionuclides and can be used to quantify the amount of radioactivity present by applying sensitivity factors. A review of the different methods used in literature for calculating these sensitivity factors is given in Chapter 2.4.9.

A schematic diagram of a conventional gamma camera detector is given in Figure 2, which consists of a collimator, scintillator crystal and photomultiplier tubes (PMTs). Gamma cameras with solid state detectors are also available [36]. However, appropriate collimators are not commonly available for I-131 imaging using commercial solid state systems [37] and so will not be discussed further in this work.

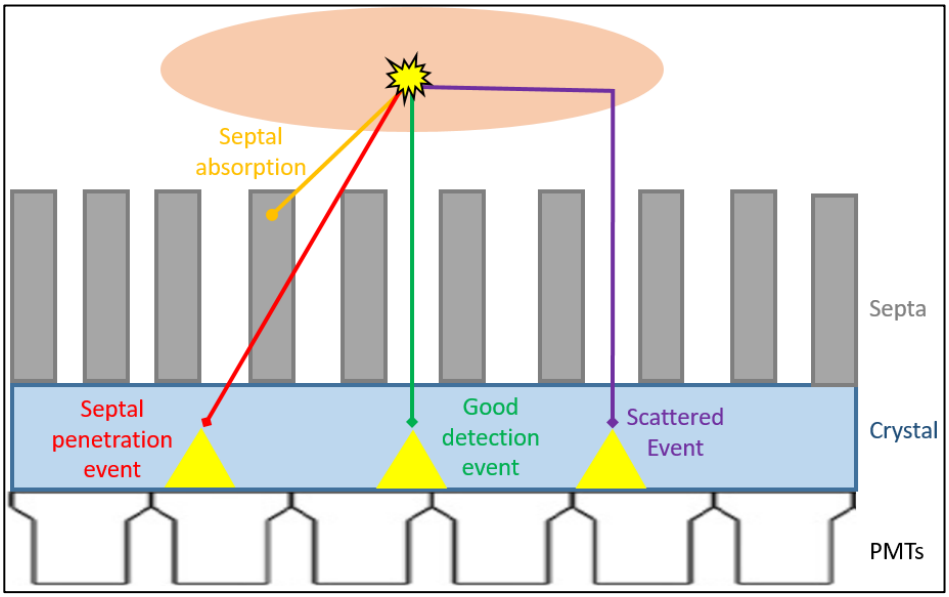

Figure 2. Schematic diagram of a conventional gamma camera detector.

The gamma camera collimator consists of septa with parallel holes, which preferentially absorb gamma photons that are not perpendicular to the detector head. This enables positional information to be obtained from the isotropic radioactive emissions. The scintillator crystal absorbs energy from gamma photons and produces visible light via scintillation, which then travels through the crystal. Light photons incident upon the photocathode surface of the PMT produce electrons, creating a current pulse amplified by the dynodes within the PMT. The total amplitude of the current pulse from all PMTs is proportional to the gamma photon energy deposited within the scintillation crystal, enabling the absorbed photon energy to be determined. The location of the gamma photon emission is then determined from the PMT signals and a 2D (planar) image formed. Acquiring multiple 2D images (projections) at different angles around the patient allows a 3D (SPECT) image of the activity distribution to be reconstructed.

The SPECT reconstruction is commonly performed using OSEM, an iterative method which can incorporate correction for factors such as attenuation, scatter and source distance dependence. The reconstruction parameters should be optimised for dosimetry and a literature review of SPECT image reconstruction optimisation methods is given in Chapter 2.4.8. SPECT images may also be fused with an x-ray produced 3D (CT) scan, to give anatomical localisation and correction for photon attenuation within the patient [38]. The CT scanner is commonly attached to the gamma camera system to give improved co-registration between the gamma camera and CT images.

I-131 has gamma photon emissions at 364keV, 637keV and 723keV [9], with the 364keV emission primarily being used in gamma camera imaging. However factors such as statistical fluctuations in the number of light photons collected from photon absorption within the crystal; photoelectrons emitted from the photocathode and; electron multiplication by the PMTs result poor energy resolution [39]. Therefore a broad peak will instead be seen at each of these energies (photopeak). Emitted photons may undergo Compton scattering within the patient or collimator, causing a change in photon direction and incorrect photon localisation (see Figure 2). This will cause a deterioration in image contrast and spatial resolution. This scattering will also result in a loss of energy, giving a range of energies detected. To reduce the scattered photon interference, signals corresponding to a set energy range (window) around the main photon emission energy may be used for image formation (see Figure 3). However, for I-131 the 637keV and 723keV emissions down-scatter into the 364keV photopeak window and for patient studies, scattered events in the photopeak window are estimated to be 40–50% of the total events [23]. Methods given in literature for reducing the impact of scatter are discussed in Chapter 2.4.5.

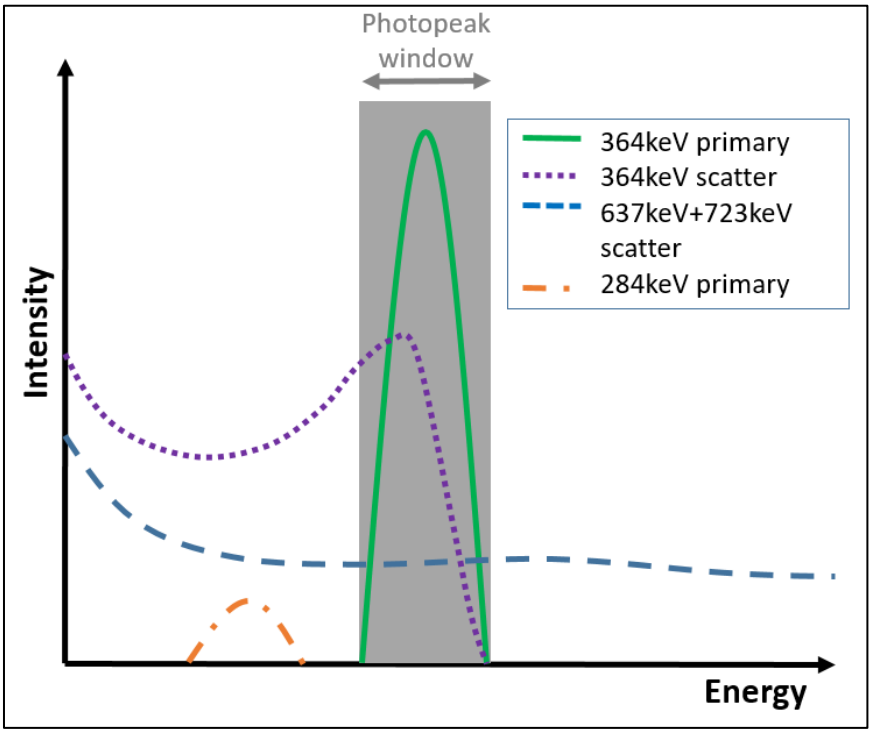

Figure 3. I-131 spectrum separated according to type of interaction. The 364keV primary can be seen along with events due to Compton scatter. The 364keV±10% photopeak window is shown in grey.

Gamma photons emitted from deeper within the patient are more likely to undergo Compton scattering and not be detected within the photopeak window. An increased

tissue depth and density also increases the likelihood of photoelectric absorption, where the emission will not be detected. Both these effects will cause a reduction of counts in the gamma camera image for sources deeper within tissue, impacting on activity quantification. A review of attenuation correction methods given in literature is discussed in Chapter 2.4.3.

The collimator is typically a hexagonal shape with holes to allow photons traveling perpendicular to the detector through and consist of high density material to absorb photons traveling at an angle to the detector. However the collimator photon acceptance angle increases with source distance from the collimator, resulting in worse resolution with distance, as shown schematically in Figure 4(a).

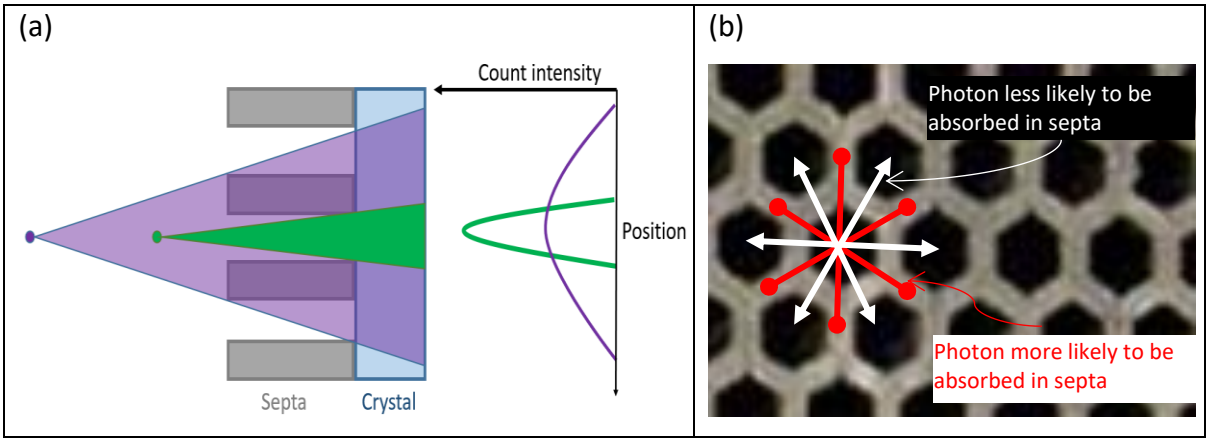

Figure 4. Schematic diagrams depicting impact of collimator structure on resolution and septal penetration. (a) Change in resolution with source distance from gamma camera detector is shown. (b) Impact of collimator hexagonal structure on septal penetration is shown (taken from Barrack et al 2018 [40]*).*

Collimators would ideally stop all photons from traveling through the septa however, the high energy emissions from I-131 may penetrate through the septa without being absorbed (see Figure 2). This can also cause blurring of the detected image. Due to the hexagonal shape of the collimators, photons may need travel through more septal material in certain directions. This increase the likelihood of absorption in these directions, resulting in the star shaped septal penetration artefacts, as demonstrated schematically in Figure 4(b). As source to collimator distance changes the path length through the septa will also change, resulting in a change in the septal penetration artefact appearance (illustrated in Figure 5). Methods given in literature for reducing the impact of these collimator-detector response effects is discussed in Chapter 2.4.6.

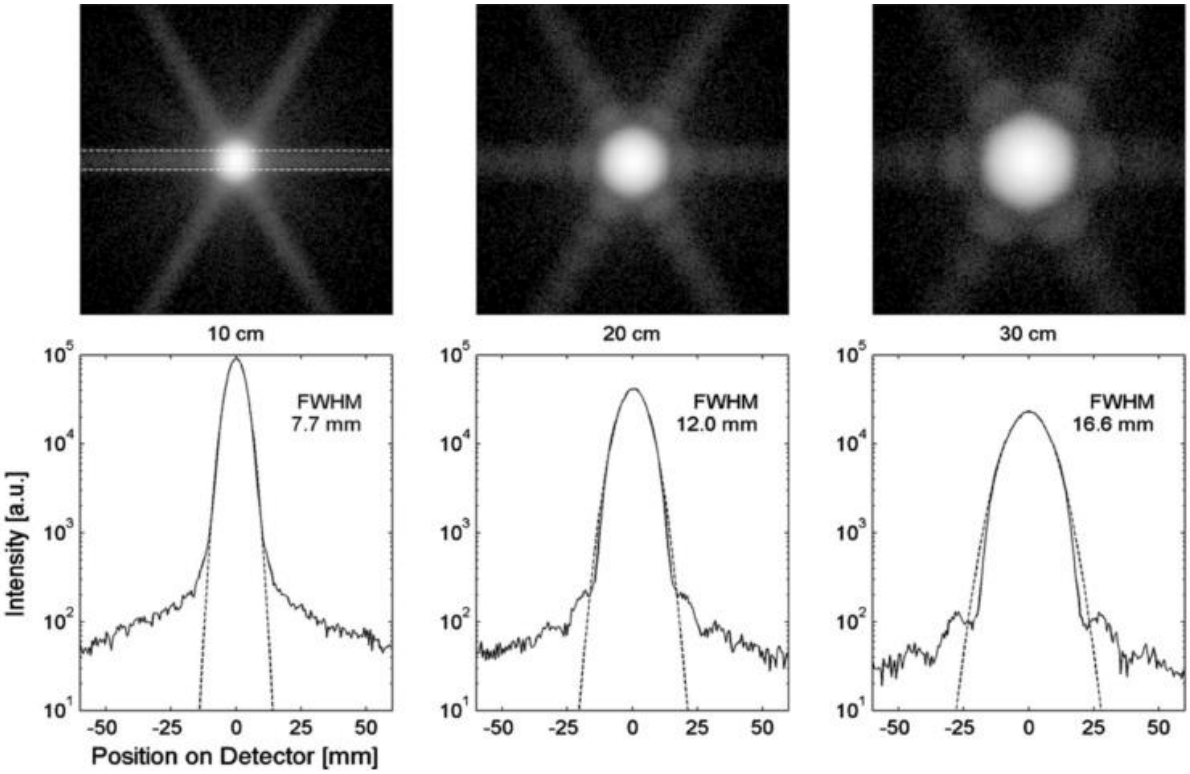

Figure 5. Impact of distance on gamma camera imaging of a point source. Top row: images of Tc-99m point sources measured at different typical source-to-collimator distances. Bottom row: line profiles through the centre of the point sources. The extent of the line profiles is indicated in the upper left image. Gaussian functions were fitted to the line profiles. Taken from Ritt et al. (2014) [41].

Gamma camera quantification is also impacted by the partial volume effect (PVE). This can be defined as "the loss in apparent activity that occurs when an object partially occupies the sensitive volume of the imaging instrument (in space or time)" [42]. The image voxel size can result in multiple tissues residing within the same voxel, resulting in spill-in and spill-out effects, as illustrated in Figure 6. The limited spatial resolution of the system will also cause blurring in the detected image, resulting in a loss of the maximum intensity seen for smaller objects (see Figure 4(a)). A discussion of partial volume correction methods given in literature is discussed in Chapter 2.4.7.

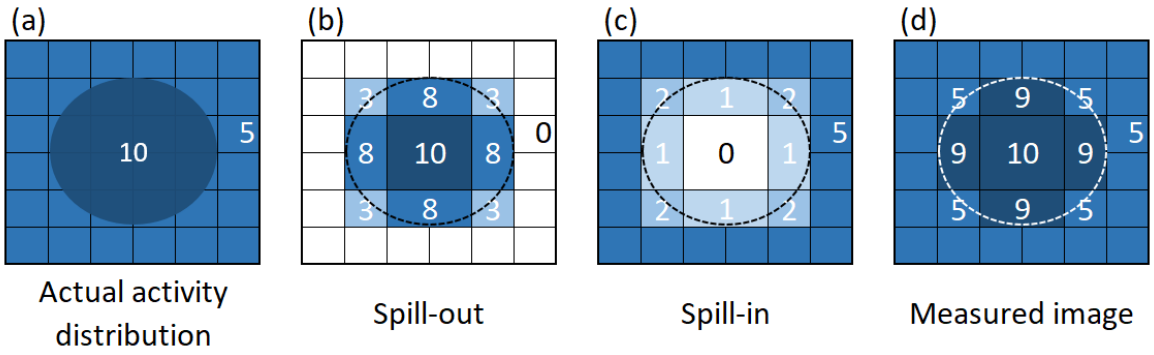

Figure 6. Impact of voxelisation on PVE schematic diagram. The measured image (d) from actual activity distribution (a) is affected by spill out of counts (b) and spill in of counts (c). Adapted from Soret et al 2007 [43].

When an event is detected the gamma camera system can also experience deadtime, where it can no longer register new events, resulting in a reduction in counts. For non-paralysable systems, new events occurring during deadtime will be lost resulting in a plateau in counts [44] (see Figure 7). For paralysable systems these events will not be registered and will restart the deadtime, resulting in a saturation point after which the detection rate will decrease, as illustrated in Figure 7 [44].

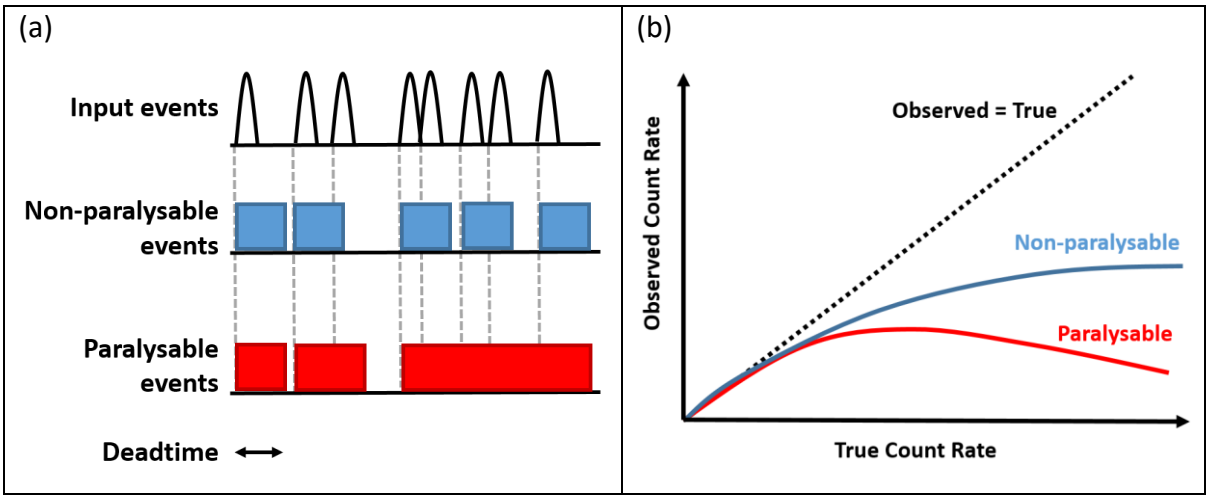

Figure 7. Schematic diagram and graph illustrating the impact of deadtime on detector counts. (a) Schematic illustrating deadtime, where events impacting on detector during deadtime in the non-paralysable system are not counted, while in the paralysable system they restart the deadtime, reducing the number of events that can be detected. (b) Graph illustrating impact of deadtime on measured count rate, with the non-paralysable system reaching a maximum count rate after which it stabilises, while the count rate in the paralysable system decreases after the maximum is reached.

Paralysable deadtime can be described using Equation 4 while non-paralysable deadtime can be described using Equations 5 and 6, where R_O is the observed count rate, R_T is the true count rate and τ is the deadtime [45]. Therefore if R_O and τ are known then R_T can be calculated analytically using Equation 6 for non-paralysable systems or iteratively using

Equation 4 for paralysable systems. A review of deadtime correction methods in literature is given in Chapter 2.4.2.

$$R_O = R_T e^{-R_T \tau} \quad (4)$$

$$R_O = \frac{R_T}{1 + R_T \tau} \quad (5)$$

$$R_T = \frac{R_O}{1 - R_O \tau} \quad (6)$$

To summarise, gamma cameras produce images from radioactive emissions and sensitivity factors can be applied to quantify the amount of radioactivity this corresponds to. Both Compton scattering and photoelectric absorption can result in a reduction in detected count rate due to patient tissue depth and density. Deadtime when high levels of radioactivity are imaged can also cause a reduction in detected count rate. Gamma photon scatter may cause errors in spatial localisation and hence poorer contrast and resolution. Larger source to collimator distances also give poorer spatial resolution. Septal penetration will further worsen resolution and varies with angle due to the collimator hexagonal shape. The spatial resolution and voxel sizes will result in partial volume effects, with spill out reducing the maximum count intensity within small objects and mean counts within objects. All these factors hinder the ability to accurately quantify the activity within the patient using gamma camera imaging and so corrections should be performed. The correction methods given in literature are reviewed within Chapter 2.4 and an experimental investigation into key methods identified in the review are given in Chapter 4.

1.4. Aims

This work was commenced in 2017 based on the clear need for dosimetry implementation. The focus of this work was to assess methods that can be used practically to perform dosimetry for patients with thyroid carcinoma, along with areas requiring further research. This patient cohort was chosen they would require the application of the key dosimetry techniques and they are treated as inpatients, meaning dosimetry involving measurements at multiple time points would be more practical to implement. However the findings could be implemented for other forms of molecular radiotherapy.

The aims of this research were to:

- Perform a literature review to identify common techniques used for performing dosimetry which could be practically implemented in a standard hospital setting and determine areas for further research with I-131 thyroid carcinoma therapy.
- Perform I-131 gamma camera calibrations for tumour dosimetry, investigating feasible methods given in literature for deadtime, SPECT reconstruction parameters, sensitivity and partial volume effect correction.
- Investigate methods for performing I-131 NaI thyroid patient post therapy whole body retention measurements for use in bone marrow dosimetry.
- Develop a procedure for performing I-131 NaI thyroid carcinoma post therapy patient dosimetry.
- Develop a method for external validation of the dosimetry technique by a national metrology centre through collaboration with the National Physical Laboratory and use this method to successfully validate the planned dosimetry processes.

As tumour and bone marrow dosimetry is not currently routinely performed in the UK for patients with thyroid cancer, this in an innovative project which could make a real difference to patients' lives. It could enable more data to be gathered on doses received to target and non-target areas as well as the likelihood of retreatments being required. This could lead to treatments to being optimised further, improving patient outcomes.

2. Literature Review

2.1. Radiation Legislation

European directive 2013/59/EURATOM states that radiotherapeutic exposures should be individually planned and verified, explicitly stating that this covers molecular radiotherapy [14]. This directive was brought into UK law under the Ionising Radiation (Medical Exposure) Regulations 2017, which came into force in February 2018 [15]. The Administration of Radioactive Substances Advisory Committee (ARSAC) who issue licences for the use of radiopharmaceuticals within the UK state in their Notes for Guidance "in cancer treatments with radioactive substances, the absorbed dose to the tumour, and to non-target volumes and tissues, following each administration should be measured and

recorded, to permit subsequent optimisation of total doses" [46]. For practitioner licence ARSAC applications, there is also a requirement for the practitioner to provide details on how dosimetry will be performed for molecular radiotherapies [46].

Dosimetry is standard practice within external beam radiotherapy using x-rays and is seen as essential to optimise therapeutic benefit and minimise potential side effects but dosimetry is not yet common within molecular radiotherapy. The European Association of Nuclear Medicine (EANM) published a position paper in 2020 regarding the 2013/59/EURATOM directive, suggesting 3 levels for performing molecular radiotherapy dosimetry [47]. For Level 1 standard activities are prescribed, with administered activity measured as within 10% of the prescription and absorbed dose reported based on cohort averaged data. For Level 2 activity based prescription is still used but the individual's dose received to organs at risk is reported and estimation of absorbed dose to target regions is optional. With Level 3 dosimetry-guided patient-specific prescription and verification is performed. Level 1 is recommended for standardised therapies, defined as "approved products (by EMA or by CE marking) for radionuclide therapies being administered according to the package inserts or relevant guidelines" [47]. Level 2 is recommended non-standardised therapies, defined as "either radionuclide therapies in developmental phase or approved radiopharmaceuticals being used off-label" [47]. A table is given for common therapies and I-131 NaI therapy for differentiated thyroid cancer is defined as a standardised therapy with prescription according to Level 1 or 2 and dosimetry as optional [47]. The paper suggests dosimetry based prescription may contravene the European Medicines Agency (EMA) and supplier recommended instructions for use. It also suggests that there is not yet sufficient evidence for dosimetry based prescription, so recommends patient-specific verification dosimetry to build this evidence base, although this is only recommended for non-standardised therapies.

The UK based Internal Dosimetry User Group (IDUG) have developed a position statement, currently available to members ahead of print [48]. This work suggests that the EANM Level 1 would not meet the UK requirements for measurement of doses to tumour and non-target tissues. It also suggests that many "standardised" therapies do not have adequate dosimetry and toxicity data. Both IDUG and this author support the recommendations in the ARSAC Notes for Guidance [49] but acknowledge that this may require additional funding for equipment and staffing [48]. It is also worth noting that for I-131 NaI the Summary of Product Characteristics suggests that 1850-3700 MBq should be used for ablations and 3700-11100 MBq for treatment of metastases, based on size and

radioiodine uptake [50], [51]. Hence product licencing is not a barrier to dosimetry based prescription for this therapy. Therefore it is felt that the implementation of post-therapy verification dosimetry for I-131 differentiated thyroid carcinoma therapy should be performed. This would enable more evidence to be built regarding the impact of dose on therapeutic benefit and patient morbidity. Pre-therapy treatment planning dosimetry should then be performed when it is felt sufficient evidence has been built.

2.2. Recent Multicentre Dosimetry Studies and Guidelines

There have been a number of studies performed recently investigating dosimetry involving I-131 in multicentre settings, using methods which may be practical to implement in a standard clinical setting. The SEL-I-METRY trial investigated the use of Selumetinib in iodine refractory differentiated thyroid cancer patients in 8 UK centres with 9 SPECT/CT systems, using I-131 and I-123 for thyroid cancer treatment response predication [52], [53]. Calibration protocols were established and used across all sites, with SPECT reconstruction and analysis being performed by the trial coordinator. The Horizon 2020 MEDIRAD project work package 3 is investigating the dose-response relationship for remnant thyroid tissue and organs at risk in 5 European centres, including the UK [54]. The dosimetry aspects for both projects were run by the same centre and so use similar methodology.

Zimmerman *et al* 2017 performed a IAEA phantom international study across 9 countries, with 10 SPECT systems and compared planar, SPECT and SPECT/CT imaging of four Ba-133 NIST calibrated cylinder sources as a surrogate for I-131 [55]. This work investigated site specific gamma camera calibration methods and the impact of standardisation. The calibration parameter results were not included in this paper but it did highlight the differences obtained using different methods and need for standardisation.

The 2016 to 2019 MRTDosimetry project investigated a number of dosimetry aspects including quantitative imaging using SPECT/CT, time activity curve assessment and dosimetry uncertainty analysis. This work involved national metrology centres and 8 European clinical centres across 5 countries. SPECT/CT calibrations were performed with I-131 and Ba-133 as a substitute for I-131, as well as with Lu-177. Following this work guidelines on performing dosimetry uncertainty assessment were published by the EANM in 2018 and also give an example method for performing dosimetry [17].

In 2008 the EANM published guidelines on performing bone marrow dosimetry for pre-therapy thyroid cancer dosimetry [21], with more generic guidelines for bone marrow and

whole body dosimetry published in 2010 [20]. Guidelines for I-131 pre-therapy dosimetry in benign thyroid disease were published in 2012 [18]. In 2020 the EANM published dosimetry guidelines for I-131 mIBG therapies, which include methodology for performing I-131 gamma camera calibrations as well as blood and whole body retention measurements [16]. MIRD published guidelines on performing dosimetry using SPECT scanning in 2012 (MIRD 23) [56], with I-131 specific SPECT scanning guidelines published in 2013 (MIRD 24) [23]. EANM and MIRD also published joint guidelines on Lu-117 SPECT dosimetry in 2016 (MIRD 26) [22]. Whole body dosimetry guidance was published by IDUG in 2015 [57]. However the dosimetry methods and calibrations performed vary and therefore this work will focus on comparing these different methods.

2.3. Bone Marrow and Blood Dosimetry

Bone marrow does not actively accumulate iodine, therefore the EANM guidelines on bone marrow dosimetry suggest that the dose to the bone marrow can be estimated to be due to irradiation from circulating radioiodine in the blood and from the rest of the body [20], [21]. The dose to the bone marrow from the rest of the body will depend on the relative distribution of uptake in areas such as the thyroid, gastrointestinal system and bladder as well as their distance from the bone marrow, which will vary from patient to patient. However, for simplicity this can be determined from the total activity in the body and a single S-factor. The method for calculating the dose to blood and bone marrow depends on the assumptions made and a number of different methods are available in literature [21], [32], [58]. There appears to be little work published demonstrating correlation between calculated absorbed dose to blood/bone marrow methods and patient haematological response [20]. Therefore, correlation of absorbed dose to blood/bone marrow methods with haematological response and DNA damage rate is an area that requires further investigation and is currently a focus of the MEDIRAD NFRP-2016-2017 project [59]. In the interim it is suggested that Equations 7 and 8 given below from the EANM guidelines should be used [20], [21].

$$D_{blood}[Gy] = A_0[MBq]\left(108\ \tau_{Blood}^{1ml}[h] + \frac{0.0188}{(wt\ [kg])^{\frac{2}{3}}}\tau_{WB}[h]\right) \quad (7)$$

$$D_{red\ marrow}[Gy] = A_0[MBq]\left(61\ \tau_{Blood}^{1ml}[h] + \frac{0.106}{wt\ [kg]}\tau_{WB}[h]\right) \quad (8)$$

D_{blood} and $D_{red\ marrow}$ are the doses to the blood and red marrow respectively, A_0 is the administered activity, τ_{Blood}^{1ml} is the residence time in 1 ml of blood, τ_{WB} is the residence time in the whole body and wt is the patient weight. The residence time is calculated by integrating the retention, $R(t)$, from zero to infinity. Therefore uptake following a bi-exponential clearance can be calculated using the following equations

$$R(t) = \frac{A(t)}{A_0} = A_1 e^{-\lambda_1 t} + A_2 e^{-\lambda_1 t} \quad (9)$$

$$\tau = \int_0^\infty R(t)\mathrm{d}t = \frac{A_1}{\lambda_1} + \frac{A_2}{\lambda_2} \quad (10)$$

where $A(t)$ is the activity at time t and A_1, A_2, λ_1 and λ_2 are fitting constants.

The majority of calculation methods require the time integrated whole-body activity to be measured. Most commonly this is performed using an external probe positioned at a distance from the patient but gamma camera imaging can also be used [20]. Access to gamma cameras for such additional imaging is typically limited, and radioiodine inpatients typically undergo probe measurements at least daily to determine when they can be safely discharged. Therefore as it will be possible to obtain more measurements with a probe, giving more measurements for the biokinetic model, this is the preferred option [20].

EANM dosimetry guidelines suggest the whole body net counts should be greater than 10^5 and the geometric mean from anterior and posterior retention measurements should be used in accordance with Equation 11 [19], [20].

$$Counts_{net\ geometric\ mean} = \sqrt{Counts_{net\ anterior} \times Counts_{net\ posterior}} \quad (11)$$

However there appears to be limited experimental evidence for the use of geometric mean data. Willegaignon et al. 2012 suggest in their experience only anterior acquisitions are required for I-131 thyroid carcinoma patients, with a net count rate which is 5% higher than conjugate acquisitions [58]. Practice at RSCH and in many sites is to perform anterior probe retention measurements to determine when patients can be discharged. Adding posterior measurements would be more time consuming and potentially involve more discomfort to the patient if performed using a ceiling probe with the patient lying on their front. Therefore, further investigation into the impact of conjugate retention measurements is an area for further research.

The EANM bone marrow dosimetry guidelines state that background measurements should be performed without the patient present before each whole body patient measurement [20], [21]. However the EANM I-131 mIBG dosimetry guidelines suggest that background readings should be acquired prior to administration and then when possible over the course of treatment or if contamination is suspected [16]. For a therapy it may not always be practical to perform background measurements without the patient present, as the measurements are typically performed in their room and the patient leaving this area could result in dose to the public and present a contamination risk. Therefore an investigation into the impact of background variation on whole body residence time is required.

For blood residence time calculation measurements blood samples should be taken at multiple time points and activity concentration quantified, most commonly using a NaI(Tl) well-type detector [20], [21]. EANM guidelines suggest that the volume of the samples should be determined either based on weight or pipetting an exact pre-set volume [20], [21]. The activity concentration can then be calculated based on prior counter sensitivity calibration. EANM guidelines suggest using two 1ml aliquots [21], while the MEDIRAD program used three 0.2ml aliquots [60].

There is limited evidence for the optimum number and timings of the measurements. The optimal timings for Lu-177 DOTATATE and I-131 mIBG therapies were investigated by the MRTDosimetry working group who found issues due to considerable variation between patients [61]. They suggested that a time point as late as possible should be used as to capture the slow clearance phases of the time activity curve, which often has an significant contribution to the time integrated activity [61]. In RSCH and in many sites, probes in the ceiling above the patient bed are used for whole body measurements. Therefore obtaining late time point whole body measurements after the patient is discharged can be challenging as the room may be in use by another patient. The probe sensitivity may also not be high enough to provide sufficient counts from the patient at late time points. Late time point gamma camera imaging is recommended for tumour dosimetry purposes. Therefore, if images could be used for late time point whole body measurements in combination with earlier probe measurements this could be beneficial and is an area for further investigation. An investigation into the impact of late time point measurements for I-131 NaI thyroid cancer patients would also be beneficial to determine the likely error for cases where these measurements are not possible.

EANM bone marrow dosimetry guidelines suggest whole body and blood sample measurements at 2, 6, 24 and 96 hours post administration, with an optional measurement at 144 hours [21]. The majority of work published includes the EANM required measurements, often with additional measurements at 48 hours [12], [34], [62], [63].

A bi-exponential clearance method is typically suggested, however additional long lived clearance components which appear after the last measurement time point cannot be excluded, and so it has been recommended that upper limits on the residence time be calculated by assuming physical half-life after the last measurement point to give a worst case dose estimate [21].

Blood dose has been used as a surrogate for dose to bone marrow, but has been noted to be around 10% to 30% higher [12], [21]. Due to the different methods of calculating activities to administer based on dose to blood or bone marrow, it has been suggested that both should be reported [20]. Therefore this should be done as part of any clinical implementation of dosimetry.

2.4. Gamma Camera Imaging

Gamma camera images can be used to quantify the uptake of I-131 within the patient for dosimetry purposes. An introduction to gamma camera imaging is given in Chapter 1.3 and identified a number of factors which can reduce the quantitative accuracy of gamma camera imaging. This included deadtime, distance dependent spatial resolution, septal penetration, partial volume effects, scatter and attenuation. In this chapter methods given in literature regarding correcting for these effects are discussed, as well as reconstruction parameter optimisation for SPECT imaging.

Both planar and SPECT gamma camera imaging are used in literature for dosimetry and a discussion of the different methods used in literature is given in Chapter 2.4.1. For quantitative imaging the measured gamma camera counts must be converted to units of I-131 activity, which requires a sensitivity calibration. Methods used in literature to perform this calibration are given in Chapter 2.4.9. The patient dose can be calculated from quantitative images at multiple time points and a discussion of the time points used in literature is given in Chapter 2.4.10.

2.4.1. Planar vs SPECT Imaging

Both planar and SPECT gamma camera images can be used for I-131 quantification. SPECT/CT imaging is seen as superior to planar imaging for dosimetry due to its improved quantitative accuracy [64]. SPECT is less affected by the background activity from under- or overlying regions, as depicted in Figure 8. The CT can be used for attenuation correction and the SPECT reconstruction can allow correction for system effects such as variable resolution with distance [64].

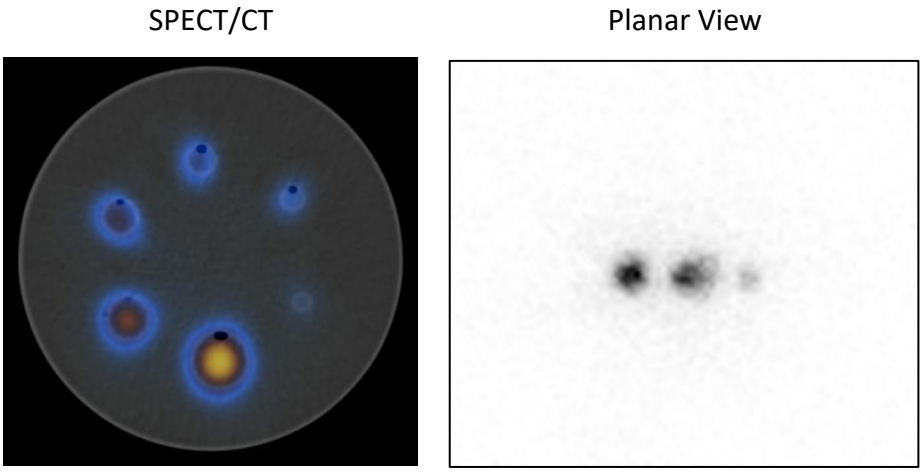

Figure 8. SPECT and planar images for a Jaszczak phantom with 6 filled spheres. All 6 spheres can be identified on SPECT/CT image but only 3 spheres can be visualised on the planar image due to overlying objects, which will affect quantification.

However, SPECT/CT is not available in all Nuclear Medicine imaging departments and these systems may often have a high diagnostic workload. This means repeat dosimetry SPECT/CT imaging of a patient may not be possible and planar imaging may be more appropriate. It has also been suggested that using SPECT/CT at a single time point for absolute activity quantification, combined with planar imaging at multiple time points to determine the relative uptake and clearance can be an effective compromise [20], [65], [66]. Assié et al. found that the hybrid method gives a closer agreement to SPECT dose estimates compared to planar only imaging in six Y90 Zevalin patients [67]. However there appears to be no data on the errors introduced by the hybrid imaging method compared to SPECT/CT for I-131 thyroid carcinoma dosimetry and so this is an area that requires further research.

2.4.2. Deadtime

Deadtime can result in a reduction of detected counts at high input count rates, as discussed in Chapter 1.3. One method of estimating deadtime for patient acquisitions is

to position a reference source with a low activity within the field of view as far as possible from the highest areas of uptake and use this to provide activity calibration [68], [69]. However, this method is subject to errors due to scatter and septal penetration from nearby sources, so is not recommended for SPECT in recent MIRD [56] or EANM guidelines [16]. This is largely due to the difficulties in positioning the source away from high activity areas within the patient.

For images of the whole body, multiple fields of view (FOVs) may be stitched together and continuity correction can be performed, with counts being normalised based on ratios from regions where views overlap, starting with a low deadtime area such as the feet [70]. This has the advantage of not requiring a calibration source and is applicable after the turnover point of the dead time curve, however it is more computationally complex, with artefacts seen where the FOV are stitched [70], [71].

The most common method used in literature to correct for deadtime is to characterise the system using phantom experiments, in which a phantom with a high activity is imaged at multiple time points as it decays or activity is added to a phantom in increments [52], [56], [65]. For example Gregory *et al* used the increment method, with planar imaging of a Jaszczak phantom with 20MBq to 2.8GBq I-131 for the SEL-I-METRY trial [53]. Alternatively, Taprogge *et al* 2020 used a I-131 decaying capsule within a cylindrical phantom due to dose restrictions but found good agreement with the Gregory *et al* method [72]. The EANM I-131 mIBG dosimetry guidelines suggest either decaying source or increment methods can be used but the increment method may be more practical due to the timescales involved [16].

Gamma photons emitted by I-131 frequently undergo Compton scattering within tissue, causing a decrease in photon energy. This can cause the detected photons to have an energy below the range used for the photopeak window, however they will still contribute towards the system deadtime. Therefore the deadtime will depend on the whole spectrum detected by the gamma camera and not just the photopeak window used for imaging. As the whole spectrum is not typically measured, this means the phantom used for characterisation should give scatter conditions which are representative of the patient.

For calculation of the system deadtime the “true” count rate may be determined from phantom activities by linear extrapolation of measured count rates at low activities [16], [53], [72] as described by the National Electrical Manufacturers Association [73]. For the

SEL-I-METRY and MEDIRAD projects this was performed based on 5 measurements with phantom activities less than 100MBq [53], [72]. There is debate as to which deadtime model should be used for gamma cameras, with paralysable and mixed paralysable/non-paralysable models being used in literature [16], [65], [74]. Gregory *et al* 2019 found that for modern systems with high count rate modes enabled, both paralysable and non-paralysable models gave good agreement for the I-131 activities up to 2.8GBq [53]. However the EANM mIBG 2020 dosimetry guidelines suggest using a paralysable model [16].

With the phantom method, care must be taken to avoid imaging patients with activities which occur after the maximum point. In the non-paralysable case increasing activities will result in constant counts and in the paralysable case increasing activities will result in a decrease in the detected counts (see Figure 7(b)). The maximum input count rate and activity that this corresponds to will depend on the system. It has been suggested that imaging with counting rates higher than approximately 50 kcps is not recommended [23]. However with modern gamma camera systems manufacturers may have high count rate modes, which may be allow the maximum count rate point to be reached at higher activities. For example Siemens and Philips systems automatically move into a high count rate mode, while for the GE systems used at RSCH “fast mode” must be enabled [16], [53]. The “fast mode” for GE systems must be optimised by the manufacturer and appears to limit the length of pulse analysed. At RSCH it has been found that GE fast mode may require additional linearity and uniformity maps to be set and if two different modes are used calibrations must be performed using both methods [75]. There appears to be limited data on the impact of using these high count rate modes clinically, therefore this is an area that required further investigation.

There is some debate as to the energy windows which should be used for deadtime modelling due to the impact of changing scatter conditions on deadtime. For example, Delpon et al found for I-131 20% window width photopeak imaging, calculating deadtime correction factors using (a) a reference source, (b) photopeak and 173-235keV Compton plateau window and (c) the full spectrum of 50-750keV resulted in errors of +7%, -4% and 3% respectively [71]. Guy et al found when placing 2-10cm scattering material between sources of 40-3000MBq I-131, deadtime correction factors should be applied to the TEW-corrected counts [76]. Gregory *et al* used Hermes scatter correction which requires photopeak only imaging and so suggested using the photopeak only due to changes in

spectrum at high count rates affecting the spectra (see Figure 9(a)) [53]. Therefore this is an area which requires further research.

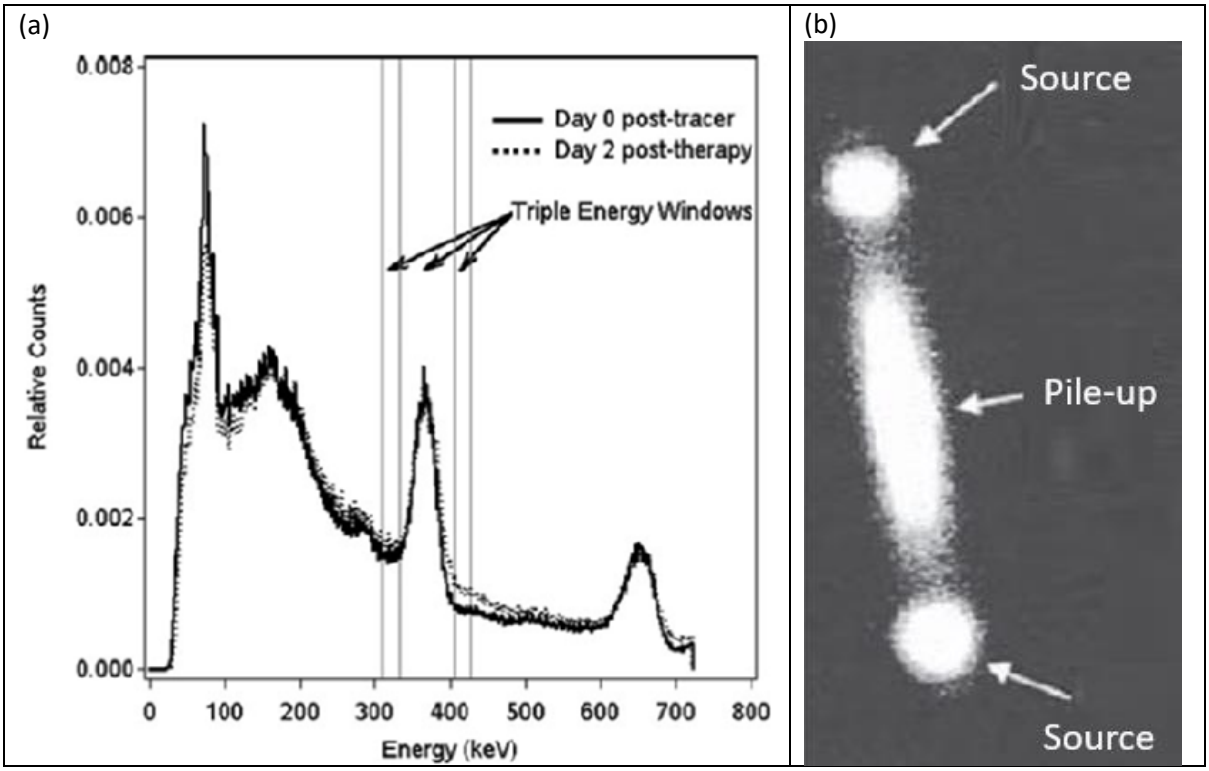

Figure 9. Demonstration of deadtime impact on I-131 imaging. (a) Comparison of I-131 energy spectra measured during post-tracer imaging and post-therapy imaging of a typical patient on a Siemens Symbia TruePoint SPECT/CT system. (b) Image of two relatively high activity Tc-99m point sources, the events within the band between the sources are mispositioned due to pulse pile-up. [(a) taken from Schipper et al. (2012) [77]*, (b) adapted from Cherry* [78]*].*

At high count rates pulse pile up can be seen, where two photons arriving at the detector within the detector resolving time are seen as one event, with an energy which is the sum of the photons. This can result in mispositioning, with a location somewhere between the two events, as depicted in Figure 9(b) [78]. A corresponding impact can also be seen on the observed spectrum, as shown in Figure 9(a) [77]. This may also be impacted by the number of photomultiplier tubes used by the gamma camera system to determine the position of event, with Guy et al reporting that distortion was only seen between Tc-99m sources with a separation of less than 15cm for an ADAC Vertex system [76]. Therefore clinical images with two nearby areas of high uptake should be checked for this mispositioning of events.

Different methods of applying the deadtime corrections are also given in literature for SPECT, with the EANM mIBG dosimetry guidelines suggesting corrections either pre or post reconstruction [16]. For the pre-reconstruction method a deadtime correction factor is applied to each pixel within the projection, based on the measured count rate for that

projection or the mean from all projections. For the post-reconstruction method a deadtime factor is calculated using the mean count rate from all projections and is applied to each voxel. The post reconstruction method does not require specialist software and is the method used by Gregory *et al* 2019 for the SEL-I-METRY trial [53]. However different projections may suffer from differing of deadtime and so the pre-reconstruction projection specific method is recommended by MIRD [23]. The recent Siemens xSPECT Quant software include projection based deadtime correction [79] however most other commercial systems do not and so would require in house software to be developed.

2.4.3.Attenuation Correction

Photoelectric absorption and Compton scattering result in a detected counts reduction from gamma photons emitted deeper within the patient, as discussed in Chapter 1.3. Therefore attenuation correction (AC) is required to correct for this count reduction. With SPECT/CT imaging, the CT data is typically used to produce an electron density map which can be used to calculate and hence correct for the attenuation of the gamma photons [80]. If CT is not available then Chang attenuation correction can be used for SPECT data, whereby constant (typically water) attenuation is assumed within the delineated patient volume and everything outside the patient is assumed to be air [81]. While this method works well in areas with uniform density such as the brain, it works less well in areas where there is more variance such as the lung and so CT correction is the optimal choice [82].

For planar imaging, CT and Chang attenuation correction cannot be used and so conjugate view corrections can be utilised instead, with details of different methods given in MIRD Report 16 [83]. If SPECT is available for at least one time point and planar imaging is simply being used to model the relative change in distribution, then geometric mean correction is the simplest method for the removal of source depth dependence. However this method will not account for changes in attenuation where tracer distribution within a tissue or organ changes and patient thickness is not uniform. If quantification is to be performed on planar imaging then attenuation correction can be performed through assessing the source tissue thickness and total patient thickness for the area of interest, through either additional lateral views or 3D imaging e.g. SPECT, CT, MRI along with an estimation of the attenuation coefficients through transmission source measurements or

lookup tables. However, practically this may be time consuming to perform and therefore SPECT/CT quantification is recommended where possible.

2.4.4. Background Correction

For radioiodine patients the uptake of radioiodine in the blood and other organs over or underlying the area of interest in planar images can vary over time and may cause increases in the detected counts. Background and scattered radiation can also contribute towards the detected counts. Therefore, to correct for these effects a "background" region of interest placed in an area which is thought to be representative of the background within the area of interest can be used [83].

2.4.5. Scatter

The high energy I-131 gamma emissions are most likely to interact with tissue material via Compton scattering, resulting in a loss of energy with a change in the angle of travel and hence incorrect spatial registration of counts. A number of different methods have been suggested to correct for scatter, and detailed discussion is given by Zaidi and Koral (2006) [84]. The most commonly used in literature and commercially is dual or triple energy window based methods [85], [86], while the effective scatter source estimation (ESSE) method [87] and accelerated Monte Carlo methods [30], [88] have also recently been implemented commercially for SPECT reconstruction.

TEW correction assumes that the scatter component of the counts in the photopeak can be estimated from counts in scatter windows positioned to the below (C_{lower}) and above (C_{upper}) the photopeak (with counts, $C_{photopeak}$) (shown in Figure 10) according to the following equation

$$C_{primary} = C_{photopeak} - \left(\frac{C_{lower}}{W_{lower}} + \frac{C_{upper}}{W_{upper}}\right) * \frac{W_{photopeak}}{2} \qquad (12)$$

where W_{lower}, W_{upper} and $W_{photopeak}$ are the widths of the lower scatter, upper scatter and photopeak energy windows respectively [86]. Narrow windows better represent the scatter component in the photopeak, however this can lead to noisy images [56], [89]. TEW correction has the advantage that it can be applied to planar imaging, to SPECT projections manually prior to reconstruction and also can be included in the OSEM reconstruction of some commercial systems. Experiments using profiles through uniform

areas of elliptical phantoms have been found that this method can often result in an overestimation of the scatter component [90]. Adding an additional weighting factor to the scatter component based on simulated data has been found to improve this. However a large variation in the optimal factor has been seen (0.25-0.67), which may be due to differences in I-131 volume and surrounding scattering material, limiting its clinical use [90]. Nevertheless the TEW equation is most common in literature due to its ease of implementation.

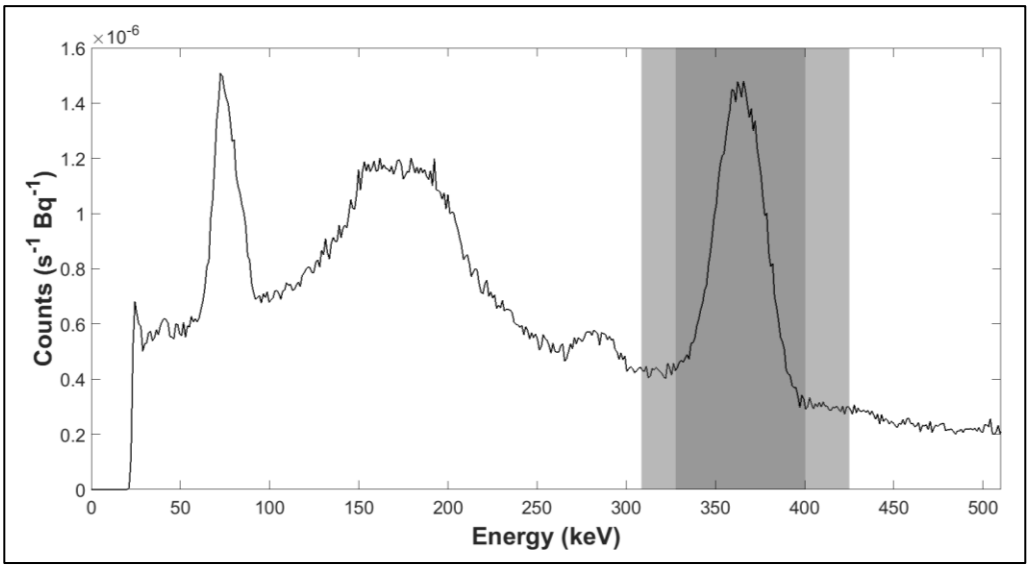

Figure 10. Location and width of the windows used for triple energy window scatter correction. The main window is located at the photopeak and the subwindows are located on both ends of the main window. The counts of primary photons in the main window are estimated as a trapezoid using photons of the two subwindows. [Taken from Barrack et al 2018 [40]*].*

ESSE uses the estimated activity distribution convolved with a scatter kernel based on the photon energy, to estimate the scatter component for each projection. This is then is added to the non-scattered projection estimate to produce the total estimated projection in the reconstruction [87]. Unlike the TEW methods, ESSE does not require the use of additional scatter windows, which require optimisation. ESSE neglects down scatter which is significant in I-131 imaging and assumes constant density, which will not be the case around the thyroid which is near the trachea and for lung metastases. However it has been shown to work well in I-131 imaging [56], [91] and is also available with the Philips Astonish software [92].

Monte Carlo based simulation methods for scatter correction have the potential to provide better quantitative accuracy in SPECT [93], [94], however they require high computing power and specialist software. Hermes provide an accelerated Monte Carlo based scatter correction, which assumes any Compton scattering events are towards the detector [30], [88].

2.4.6. Collimator-Detector Response

The collimator properties, septal penetration and distance between the source and detector can impact on the image resolution and quantification, as discussed in Chapter 1.3. While not commonly performed in planar imaging due to difficulties in estimating source depth, for SPECT collimator detector response (CDR) compensation can be built into the image reconstruction. Commercial systems may model the geometric component as a Gaussian function, neglecting the hexagonal collimator shape, septal penetration component and scatter in the collimator [92]. However edge and oscillation artefacts are often seen with this correction method [92], [95]. The HERMES SUV SPECT (HERMES Medical Solutions) system has a Monte Carlo simulation model option which accounts for collimator septal penetration and scatter for I-131, which can be used within the SPECT reconstruction, improving resolution [96], [97]. Siemens xSPECT Quant software can also account for I-131 septal penetration but instead uses measured depth depended point spread functions [79], [98]. However in a standard clinical setting the reconstruction software is likely to be limited to that which is already in use and the GE Xeleris software available for this work uses a Gaussian function only.

2.4.7. Partial Volume Effect

The PVE can result in an incorrect estimation of counts due to spill in and out effects, as discussed in Chapter 1.3. The PVE depends on the shape of the object of interest and the spatial resolution of the system. For accurate quantification, compensation is needed for objects if any of the dimensions are around less than 3 times the spatial resolution of the system [92], [99]. A number of methods for performing partial volume correction have been suggested and an extensive review is given by Erlandsson et al. (2012) [42], with a summary of the most common corrections given here.

Modelling of the CDR within the SPECT reconstruction can be used to compensate for the PVE by improving the spatial resolution of the imaging system, however due to the noise typically seen within the images and loss of high frequency information during the data

acquisition, this often cannot fully compensate for the PVE seen. Utilising structural information e.g. from the co-registered CT image, can be used to further improve partial volume effect corrections. The Siemens xSPECT bone commercial SPECT reconstruction package uses an ordered-subset conjugate gradient algorithm with zonal maps from the CT to weight the contribution from different tissues in the forward projection step, which can improve spatial resolution and hence reduce the partial volume effect [41]. However for I-131 NaI automatic tissue delineation based on the CT is likely to be challenging for the soft tissue areas of interest, which are often difficult to differentiate in the CT. There appears to be no commercial software that offers post reconstruction partial volume effect correction and this is an area that requires development.

Another method which can also complement the previously mentioned methods is to image a phantom with uniform cylindrical or spherical objects to calculate correction factors [23], [52], [92]. Size dependent recovery coefficients (RC) are calculated as the ratio of measured activity concentration to known activity concentration within an object. A recovery curve is then produced by fitting the measured data, with a sigmoid function being commonly used, as given in the equation below

$$RC(x) = \frac{\alpha}{1 + (\gamma/x)^{\beta}} \qquad (13)$$

where x is the sphere diameter or volume and α, β, γ are fitting parameters [16], [100]. This empiric method relies upon the user delineating the region of interest within the patient to determine the volume and hence correction factor to use, which can be subject to errors. However, this method does not require specialist software and is a recommended by MIRD as a practical method of implementing PVE correction in both SPECT and planar imaging [23]. Both sphere and cylinders are commonly used in literature for this partial volume effect calibration [53], with the EANM I-131 mIBG dosimetry guidelines recommending either could be used [16]. The impact of choice of cylinders or spheres for calibration does not appear to have been investigated for I-131 imaging, therefore this is an area for further investigation. The EANM I-131 mIBG dosimetry guidelines suggest that ideally spheres or cylinders up to 60mm within a larger phantom should be used, however these large objects are not commonly available. Therefore the impact of only using more commonly available phantoms is an area for further investigation. In some published literature the α value is set to unity [17], while in others it is unconstrained [16], [53] therefore investigation into the impact of these different methods is also an area for further investigation.

In recent multicentre dosimetry and quantification studies the volume based method with either spheres or cylinders has been used. For example, in the SEL-I-METRY study six 3D printed cylinders with volumes of 0.8 to 196ml and diameters of 1 to 6.3cm were imaged together within a water filled torso shaped phantom [53]. In the MEDIRAD study six 3D printed spheres with volume of 0.5 to 144ml were imaged together within a water filled cylindrical phantom [72]. For MRTDosimetry cylinders with volumes of 1.7 to 110ml and diameters of 0.75 to 6cm were imaged together within a water filled cylindrical phantom [101].

2.4.8.Other SPECT OSEM Reconstruction Factors

For SPECT OSEM reconstruction the projections are spilt into equal sized smaller subsets, iterative reconstruction is performed using each subset and the processing of all subsets is classed as an iteration. The number of OSEM reconstruction updates is the product of the number of iterations and subsets used, with increased numbers of subsets reducing the computation time for the same number of updates. Increasing the numbers of iterations and subsets will converge upon the true result, at the expense of increasing amount of noise within the image [38]. More updates are required to reach convergence for smaller objects and those with more noise [22], [29], [102]. MIRD 23 suggests using at least 4 projections per subset, with more projections per subset in the case of noisy data (defined as fewer than 50 kcounts per slice) [56]. The addition of CDR modelling in the reconstruction has also been found to require more updates for convergence [22], [56]. However it has been noted that an increased number of updates with CDR correction also increases the prominence of Gibbs edge artefacts [103]. For voxel based dosimetry, the small number of counts per voxel means reducing the variance and hence iterations may be required [29]. If only the mean dose to an organ/lesion is required then the effects of noise will be averaged out over the larger region being assessed and so a higher number of updates can be used [29], [56].

The point at which count convergence is said to be reached is not clear, with MIRD 23 suggesting 90% recovery is sufficient [56] and MIRD 26 suggesting 95% recovery may be preferable [22]. MIRD 26 gives the example of a patient case with a tumour and kidney of similar sizes but different noise levels, where 90% convergence occurs with 20 and 40 updates for the tumour and kidney respectively [22]. However 95% convergence is reached for both regions at 60 updates [22]. This indicates that using a higher

convergence threshold during initial optimisation may result better convergence for a range of noise levels.

Post reconstruction low pass filtering is common within diagnostic imaging to reduce the appearance of noise and edge artefacts and may be necessary for voxel level dosimetry. However as this filtering worsens the spatial resolution and hence partial volume effects MIRD 23 does not recommend it for mean dose estimation [56]. In contrast EANM I-131 mIBG dosimetry guidelines suggest that the clinical reconstruction (with filter) should be used and number of iterations increased until a balance between convergence and noise is obtained [16]. However this difference could be because the EANM mIBG guidelines do not differentiate between the reconstruction requirements for mean and voxel level dosimetry.

The optimal parameters should be determined for the system to be used, with clinically realistic phantom acquisitions or simulations, where the true result is known. For clinical reconstructions around 3 or 5 iterations and 8 to 10 subsets are commonly used for OSEM with Butterworth or Gaussian filters to reduce noise [104]. Koral et al. (2007) and Dewaraja et al (2005) found the total number of counts within source regions continued to increase until about 100 iterations were reached, with the smaller spheres taking longer to converge [105], [106]. For voxel level dosimetry Cheng et al (2013) found that a reduced number of iterations and low pass filtering was needed to reduce the effects of noise and ringing artefacts on dose volume histograms [29]. The optimal parameters depended on the noise-level and object of interest, with a lower number of iterations required for the large objects with few features, compared to smaller objects with fine details (3 iterations and Gaussian FWHM of 1.0 voxel for liver, 25 iterations and FWHM of 1.0 voxel for the kidneys) [29].

2.4.9.Sensitivity Calibration Factors

Sensitivity calibration factors can be used to convert the detected count rate into activity and quantification accuracy within 10-15% has been reported for typical organs of interest following corrections [23]. Calibration factors are typically calculated from phantom acquisitions of known activity following any corrections. However there is no consensus on the choice of calibration protocol, with different choices of phantom and VOI or ROI [2], [107]. For example the MRTDosimetry method suggests imaging a cylindrical phantom and using a VOI with 130% of the phantom radius and 120% of length

[108], while the EANM 131I-mIBG dosimetry guidelines suggest using a VOI with 75% of the phantom size [16]. For the MEDIRAD project a 15cm diameter volume of interest within the centre of a 6L cylinder phantom was used [72] (e.g. 69% of diameter for a 21.6cm diameter Jaszczak phantom). Gregory *et al* 2019 used the plateau from the PVC curve for the SEL-I-METRY trial, based on knowledge of the known activity concentration of the sources [53]. Zimmerman *et al* 2017 used a 4ml, 1.27cm diameter cylinder in air with a large VOI and measurements repeated 3 times, with separate calibrations used for planar and SPECT [55]. A smaller object was used by Zimmerman et al to reduce attenuation effects as it was used for both SPECT and planar imaging. Alternatively, GE recommend planar imaging of a disc source in accordance with the NEMA planar sensitivity method, using the total counts in the image [73]. While Siemens suggest planar images of a long lived NIST calibrated point source (Sn-113 for I-131 imaging) [79].

However the MIRD 24 guidance suggests that for I-131 there is significant septal penetration and collimator scatter, so low attenuation source measurements may only be appropriate where there is highly accurate SPECT corrections [23]. Therefore the use of a phantoms where the level of scatter and attenuation is similar to that of a patient is recommended [23]. Therefore further work could investigate impact of different sensitivity measurement techniques for I-131.

2.4.10. Imaging Time Points

As with blood and bone marrow dosimetry, there is limited evidence for the optimum number and timings of the imaging measurements. EANM guidance on pre-therapy dosimetry for benign thyroid disease suggests that the thyroid tissue may be modelled as a two compartment model as given in Figure 11, with retention, $R_{target}(t)$, and residence time, τ_{target}, calculated using Equations 14 and 15 [18].

$$R_{target}(t) = \frac{\lambda_t}{\lambda_B - \lambda_T}[exp(-\lambda_T t) - exp(-\lambda_B t)] \quad (14)$$

$$\tau_{target} = \int_0^\infty R_{target}(t)\, dt = \frac{\lambda_t}{\lambda_B \lambda_T} \quad (15)$$

Where λ_t is the rate of uptake into the target remnant tissues, λ_B is the rate of elimination from the blood, and λ_T is the rate of elimination from the target remnant tissue. Therefore measurements would ideally be performed with at least two measurements in both the uptake and clearance phases [83].

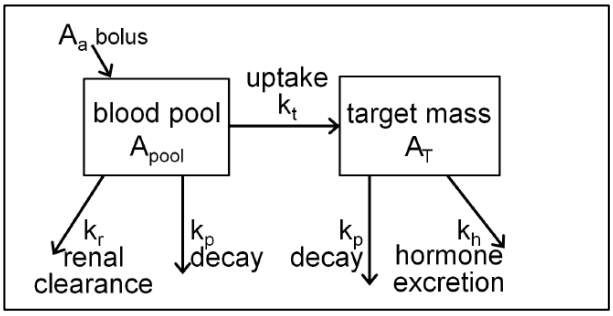

Figure 11. Model of the 131I kinetics in benign thyroid disease with 2 compartments, blood pool and target mass. A_x denote activities, k_x transfer rates. Taken from Hänscheid et al 2013 [18]

Maximal uptake within iodine-avid metastatic lesions has been seen to typically occur at around 24h post administration [109]–[111], so ideally at least two measurements would be performed within this period to model the uptake. For the MEDIRAD NFRP-2016-2017 project the thyroid uptake phase was assumed to be 6-8 hours and therefore imaging was suggested at 4±1h and 8±1h to model this uptake [59]. The system deadtime should be assessed to determine the earliest possible time point for imaging, with 24-48h commonly used for the first time point in literature [34], [52], [77]. 3 to 4 time points are commonly used (likely limited by camera availability), with a late time point at 72-216h (3-9 days) [34], [52], [77]. The excretion effective half-life of I-131 is expected to be approximately 7 days for I-131, therefore a final scan at 6-8 days has been recommended [59]. The variation in time of final measurement may be due to the length of inpatient stay (depending on national legislation and local protocol) and patient ability to return for late time point imaging following discharge (catchment area dependent). For the MEDIRAD project imaging at 4±1h, 8±1h, 24±2h, 2d, 3d, 4-5d, and 6-8d following administration was used [59], however 7 imaging time points is likely to be challenging for routine use in many sites.

2.5. S-factors

The S-factor (or dose factor), can be calculated in a number of different ways. Historically, this has been calculated using Monte Carlo modelling of stylised computational phantoms, such as the Chirsty-Eckerman phantom shown in Figure 12. This method was used for the MIRDOSE software [112] and its replacement the FDA approved OLINDA/EXM v1.0 software [26], which was made widely available and so should be accessible in most Nuclear Medicine departments. More recently the S-factors have been calculated using non-uniform rational B-splines (NURBS) computational models such as

those shown in Figure 12, which are voxel based, more anatomically realistic phantoms [113]. Doses calculated using S-factors based on both the older and NURBS phantoms can be calculated using the OLINDA 2.0 software [113], which is now distributed commercially by Hermes. The organ doses calculated from OLINDA software are based on standard sized patients and so application to a specific patient must be performed with caution [113]. Photon self-irradiation absorbed fraction has been shown to vary directly with the cube root of the mass in cases where the mean path length of photons is large compared with the diameter of the source organ [20], [26]. Therefore, this can be used to apply calculations to a specific patient. For the cross-absorbed dose, the S value is considered to be independent of the mass and therefore scaling is not typically performed [20], [26]. Typically for beta emitters the absorbed fraction is taken to be 1 within the organ and 0 outside the organ [112]. OLINDA also allows the dose to tumours to be calculated using the dose to unit density spheres for defined masses, and interpolation is required for masses in between those given [112], [113].

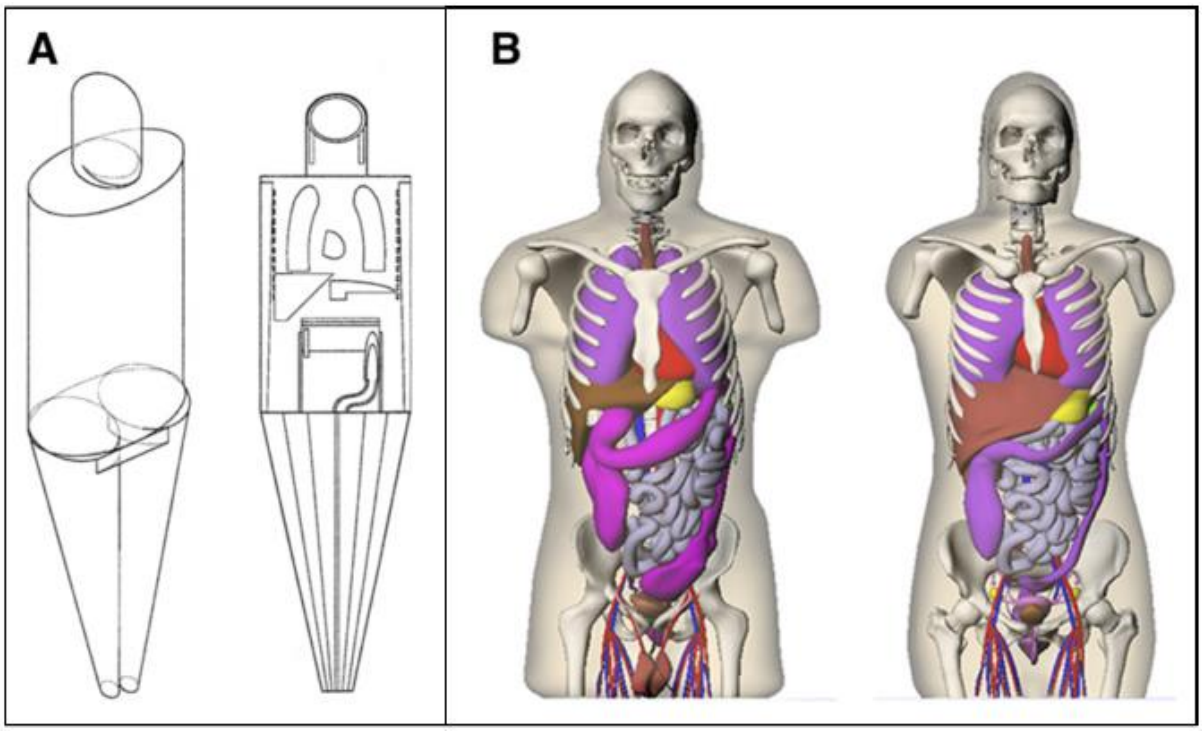

Figure 12. (A) Cristy–Eckerman stylized computational phantoms. (B) NURBS realistic voxel- based phantoms. [Taken from Stabin and Siegel (2018) [113]*].*

2.6. Conclusions

A summary of different techniques used for dosimetry in literature have been presented and their practical implementation has been discussed. Bone marrow dosimetry based on the EANM bone marrow dosimetry guidelines is suggested [21], with blood and retention measurements at around 2, 6, 24, 48 and 96-164 hours after administration. For other dosimetry, SPECT/CT imaging at a minimum of 4-9 and around 24 hours (deadtime dependent), 48 and 96-164 hours post injection is suggested based on literature. If SPECT/CT imaging at multiple time points is not possible, SPECT/CT could be performed at a single late time point and planar geometric mean imaging at other time points. Further work is required to investigate the optimum number and timing of measurements, however this requires dosimetry to have been implemented and so is outside the scope of this work.

For bone marrow dosimetry, whole body retention measurements measurement methods were reviewed. This review suggested a probe should be used, with late time point measurements where possible and probes should have sufficient sensitivity be able to acquire 10^5 net counts. Guidelines suggested the geometric mean of anterior and posterior measurements should be used but the benefit over anterior only measurements was not clear, this has been investigated further in Chapter 3.4. Performing late time point probe measurements after the patient has been discharged is recommended but the impact on residence time calculation was not clear and may be logistically challenging. Therefore an investigation into the impact of an additional late measurement was performed and is given in Chapter 3.6. The use of whole body gamma camera images for the late time point measurements was suggested as an area for investigation to assist with the logistical issues. An investigation into the feasibility of this method is given in Chapter 3.7. Further work investigating correlation between calculated absorbed dose to blood/bone marrow and patient haematological response is required, however implementation of dosimetry is first required and therefore it is outside of the scope of this thesis.

Methods for performing SPECT reconstruction were reviewed along with methods for optimising the reconstruction parameters. This found the optimum reconstruction parameters should be determined for the system using phantom and patient images. For the planned organ level dosimetry it was found that no smoothing filter and a large number updates should be used and the optimum parameters investigated. This was performed, with the findings detailed in Chapter 4.4. If implementation of voxel level

dosimetry was required then further optimisation of parameters for software and organs of interest would need to be performed, with a reduced number of updates required to due to the smaller size of voxels.

Partial volume effect correction was seen to be required for dosimetry and methods for performing this were reviewed. The most practical PVC method is likely to be determining volume-based correction factors from imaging a phantom containing spheres or cylinders with different diameters. It was not clear whether spheres or cylinders should be used and the equation to use for the fit based on literature, therefore this was investigated further and details are given in Chapter 4.6.

Deadtime and sensitivity calculation methods were reviewed and it was concluded that these should be determined for the system using phantom acquisitions. These calibrations were performed and details are given in Chapters 4.3 and 4.5. For sites with GE systems “fast” counting mode is required due to detector deadtime, which is not well documented so a need for further characterisation was identified. Investigations into the change in count rate seen for the different energy windows with increasing activity, impact on sensitivity and activity recovery were performed and are given in Chapters 4.3, 4.5 and 4.6 respectively.

Patient mean organ doses are likely to be determined from time activity curves inputted into OLINDA/EXM 1.0 which requires fitting to interpolate between the different tissue masses given, this was performed for spherical objects and is given in Chapter 4.7. However, if software is available that will allow voxel-based dosimetry then this should be used as it will be more patient tailored. Using these methods, it should be possible to practically implement dosimetry for I-131 patients with differentiated thyroid carcinoma.

Areas for further work which were outside of the scope of this work were identified which includes errors caused by using the planar-SPECT/CT hybrid method compared to SPECT/CT; development of more commercial software including models of septal penetration and geometric photons at different distances for hexagonal shaped holes; development of commercial software to perform partial volume corrections; optimal reconstruction parameters for I-131 patients for voxel dosimetry; impact of dosimetry on patient outcomes.

3. Blood and Bone Marrow Dosimetry Investigation

3.1. Introduction

For I-131 NaI therapy the key organ at risk is the bone marrow and the dose it receives is commonly calculated using whole body and blood retention measurements [20], [21]. The whole body retention measurements are typically performed using an external probe and blood retention is calculated through taking blood samples and measuring them in a gamma counter [20], [21].

At the RSCH whole body probe measurements were routinely performed using a Thermo Electron Corporation MC20PET AMB Geiger detectors with a Mini-Instruments 6-90 series scalar rate meter. Two shielded therapy rooms were available on the ward for inpatient treatments. The Geiger detectors were positioned in the ceiling above the patient beds in the treatment rooms and anterior measurements were performed with the patient lying supine on the bed. EANM Guidance on bone marrow dosimetry suggests that probe measurements should be performed at least 2m from the patient to reduce positioning errors and the net counts measured using the probe should be greater than 10^5 to ensure sufficient count statistics [20], [21]. The Geiger probe used for whole body measurements did not meet this condition (~10^3 counts over 60s at 3m from a patient administered with 1.1GBq I-131 NaI) and late time point measurements around 7 days after therapy were found to be at background levels. Therefore the use of a Radhound SS404AL scintillation monitor (Southern Scientific) was investigated, as they are commonly used for contamination monitoring within Nuclear Medicine departments. While the Radhound monitor had previously undergone quality control testing in accordance with relevant guidance [114], additional linearity testing relevant to I-131 patient monitoring was performed and is detailed in Chapter 3.3.

The literature review in Chapter 2 identified investigations into the impact of conjugate view measurements on whole body counts and residence time; impact of whole body background correction methods; impact of late measurement time points and investigation into the use of a gamma camera for a late time point measurement as areas for further work. These were investigated through performing patient measurements and are detailed in Chapters 3.4 to 3.6. Similar methodology was used in these chapters for the calculation of whole body residence time, therefore the general methodology is given in Chapter 3.2.

For blood residence time calculation, blood samples are commonly measured in a gamma counter and the sample activity concentration is calculated using a sensitivity factor for that isotope and geometry [20], [21]. Therefore a sensitivity calibration was performed using 1ml I-131 samples and details are given in Chapter 3.8.

3.2. General Methodology for Whole Body Residence Time Calculation

46 patients undergoing radioiodine treatment for thyroid carcinoma at RSCH between February 2020 and January 2021 had Radhound probe measurements performed. 5 patients were excluded from analysis as an incorrect Radhound monitor was used or it wasn't clear which monitor had been used. One patient was excluded as it was found that their worn clothes had been left near the monitor for some of the measurements, substantially affecting the background. Another patient was excluded due to a set of outlier results for one time point, suspected to be due to the deadtime correction being turned off. Therefore 39 patient's results were analysed.

Anterior and posterior whole body probe measurements were performed in the patient therapy room on the RSCH ward immediately and one hour after administration, then at the start and end of each working day until the patient was discharged. Measurements were also performed immediately prior to gamma camera scanning in the RSCH Nuclear Medicine department. If the patient had been discharged from the ward at the point of scanning, probe measurements were performed in the Nuclear Medicine department. In order to perform patient measurements in both the therapy room (inpatient measurements) and late time point measurements in the Nuclear Medicine department prior to imaging (outpatient measurements), the monitor was positioned on a trolley which could be moved between areas. The patient was positioned 3m from the trolley to reduce errors due to positioning and the dose to the operator, with marks on the floor/walls for the patient and trolley being used to reduce variability (see Figure 13). Measurements were performed with both Geiger and Radhound monitors present to validate the changeover.

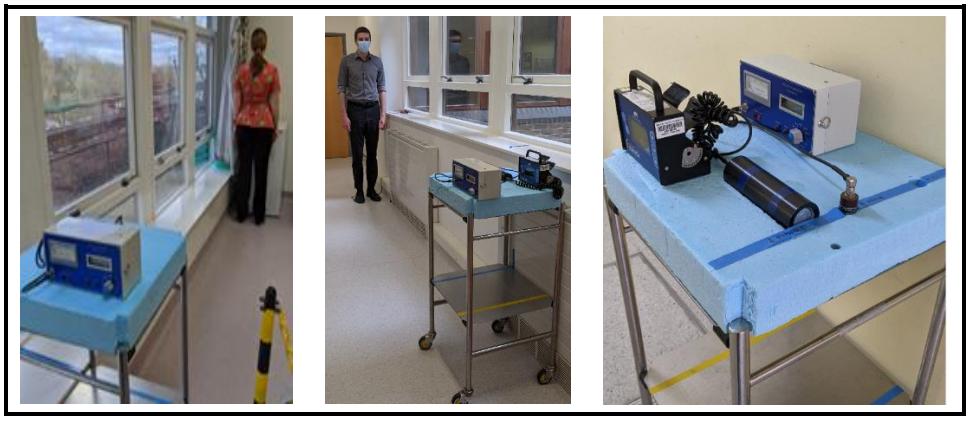

Figure 13. Revised patient positioning for whole body retention monitoring. For inpatient measurements (left) and outpatient measurements (middle), with Radhound and Geiger detectors positioned on a trolley (close up on right).

Three 60s patient measurements were performed with the monitors and the results recorded. The Radhound deadtime correction was enabled and the system default deadtime of 10µs was used. Measurements were typically performed immediately after administration, approximately 1 hour post administration and then in the morning and afternoon while they were inpatients (typically 1 to 4 days depending on patient I-131 clearance). Patients were typically administered with I-131 on the Monday and had gamma camera imaging on the Thursday if administered with 1.1GBq or 5.5MBq I-131 and on the following Monday if administered with 3.7GBq I-131, in accordance with local protocol. Additional whole body measurements were performed immediately prior to imaging, using the inpatient method or outpatient method if the patient had been discharged. Inpatient background measurements were typically performed prior to administration and at discharge prior to room decontamination, without the patient present. Outpatient background measurements were performed without the patient present immediately prior or after the patient measurement. The start time for the measurements was taken to be the first measurement start time.

For each set of measurements the average count rate was calculated. An additional non-paralysable deadtime correction was then performed using the deadtime determined in Chapter 3.3. The net average deadtime corrected count rate was then calculated. Unless stated otherwise, the background for inpatient measurements was calculated using linear interpolation of the background inpatient measurements performed. The geometric mean was then calculated from the anterior and posterior net background corrected count rates in accordance with Equation 11.

Bi-exponential clearance fitting was performed using the anterior or geometric mean corrected count rate data, $C(t)$, at measurement times post administration, t, to determine the fitting constants C_1, C_2, λ_1 and λ_2 given in Equation 16.

$$C(t) = C_1 e^{-\lambda_1 t} + C_2 e^{-\lambda_2 t} \quad (16)$$

Sensitivity factors, Q_{WB}, were then calculated to convert the whole body count rates $C(t)$ to whole body activities $A_{WB}(t)$ by taking the calculated count rate at $t = 0$ to be directly proportional to the administered activity, A_0, as given in Equations 17 and 18 below.

$$Q_{WB} = \frac{C_1 + C_2}{A_0} \quad (17)$$

$$A_{WB}(t) = \frac{C(t)}{Q_{WB}} \quad (18)$$

The whole body residence time, τ_{WB}, was then calculated using Equations 9 and 10.

The bi-exponential fitting constants C_1, C_2, λ_1 and λ_2 were determined iteratively using Solver in Excel by minimising the root mean squared error (RMSE) between the measured and fitted net counts data as given in Equation 19, with conditions that the fitting parameters λ_1 and λ_2 must be greater than the I-131 physical decay constant and the fitting parameters C_1 and C_2 must be greater than 0.005.

$$RMSE = \frac{\sum_{i=1}^{N} \left(R_{O,i}^{fit} - R_{O,i}^{measured}\right)^2}{N} \quad (19)$$

As the bi-exponential iterative fit depended on the starting fit parameters, curve stripping was used to determine these initial parameters. The curve stripping first performed an exponential fit to the last two data points to calculate λ_1 and C_1. The estimated net count rate, C_{est}, was then calculated using these parameters ($C_{est}(t) = C_1 e^{-\lambda_1 t}$). The "stripped" counts, $C_{strip}(t)$, were then calculated ($C_{strip}(t) = C(t) - C_{est}(t)$) and another exponential fit was then performed for positive $C_{strip}(t)$ counts to calculate λ_2 and C_2.

3.3. Radhound Probe Deadtime Characterisation

3.3.1. Methods

While the Radhound monitor had undergone full local commissioning and annual tests in accordance with NPL (National Physical Laboratory) Good Practice Guide 14 [114] for use in contamination monitoring, additional testing was required to determine if it could be used for patient whole body retention measurements [16]. Deadtime characterisation

was performed for I-131 in accordance with the EANM I-131 mIBG dosimetry guidelines [16], using an I-131 source within a scatter medium. The probe was positioned a distance of 2m from an I-131 capsule within a thyroid neck phantom, with reproducible positioning as shown in Figure 14.

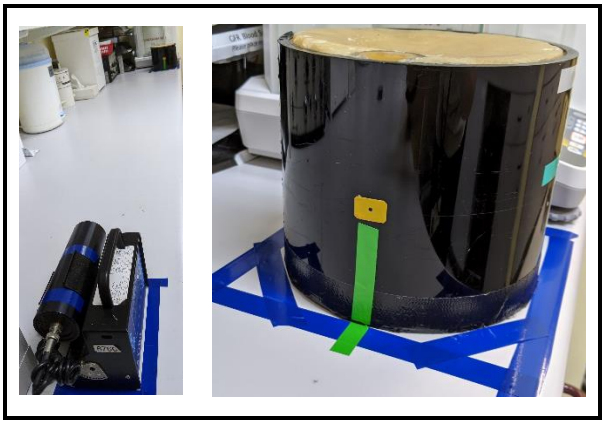

Figure 14. Experimental set up for Radhound I-131 deadtime testing. The monitor was positioned 2m from an I-131 capsule positioned within a thyroid neck phantom. Tape was used for reproducible positioning of the probe, unit and phantom.

Two I-131 NaI capsules were separately measured at multiple time points as they decayed, giving activities within the phantom of 2.15MBq to 3500MBq. Deadtime measurements were performed with the probe at 2m from the I-131 rather than the 3m used for patients. This was due limitations on space within the testing room and I-131 capsule activity available. Therefore using the inverse square rule, the experimental count rates seen were equivalent to those expected for around 5MBq to 7800MBq I-131 patient whole body activity. The activities of the capsules were measured in a Capintec radionuclide calibrator (Mirion Technologies) prior to the start of testing and activity at time of testing was calculated using decay correction. On each testing day, for each capsule, three 60s measurements were taken, with the Radhound deadtime correction function set at the default of 10µs and the mean counts per second calculated. Background measurements with no activity present were also performed using the same method and the net average counts per second were calculated. The sensitivity with no deadtime, Q_{RH}, ("baseline cps/MBq") was calculated from a linear regression of the net average cps/MBq as a function of activity, performed using the low activity capsule measurements in the range of 2MBq to 122MBq. The "true" count rate, $C_{T,i}$, was calculated from the baseline cps/MBq, the capsule activity at time of measurement, A_i and mean background at time of measurement, $C_{bg,i}$ as given in Equation 20.

$$C_{T,i} = Q_{RH}\, A_i + C_{bg,i} \qquad (20)$$

A plot of measured count rate as a function of "true" count rate was produced and it was found that increasing input count rates produced greater deviations from the line of identity. Therefore the default deadtime setting of 10µs was not correct for I-131 so any measurements made with this setting would need further deadtime correction. Paralysable and non-paralysable fits were used to calculate the observed count rate based on the "true" count rate using in accordance with Equations 4 and 5 respectively. The deadtime and uncertainty for each fit was calculated iteratively using OriginPro, to minimise the RMSE as given in Equation 19. The fit error was also calculated, using Equation 21 below.

$$Fit\ error = \frac{R_{O,i}^{fit} - R_{O,i}^{measured}}{R_{O,i}^{measured}} \qquad (21)$$

3.3.1. Results

The calculated Radhound deadtime using paralysable and non-paralysable fits is given in Table 1. The RMSE for the fits is also given along with the calculated baseline net count rate per unit activity.

A plot of observed count rate as a function of the calculated “true” (input) count rate is given in Figure 15 for both measured data and deadtime fit curves, with the line of identity given for comparison. A plot of the fit error is also given as a function of capsule activity in Figure 16.

Table 1. The calculated Radhound deadtime using paralysable and non-paralysable fits from measurements 2m from an I-131 capsule within a thyroid neck phantom. The RMSE for the fits is also given along with the calculated baseline count rate per unit activity.

Mode	Baseline (cps/MBq)	Calculated deadtime, τ (µs)		RSME	
		Paralysable Fit	Non-Paralysable Fit	Paralysable Fit	Non-Paralysable Fit
10µs Radhound deadtime correction on	9.75±0.03	8.68±0.09	9.89±0.07	114	74

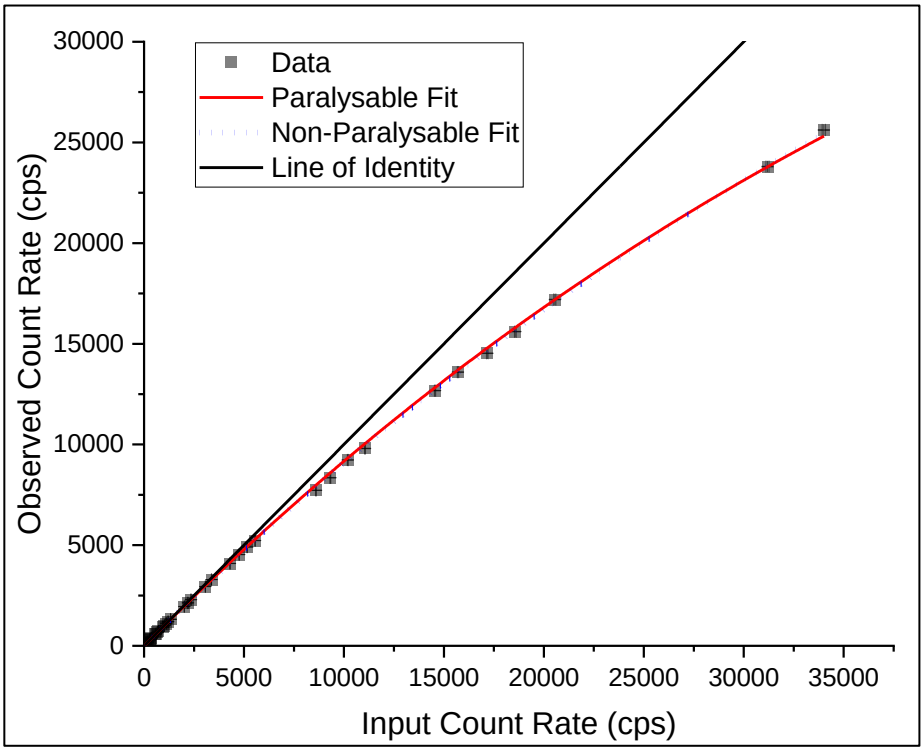

Figure 15. A plot of observed count rate as a function of the calculated input count rate for a Radhound positioned 2m from an I-131 capsule within a thyroid neck phantom.

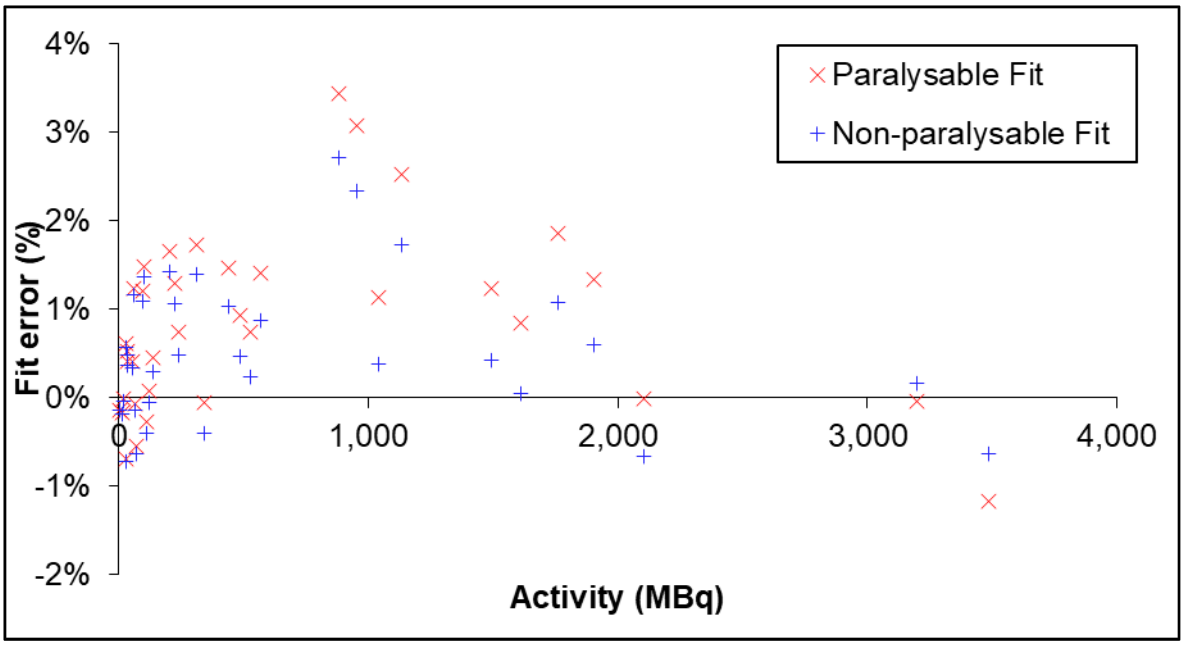

Figure 16. Plot of fit error for paralysable and non-paralysable deadtime models as a function of activity of the I-131 capsule positioned within a thyroid neck phantom 2m from the Radhound.

3.3.2. Discussion

A plateau, turnover or saturation point was not reached for Radhound count rates measured. This indicates that a Radhound may be used for patient whole body retention monitoring if the patient is at 3m from the monitor and appropriate deadtime corrections

are performed. Deadtime calibration measurements were performed with the probe at 2m from the source rather than the 3m used for patients. This was not thought to have a significant impact on the calibration, however further work could be performed with the phantom and probe in the positions used for patient measurements to investigate this further.

The Radhound demonstrated low fit errors with both paralysable and non-paralysable fits, with the non-paralysable fit giving a slightly lower RMSE. Therefore if measurements were acquired with the default Radhound 10µs deadtime correction on, then the deadtime could be calculated using a non-paralysable fit. The lower errors with a non-paralysable fit is unexpected as the system would normally be expected to demonstrate paralysable deadtime. However, it is noted that the measurements were performed with the default Radhound 10µs deadtime correction on, which could be affecting the results. Ideally further deadtime correction would not need to be applied in addition to the deadtime correction set on the system. Therefore further investigations could be performed into the characterisation of deadtime for Radhounds with I-131 with higher activities, with the deadtime correction turned off and also with a more I-131 appropriate deadtime set on the Radhound.

3.4. Impact of Geometric Mean Retention Measurements

3.4.1.Methods

Guidelines suggest that both anterior and posterior whole body retention measurements should be performed and the geometric mean values should be used to calculate the whole body residence time [16], [20], [115]. However anterior only measurements are typically performed for determining patient discharge and the additional posterior measurements are more time consuming. Therefore the impact of using geometric mean measurements compared to anterior only was investigated.

The first measurement time point immediately after I-131 administration was disregarded as the counts were found to change during both the anterior and posterior measurements due to gastrointestinal transit and both patient orientations could not be measured simultaneously. The net background corrected anterior and geometric decay corrected mean count rates for the remaining measurements were then calculated. The percentage difference between the anterior and geometric mean count corrected rates was then calculated using Equation 22 below, the results tabulated and a histogram plotted to investigate the impact for different time ranges.

$$Anterior\ vs\ Geometric\ Mean\ \%\ Difference = \frac{Anterior - Geometric\ Mean}{Geometric\ Mean} \quad (22)$$

The whole body residence times using the anterior and geometric mean methods, $\tau_{WB,Ant}$ and $\tau_{WB,GM}$ were calculated using Equations 9 and 10 with bi-exponential fitting and a Bland-Altman plot was produced to compare the residence times.

The difference between the whole body residence times using the different methods was calculated for each patient and from this the mean difference was found. A paired 2 tailed t-test was then performed to determine if there was a statistically significant difference between the methods.

3.4.2. Results

The median, minimum and maximum percentage difference between the anterior and geometric mean corrected whole body count rates are given in Table 2 for measurements at 0.25, 0.25 to 2 and greater than 2 days post administration and a histogram of the percentage difference for these different time ranges if given in Figure 17.

Table 2. Percentage difference between anterior and geometric mean probe whole body corrected count rates. Given for three measurement time periods post administration.

Time range [days]		**≤0.25**	**0.25-2.00**	**>2.00**
% Difference between anterior and geometric mean corrected count rates	Median	4.00%	2.62%	2.81%
	Minimum	-4.77%	-2.95%	-3.56%
	Maximum	15.52%	10.61%	15.07%

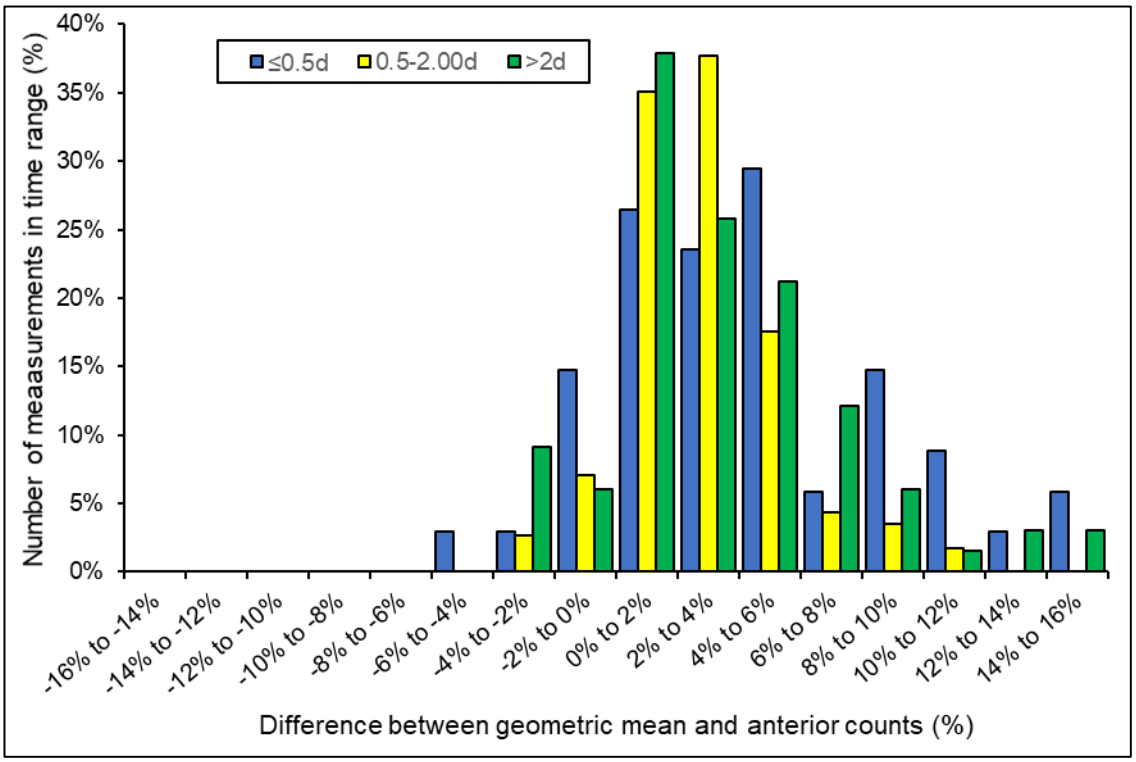

Figure 17. Histogram showing percentage difference between anterior and geometric mean whole body corrected count rates for three measurement time periods post administration.

A Bland-Altman plot comparing the difference between the whole body residence times calculated using the anterior and geometric mean methods is given in Figure 18. The mean difference in residence times was -10.5d and a statistically significant mean difference was not seen (P = 0.247). The median percentage difference in residence time was -0.5% (i.e. $\tau_{WB,Ant}$ slightly lower than $\tau_{WB,GM}$), with a minimum difference of -6.3% and maximum difference of 5.0%.

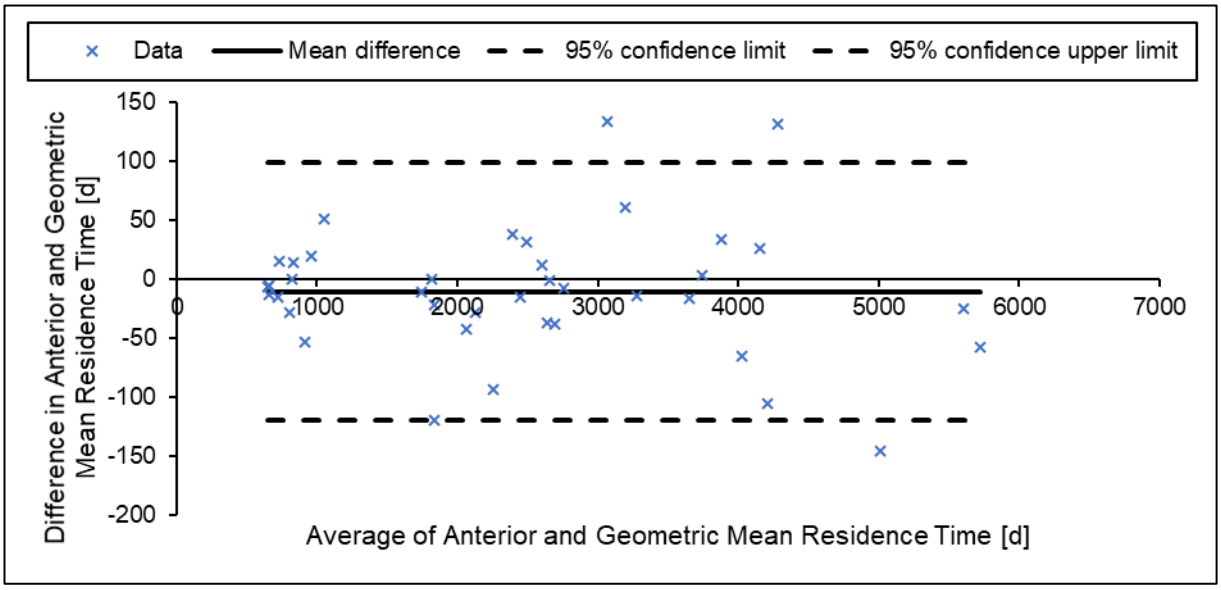

Figure 18. Bland-Altman plot showing the difference between the residence times calculated with anterior and geometric mean corrected whole body count rates.

3.4.3. Discussion

The histogram and table of difference between anterior and geometric mean Radhound counts given in Figure 17 and Table 2 respectively show there were typically higher counts anteriorly compared to posteriorly. This is to be expected as the I-131 typically accumulates in the thyroid tissue and bladder, which are anterior within the body. The median difference and histogram distributions were similar across all time ranges assessed, suggesting that from 1 hour post administration the difference between anterior and geometric mean counts remains fairly consistent.

The Bland-Altman plot comparing residence times with anterior and geometric mean measurements given in Figure 18 shows a mean difference in whole body residence times of -10.5d (-119 to 98 d 95% CI). A median difference of -0.5% was also seen, indicating that the anterior counts cause an underestimation in the residence time compared to the geometric mean counts. However mean difference deviation from zero was not found to be statistically significant at $P<0.05$, with a P-value of 0.247 measured. There were 4 patients who had measurements outside of the 95% confidence interval and more data are required to investigate this further. However, the evidence suggests that while best practice would be to perform assessment of geometric mean counts, in the majority of cases anterior measurements only are unlikely to make a clinically significant impact on the whole body retention. Therefore if there is a patient who would struggle to have both

anterior and posterior measurements, then anterior only should be performed and an additional uncertainty of 6% could be accounted for in whole body residence time.

3.5. Impact of Whole Body Background Measurement Method

3.5.1.Methods

In order to estimate the impact of using an interpolated background method with background inpatient room measurements before treatment and at discharge, the whole body geometric mean residence time using "minimum background" and "maximum background" measurements was calculated. For the "minimum background" method the background during the inpatient room measurements was taken to be the value measured before treatment. For the "maximum background" method the background was taken to be the background measured at discharge prior to inpatient room decontamination. The whole body residence times were calculated using the minimum, maximum and interpolated background methods using inpatient data only ($\tau_{WB,min\ bg}$, $\tau_{WB,max\ bg}$ and $\tau_{WB,interp\ bg}$ respectively). Where additional outpatient measurements were performed, the residence times were also calculated using these measurements. The difference between the minimum or maximum and interpolated residence times were then calculated. This was performed using inpatient measurements only and also with outpatient measurements included, if acquired. Histograms of the difference in calculated residence times were then plotted to enable comparison.

Of the 39 patients assessed in the audit 13 were missing inpatient background measurements and so were excluded from this analysis. An additional patient was excluded from the analysis as only one patient measurement was performed on day of therapy, immediately after administration and only 3 further measurements were performed while they were an inpatient. This left 25 patients for the inpatient measurement analysis and 16 for the analysis including outpatient measurements.

3.5.2.Results

Histograms of the difference between residence times using the different background correction methods are given in Figure 19, with results for inpatient measurements only given along with results using both inpatient and outpatient measurements.

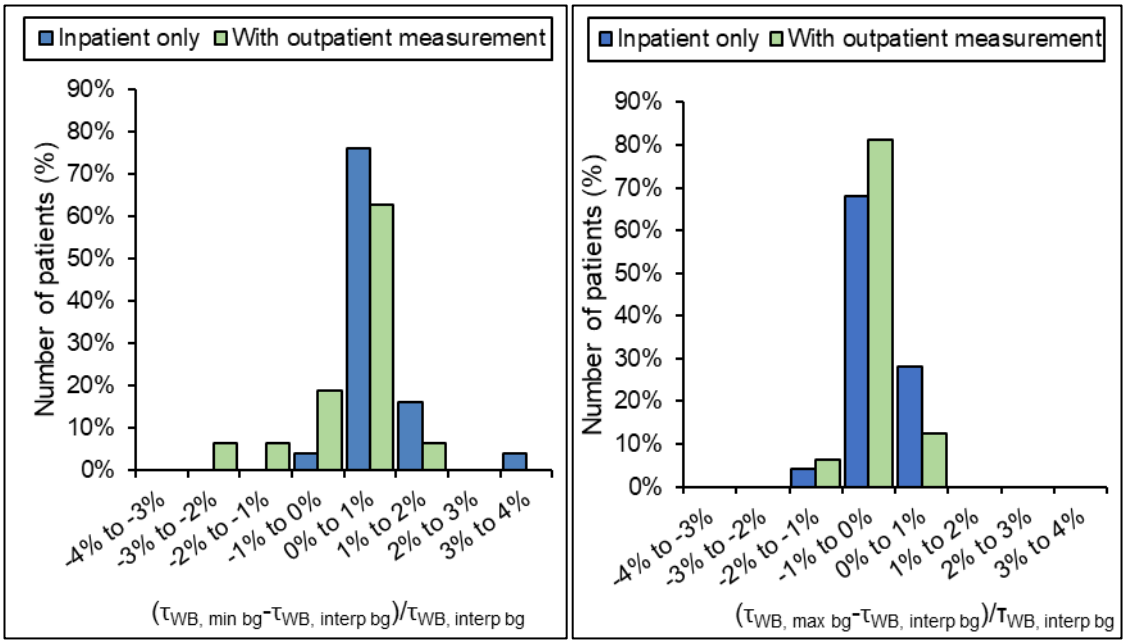

Figure 19. Histograms comparing difference in calculated whole body residence times using minimum or maximum background measurements compared to the interpolated background measurement methods. The difference using the minimum background method $\tau_{WB,min\ bg}$ is given on the left and the difference using the maximum background method, $\tau_{WB,max\ bg}$ is given on the right. This is shown using inpatient only measurements and with the inclusion of additional outpatient measurements at the time of the scan, where performed.

3.5.3. Discussion

From Figure 19 it can be seen that residence times calculated using inpatient measurements only with the background measurements before therapy were typically higher compared to the interpolated background method. This is likely due to the higher count rates calculated with a lower background and therefore larger area under the curve. There was one case there the residence time was lower (-0.02%), however in this case the background level at discharge was similar to the pre-therapy background level so the small error is likely due to Poisson noise within the measurements and the iterative nature of the bi-exponential fit. There was one case where a 3.8% difference was seen, where the background measurement at discharge was found to be high (190cps, compared to 8cps prior to therapy and 613cps with patient prior to discharge). When the fit was expanded to include late time point outpatient measurements, 31% of patients were seen to have residence times which were lower with the minimum background method compared to the interpolation method. This is likely due to the later inpatient measurements being overestimated and so a greater apparent second phase clearance being seen when the outpatient measurement was included.

Using the maximum background method the opposite effect was seen when using the inpatient measurements only. However when the outpatient measurements were included less of a change was seen because unlike with the minimum background method, for the maximum background method the final inpatient measurement was sufficiently background corrected.

Using maximum or minimum background methods was found to result in a -2.2% to 3.8% difference compared to the interpolation method. Therefore the background subtraction method was seen to make a small difference to the whole body retention measurements. Hence, while ideally background measurements should be performed at each patient measurement, it does not appear to have a large impact.

The largest differences in retention measurements were seen when the background following therapy was high. Further investigation found that some patients were leaving their worn clothes and used meal trays on the shelf near where the monitor was positioned. This highlights that where limited background measurements are performed, care must be taken to ensure that items which may cause high background are placed as far away from the measurement areas as possible during all measurements.

Further work could investigate the impact of performing background measurements for every patient measurement while ensuring that items that are known to cause high background are removed where possible.

3.6. Impact of Late Time Point on Whole Body Residence Time

3.6.1. Methods

To investigate the impact a late whole body retention measurement has on the residence time, the impact seen for patients with imaging at 7 days post therapy was investigated. Patients were excluded from analysis where a measurement 1 hours post administration was not performed or where background measurements were not performed. This left 8 patients included in the analysis.

The whole body residence time was calculated both using the inpatient measurements only ($\tau_{WB,early}$) and with the scan time outpatient measurements included ($\tau_{WB,late}$). The percentage difference between the measurements was calculated and a histogram plotted to compare the difference in residence times. All patients were high risk ablation

patients administered with 3700MBq±10% I-131 and were inpatients for 1.8 to 2.8 days (1.9 days median).

3.6.2. Results

A histogram of the difference in whole body residence times using inpatient measurements for 2 to 3 days post therapy, compared to those including an additional late time point 7 days post therapy is given in Figure 20. The median, minimum and maximum differences in residence times were -2.2%, -5.9% and -0.5% respectively.

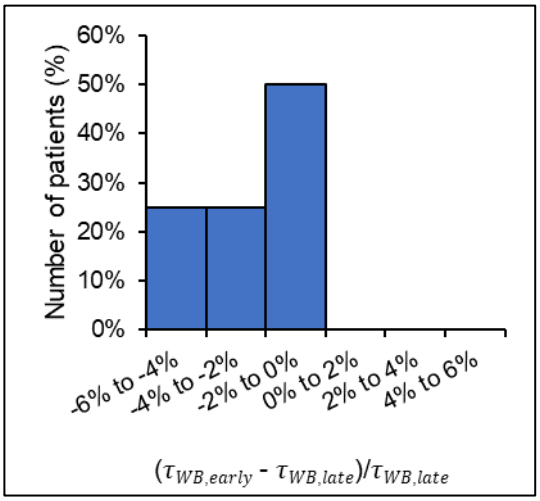

Figure 20. Histogram showing percentage difference in whole body residence times calculated using "early" and "late" measurement time points. Where $\tau_{WB,early}$ is the whole body residence time calculated using inpatient measurements only and $\tau_{WB,late}$ is the residence time calculated including an additional "late" measurement 7 days post therapy.

3.6.3. Discussion

From Figure 20 it can be seen that the addition of a late time point 7 days post therapy caused either little difference or increase in whole body residence time, as expected due to sampling of an additional slower late clearance phase where present. Differences in residence times of up to 5.9% were seen when the late time point was included, indicating that dosimetry would benefit from the inclusion of a late measurement. However for 50% of patients the difference was less than 2%, which is unlikely to be clinically significant. Therefore sites which treat patients who live further away and imaging at 7 days post therapy is logistically challenging could determine that this late time point does not add sufficient benefit and instead account for a potential under estimate in dose of up to ~6%.

This analysis only included 8 patients, therefore further work is required to investigate the impact with a larger cohort of patients. The cohort also only included patients who were high risk receiving their first ("ablation") treatment, therefore further work could investigate the impact of different patient groups. The only late time point used was at 7 days post therapy, therefore further work could investigate measurements at other time points to determine the best choice for late time point measurements.

3.7. Use of Gamma Camera for Late Time Point Whole Body Retention

3.7.1. Methods

Whole body retention measurements are often performed using a probe in the ceiling above the bed in the patient therapy room. However, for late time point measurements the patient will likely have been discharged and another patient may be using the therapy room. Late time point measurements using a gamma camera are recommended for tumour dosimetry and so could be a practical substitute for the whole body probe measurements. Therefore an investigation was performed to determine if a conversion factor could enable gamma camera imaging to be used for a late time point retention measurement, in conjunction with probe measurements.

Gamma camera whole body imaging was performed using the GE Optima system in normal mode with 5cm/min scan speed, HEGP collimators, 256x1024 matrix, a "photopeak" window of 364keV±10%, "lower" scatter window of 318ekV±3% and "upper" scatter window 413keV±3%. Whole body probe monitoring was performed just prior to imaging and the patient was asked to not go to the toilet between the probe measurement and whole body gamma camera scan. Patients were excluded where a measurement around 1 hour post administration was not performed, the patient was known to go to the toilet between probe measurement and imaging or the probe measurement was not within 1 hour of imaging (due to the likelihood of the patient going to the toilet). This resulted in 26 patients being analysed for this work.

On the planar images, whole body and background ROIs were drawn using GE Xeleris software for each patient and the total counts and number of pixels was recorded for each ROI, as shown in Figure 21. The background ROIs were drawn towards the feet to reduce the influence of scatter and care was taken to avoid overlap with the patient outline.

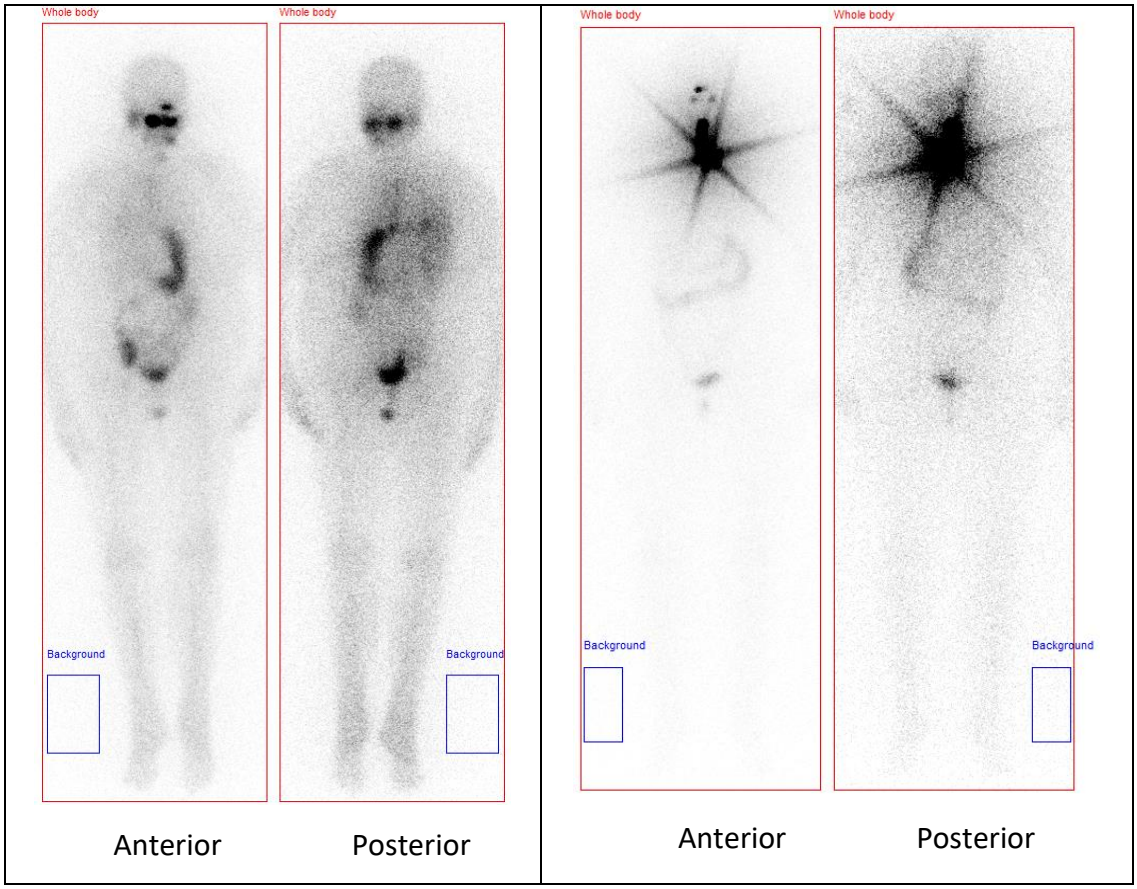

Figure 21. Whole body and background ROIs outlined on planar patient photopeak post I-131 therapy gamma camera images. Shown for a patient with high BMI (left) and for a patient with a prominent septal penetration artefact (right).

The net total counts in each image were calculated as given in Equation 23 below and the geometric mean gamma camera counts were calculated from the net anterior and posterior counts in accordance with Equation 11.

$$Net\ image\ counts = \left(\frac{WB\ ROI\ counts}{WB\ ROI\ pixels} - \frac{Bg\ ROI\ counts}{Bg\ ROI\ pixels}\right) \times WB\ ROI\ pixels \quad (23)$$

The probe anterior, posterior and geometric mean counts were decay corrected to the scan start time, taken from the DICOM header. A bi-exponential fit was performed using the geometric mean probe measurements to determine the estimated activity at the scan start time. Plots of gamma camera net counts ($C_{CG\ net\ counts}$) as a function of probe counts ($C_{RH\ net\ counts}$) were produced for the anterior, posterior and geometric mean views. For each view linear regression fits were performed in Excel using patient data where the estimated internal activity at time of scan was less than 1.5MBq (11 patients) to give fitting parameters *m* and *c*, as given in Equation 24.

$$C_{RH\ net\ counts} = m \times C_{CG\ net\ counts} + c \quad (24)$$

The linear regression fit from the patients with low estimated internal activities of 1.5MBq were then used to estimate the whole body Radhound counts from the measured patient gamma camera net counts and the RMSE as well as error in fit were estimated. The low activity patient data was used to avoid the potential influence of deadtime.

3.7.2.Results

The gamma camera to Radhound counts calibration fit parameters using Equation 24 are given in Table 1 along with the Radhound counts fit error. Examples of the graphs of Radhound net count rate and estimated counts fit error as a function of gamma camera net counts are given in Figure 22 and in Figure 23 for the geometric mean counts.

Table 3. The fit parameters and errors in fit for the gamma camera-Radhound calibration. Given for anterior, posterior and geometric mean views.

View	Fit Parameters		RMSE	% Radhound Counts Fit Error		
	m	c		Median	Minimum	Maximum
Anterior	0.0004	0.030	114	-3.7%	-24.5%	22.4%
Posterior	0.0005	-0.008	69	-6.7%	-26.4%	23.3%
Geometric Mean	0.0005	-0.407	85	-5.5%	-21.7%	20.4%

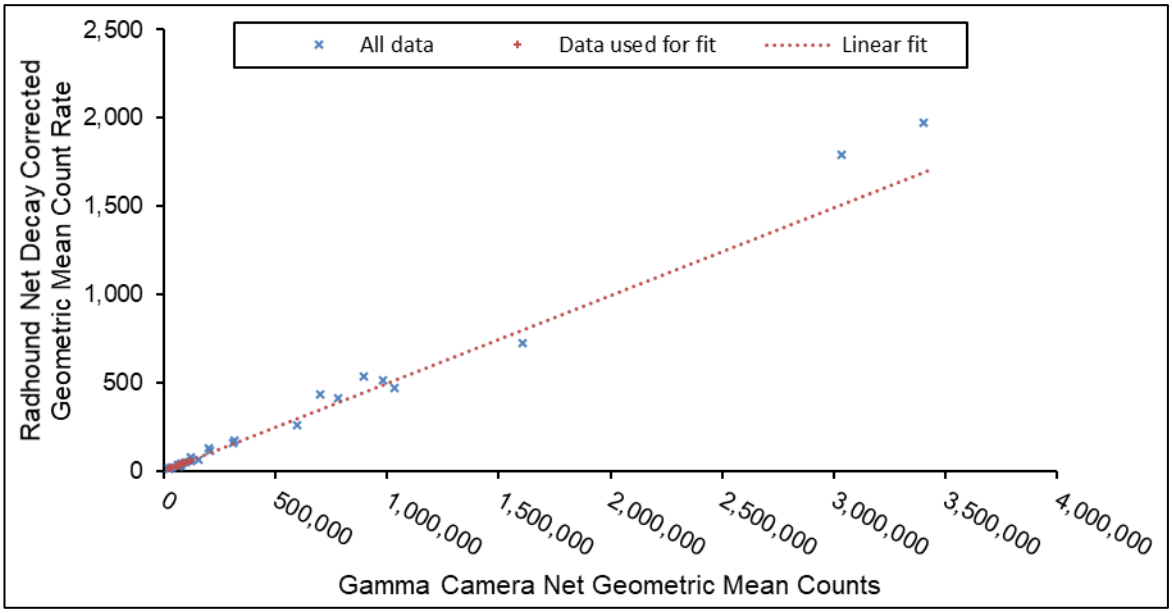

Figure 22. Plot of measured gamma camera net counts as a function of Radhound net decay corrected counts rate using geometric mean data. A linear fit line is given, extrapolated from low counts data.

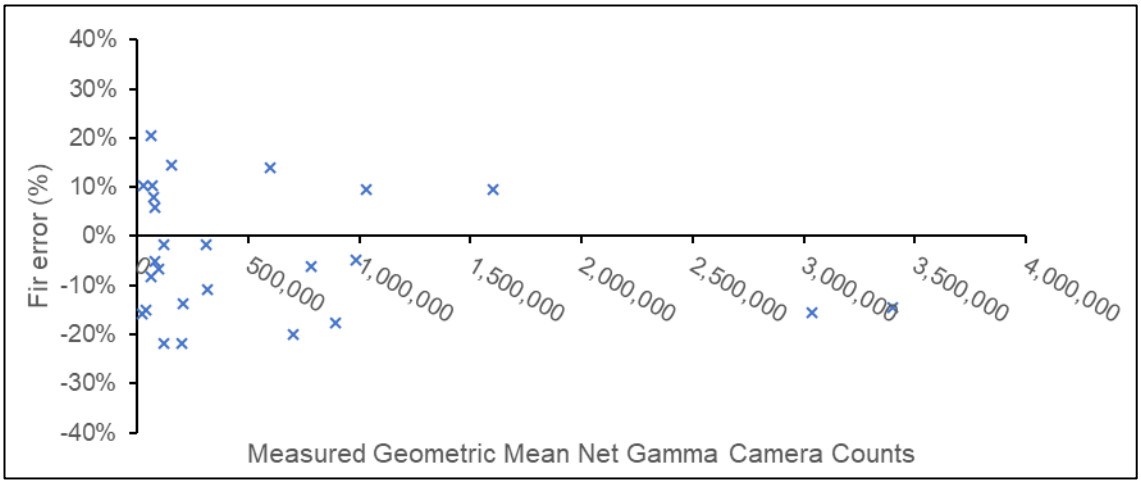

Figure 23. Plot of error in estimated Radhound net decay corrected count rate as a function of measured geometric mean net gamma camera counts. The Radhound counts were estimated using the measured gamma camera counts.

3.7.3. Discussion

Significant errors were seen in the estimation of Radhound whole body count rate from measured gamma camera counts. Therefore, based on the current work whole body gamma camera images cannot be used to provide whole body retention measurements for a single time point in conjunction with an external probe. Measurements with a probe that can be moved between rooms, or matched probes is instead suggested. If a separate probe is being used for outpatient measurements then measurements with this probe should also be taken at discharge to allow cross-calibration [57]. Performing gamma camera measurements only would remove the need for a cross-calibration between equipment in different areas, however this would likely result in less measurement time points and issues with deadtime correction at early time points.

The main reason for the errors seen with using gamma camera counts for a late whole body retention measurement is thought be due to the difference in scatter and photon acceptance angle for the different detectors. The arms of patients were not always fully within FOV, as seen within Figure 21. However tissues within arms typically do not actively accumulate the radiopharmaceutical and as such are unlikely to have had a significant impact, as the arm accounts for approximately 5% of a patient's body weight [116]. Therefore even in a worse case where the entire arms were excluded from the field of view and the activity was evenly distributed within the body, this would still account for less than 5% of the uptake within the patient.

Septal penetration artefacts were seen from areas of high uptake in gamma camera images, which do not affect the probe as it does not have septa. For example in one

patient a septal penetration artefact was seen in the anterior image (see Figure 21) resulting in anterior, posterior and geometric mean gamma camera counts of 822k, 434k and 596k respectively, with the Radhound net count rates calculated from the fit 22%, 3% and 14% higher than those measured. Further work could investigate the impact of septal penetration artefacts, for example through performing measurements of phantoms with different lesion to background activity ratios.

The calibration could be affected by patients going to the toilet between probe measurements and imaging, however at the imaging time points used this is unlikely to fully account for the large differences seen. For example, one audit patient scanned 2.8 days after administration needed to go to the toilet after the initial probe measurements were performed and a 4.7% decrease in measured probe counts was seen.

For the two patients with the highest gamma camera counts, underestimation of Radhound counts using the fit could be due to gamma camera deadtime, which was not corrected for. Therefore further work could investigate the use of deadtime correction or fast mode. For posterior imaging the table would introduce attenuation not seen with probe measurements, however as this would be the same across all patients this was not thought to be the reason for discrepancies seen.

3.8. Blood Sampling Calibration

4.1.1.Methods

EANM bone marrow dosimetry guidelines suggest that 2 ml heparinised blood samples in 1ml aliquots should prepared for each measurement time point, measured on a calibrated gamma counter and activity concentration calculated [21]. Therefore in order to implement dosimetry using blood samples, I-131 sensitivity calibration of the sample counter was required. This was performed in line with IPEM guidance [117].

The sensitivity was measured using 10 samples containing 1ml stock solution with known activity concentration. To determine the activity concentration of the stock solution, the liquid weight and activity within a standard vial was measured, 0.01ml was dispensed into a 1L volumetric flask using a syringe and the flask was made up to 1L using water. The activity in the vial was measured to be 4.43MBq using a Capintec calibrator (Mirion Technologies) with an I-131 measurement factor traceable to the National Physical Laboratory and an accuracy of 5% was assumed [118]. The vial liquid weight and syringe

dispensed weight were measured using a Kern ABJ-NM/ABS-N balance (Kern Ltd) with 0.001g precision. The stock solution was pipetted into 10 sample tubes using 1ml aliquots and the weights of the liquids were determined using the Kern balance.

The sample count rates were then measured using two automated gamma counters, the Wallac Wizard 1480 and Wizard2 2480 (Perkin Elmer) with NaI(Tl) crystals of height 80 mm and diameter 75 mm, with 1ml water background samples at the start and end of counting. The samples were counted for 1200s on the Wizard 1480 with the I-131 360 keV dynamic window (boundary 260 to 430 keV) and decay correction to sample start time. They were then counted 18 hours later for 3000s per sample on the Wizard2 2480 with a 360keV fixed window (boundary 260 to 430 keV). There was an 8 day delay in initial counting due to equipment failure, therefore the activity concentration was ~0.5kBq/ml during counting. The samples were reweighed prior to counting and the weight reduction was found to be less than 0.02% so the delay was not thought to have a significant impact on the results.

For each counter the measured counts per minute were recorded for each sample and this was background corrected, then decay corrected to reference time as appropriate. The activity in the samples at reference time was then calculated based on the stock reference activity concentration and measured sample weight. The sensitivity was then calculated as the ratio of sample corrected count rate and reference activity. The mean sensitivity for the samples was then calculated for each gamma counter.

4.1.2. Results

I-131 sensitivity for a 1ml sample was measured to be 432±22 cps/kBq for the Wallac Wizard 1480 counter and 425±21 cps/kBq for the Wizard2 2480 counter.

4.1.3. Discussion

I-131 1ml sample sensitivity for Wallac Wizard 1480 and Wizard2 2480 counters at RSCH has been measured and can be used to calculate the activity concentrations for 1ml patient blood samples. Daily stability QC with a long lived check source should be performed in accordance with guidance [117] to check for any changes in system performance. The sensitivity testing should be repeated if any change in performance is seen or if the energy windows or sample geometry are changed, the testing should also be performed periodically to confirm that the system performance has not changed for I-131.

4. Tumour Dosimetry Investigation

4.1. Introduction

Tumour dosimetry in molecular radiotherapy requires quantification of the radionuclide uptake within the tumour. In order to perform quantification of I-131 uptake within tumours using gamma camera imaging deadtime, sensitivity and partial volume effect calibrations should first be performed. The gamma camera I-131 calibrations were performed using common methods identified in the literature review given in Chapter 2.4, comparing different published methods where possible and are detailed in Chapters 4.3, 4.5 and 4.6. Measurements were performed on a GE Optima 640 SPECT/CT system (GE Healthcare), which had previously been found to require the use of the fast counting mode for I-131 patient dosimetry [53]. Therefore calibrations were performed using fast mode and the results were compared with normal mode measurements where possible. This was performed to help characterise the changes due to fast mode, as it is not well documented within literature.

For SPECT imaging the literature review in Chapter 2.4.8 identified that reconstruction parameters should be optimised for dosimetry purposes, based on the system and planned use. An investigation into the optimal SPECT reconstruction parameters for tumour mean dose calculation is given in Chapter 4.4.

The dose received from radionuclides within the body can be calculated using either dose S-factors, dose kernel convolution or Monte Carlo modelling. Due to lack of available CE marked specialist dosimetry software at RSCH, dose to patient target regions will be calculated using S-factors given in the widely available OLINDA/EXM 1.0 software [26]. This software gives S-factors for discrete sphere masses and Chapter 2.5 covers the determination of an equation which can be used to calculate the S-factors based on measured tumour volumes.

4.2. General Methodology

All gamma camera acquisitions were performed on the Optima 640 SPECT/CT system with a 9.5mm thick crystal. Unless otherwise specified, HEGP collimators were used with fast mode applied, a “photopeak” window of 364keV±10%, “lower” scatter window of 318keV±3% and “upper” scatter window 413keV±3%. I-131 fast mode and normal mode uniformity maps had previously been created and were tested periodically using 20Mcount intrinsic uniformity tests to ensure consistent uniformity. Other gamma

camera testing was also performed in line with national guidance [53], [59], [119]. SPECT acquisitions were performed with 120 views and 3° between views, body contouring and a 128x128 matrix, giving a 4.4mm pixel size. All CT acquisitions were performed with the clinical low dose protocol of 120kVp, 30mAs, 1.25 pitch, 512x512 matrix and 2.5mm slice thickness. SPECT image reconstruction was performed using Xeleris Volumetrix software (version 4.12, GE Healthcare). VOI outlining was performed using Mirada General Oncology Review (version 3.6, Mirada Medical Ltd).

The SPECT acquisition parameters chosen were those used for the MRTDosimetry project [101], with the exception that GE fast counting mode was investigated in addition to the normal counting, as suggested by Gregory *et al* 2019 [53], [101]. It is noted that 72 and 60 projections were acquired in the recent SEL-I-METRY and MEDIRAD trials respectively, to enable an increased scan times per projection for low count rate late time point imaging [53], [72]. However acquiring with 120 projections allows for improved sampling [56], [120] and could enable investigation of the impact of using 60 projections at a later date.

All activity measurements were made using Fidelis (Southern Scientific Ltd) or Capintec (Mirion Technologies) calibrators with I-131 measurement factors traceable to the National Physical Laboratory. Masses less than 80g were measured on a Kern ABJ-NM/ABS-N balance (Kern Ltd) with 0.001g precision and all other masses were measured using a Kern FKB 15KO.5A balance (Kern Ltd) with 0.5g precision.

4.3. Deadtime

4.3.1.Methods

Deadtime phantom acquisitions were performed by Jill Wevrett, Nick Bates, Rebecca Gregory and James Scuffham in accordance with the SELIMETRY trial protocol as part of the site set up for the trial [121]. A Jaszczak cylindrical phantom with a 21.6cm diameter was filled with water and an air bubble for mixing, then was placed on the patient couch between the detector heads as shown in Figure 24. 1g potassium iodide and 1g sodium thiosulphate was added to the phantom to reduce plating out of the I-131. Phantom activities covering the range of 20-2800MBq were investigated by adding increments of I-131 to the phantom. Acquisitions for each phantom activity were performed, terminating for each detector head on 100 kcts in the photopeak window. Fast and normal modes acquisition were performed on separate occasions, due to initial issues with fast mode

setup. Detector 1 upper scatter window fast mode images were disregarded as the window had been set up incorrectly.

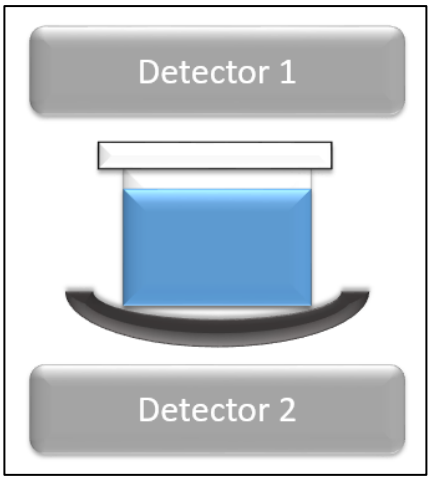

Figure 24. Experimental setup for deadtime acquisitions. 15cm diameter Jaszczak phantom on couch between detector heads, with heads positioned as close as possible to the phantom.

The activity in the phantom was determined from Capintec calibrator measurements of the vial activity before and after dispensing, the residual activity in syringe used for injection into the phantom and the previously calculated phantom activity. Therefore the errors in phantom activity estimation increased with increasing activity, however this method allowed for all acquisitions to be performed in a day.

TEW correction was performed on Head 2 images using an in-house Aladdin code on the GE Xeleris (GE Healthcare) in accordance with Equation 12, all negative pixels were set to zero and the total counts with no pixel rounding were recorded. The count rate in each of the images produced was determined from the total counts and acquisition duration.

The lowest activity used for the phantom acquisitions, A_{low}, (17.9MBq for fast mode, 18.4MBq for normal mode) was assumed to give negligible deadtime and the "true" count rate for each nth measurement, $R_{N,T}$, was calculated using Equation 25. A_N is the phantom activity for the Nth measurement and R_{low} is the observed count rate with activity A_{low}.

$$R_{N,T} = A_N \frac{R_{low}}{A_{low}} \qquad (25)$$

The deadtime factor, DF, was calculated for each image based on the observed count rate $\mathrm{R_{N,O}}$ and "true" count rate $\mathrm{R_{N,T}}$ using Equation 26 below.

$$\mathrm{DF} = \mathrm{R_{N,T}}/\mathrm{R_{N,O}} \qquad (26)$$

For the SEL-I-METRY and MEDIRAD trials the "true" count rate was calculated from linear extrapolation of five count rate measurements with activities below 100MBq, assuming no deadtime [53], [72]. However, during the analysis for this work decreased count rates per unit activity already appeared to be seen for those activities, particularly with normal mode (see Figure 26). Therefore it was decided to instead use the lowest activity measurement point.

The deadtime using paralysable and non-paralysable models was calculated using Equations 4 and 5 respectively, using OriginPro simple fit tool (version 2020b, OriginLab Corporation). For normal mode deviations from the non-paralysable fit could be seen with activities greater than 1200MBq, so this data was not used for determining deadtime for this fit.

The percentage uncertainty in measured count rate $u(R_{N,O})/\,R_{N,O}$ was assumed to be due to Poisson statistics and so the inverse square root of the measured counts was used ($1/\sqrt{C_{N,O}}$). The percentage uncertainty in the activity measurements, $u(A_{low})/A_{low}$, was assumed to be 1%, based on instrument repeatability [118]. The uncertainty in the deadtime factor, $u(DF_N)$ was calculated using Equation 27.

$$\left[\frac{u(DF_N)}{DF_N}\right]^2 = \left[\frac{u(R_{N,O})}{R_{N,O}}\right]^2 + \left[\frac{u(A_{low})}{A_{low}}\right]^2 + \left[\frac{u(R_{low})}{R_{low}}\right]^2 \qquad (27)$$

4.3.2. Results

The observed count rates measured for the photopeak, lower window, upper window and TEW datasets as a function of phantom activity are given in Figure 25 for fast and normal modes. The deadtime factors as a function of phantom activity for Head 2 are given in Figure 26 for fast and normal modes. For Head 2 fast mode the observed count rates with the lowest phantom activity of 17.9MBq were 421cps, 75cps, 51cps, 274cps for the photopeak, lower window, upper window and TEW images respectively. For Head 2 normal mode the observed count rates with the lowest phantom activity of 18.4MBq were 487cps, 85cps, 62cps, 307cps for the photopeak, lower window, upper window and TEW images respectively.

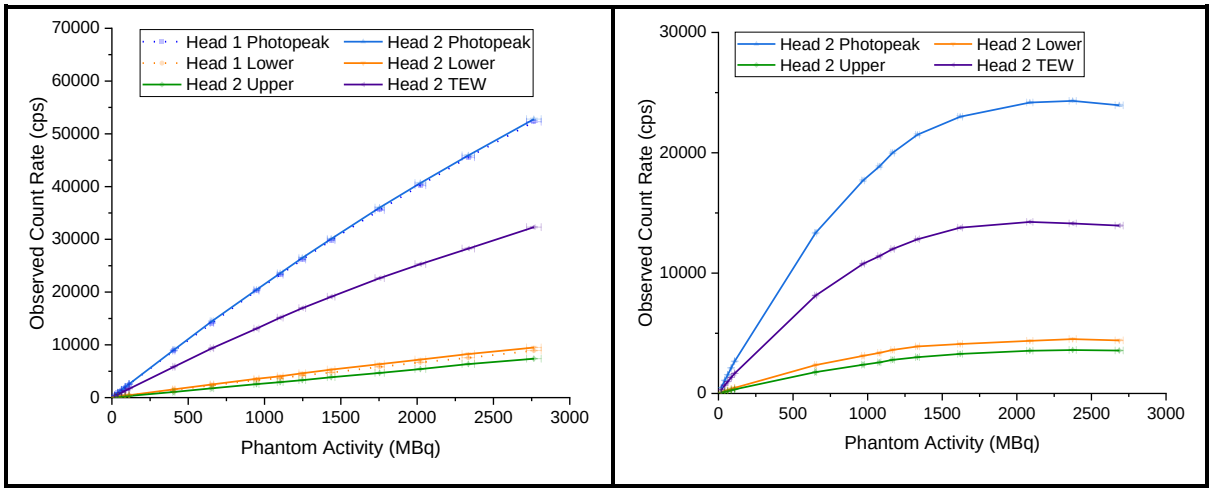

Figure 25 Observed count rate as a function of Jaszczak phantom activity for photopeak, upper scatter, lower scatter and TEW corrected images. Given for fast mode (left) and normal mode (right).

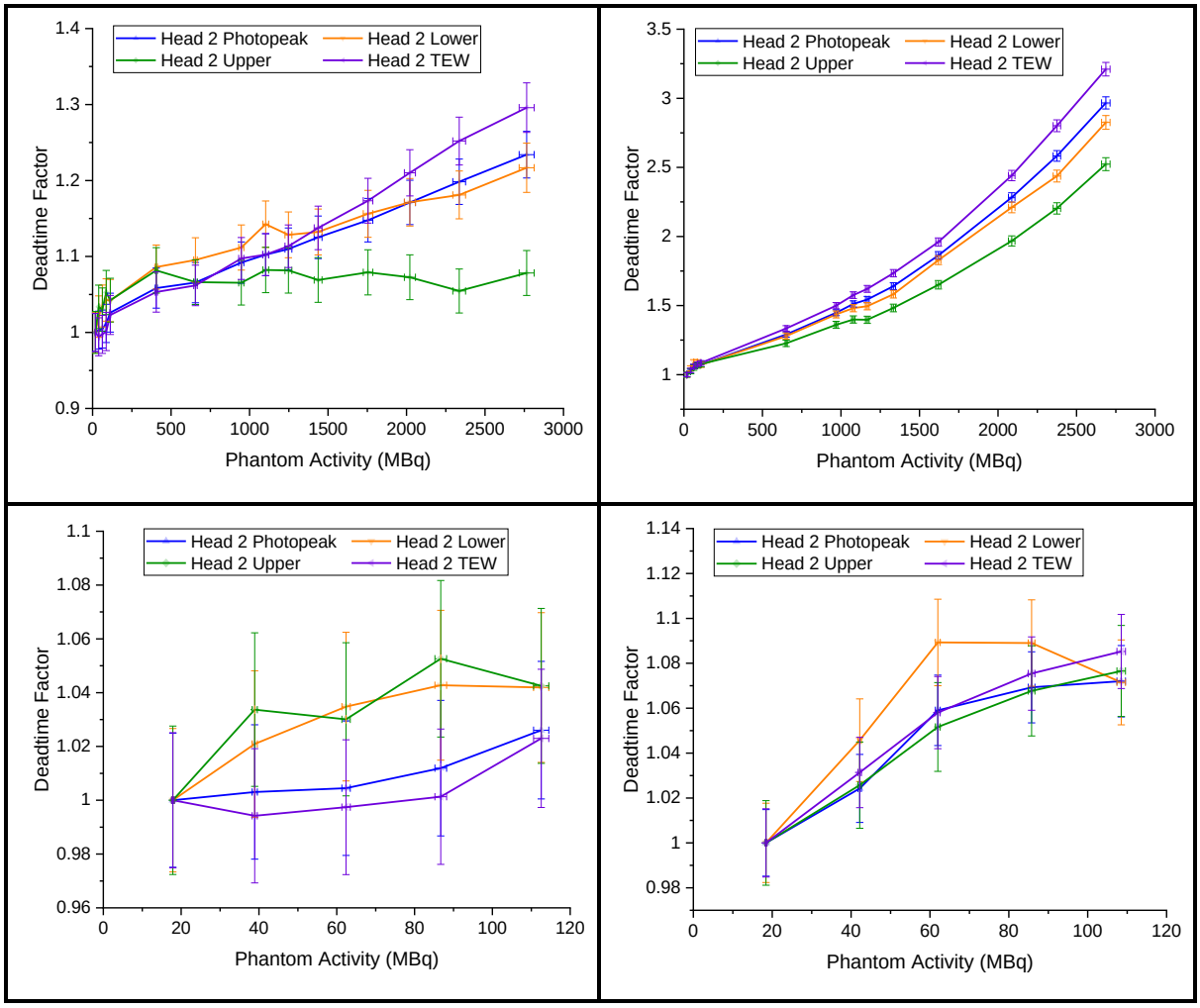

Figure 26 Deadtime factor as a function of Jaszczak phantom activity for photopeak, upper scatter, lower scatter and TEW corrected images. Given for fast mode (left) and normal mode (right). Shown for full range of phantom activities (top) and first five measurements (bottom).

The fast and normal mode calculated deadtime is given in Table 4 for the photopeak, lower, upper and TEW images using paralysable and non-paralysable fits, along with the sensitivity factor calculated from the low deadtime measurement. The errors in the fits are given in the Figure 27 for fast mode and Figure 28 for normal mode.

Table 4 Calculated deadtime parameters for Head 2 using paralysable and non-paralysable fits. Deadtime is given for each energy window, together with the error in the fits for fast and normal modes. Sensitivity factor calculated from the low deadtime measurement.

Mode	Window	Baseline Sensitivity (cps/MBq)	Deadtime (µs)		Fit Error	
			Non-paralysable	Paralysable	Non-paralysable	Paralysable
Fast	Photopeak	23.02	3.62±0.03	3.30±0.03	-0.2%-2.3%	-0.5%-2.6%
	Lower	4.18	19.8±0.6	18.1±0.6	-1.2%-5.0%	-1.2%-5.3%
	Upper	2.87	11.1±1.0	10.7±0.9	-1.8%-6.8%	-2.0%-6.8%
	TEW	15.31	6.91±0.08	6.20±0.04	-1.6%-1.1%	-1.2%-1.3%
Normal	Photopeak	26.44	17.6±0.1	14.9±0.1	-1.0%-31.8%	-3.0%-3.4%
	Lower	4.63	94.3±0.1	81.2±0.7	-1.0%-30.0%	-4.2%-6.4%
	Upper	3.35	106.8±1.6	98.2±1.3	-1.2%-29.2%	-4.8%-4.4%
	TEW	16.66	31.6±0.2	25.7±0.1	-1.0%-32.9%	-2.1%-3.7%

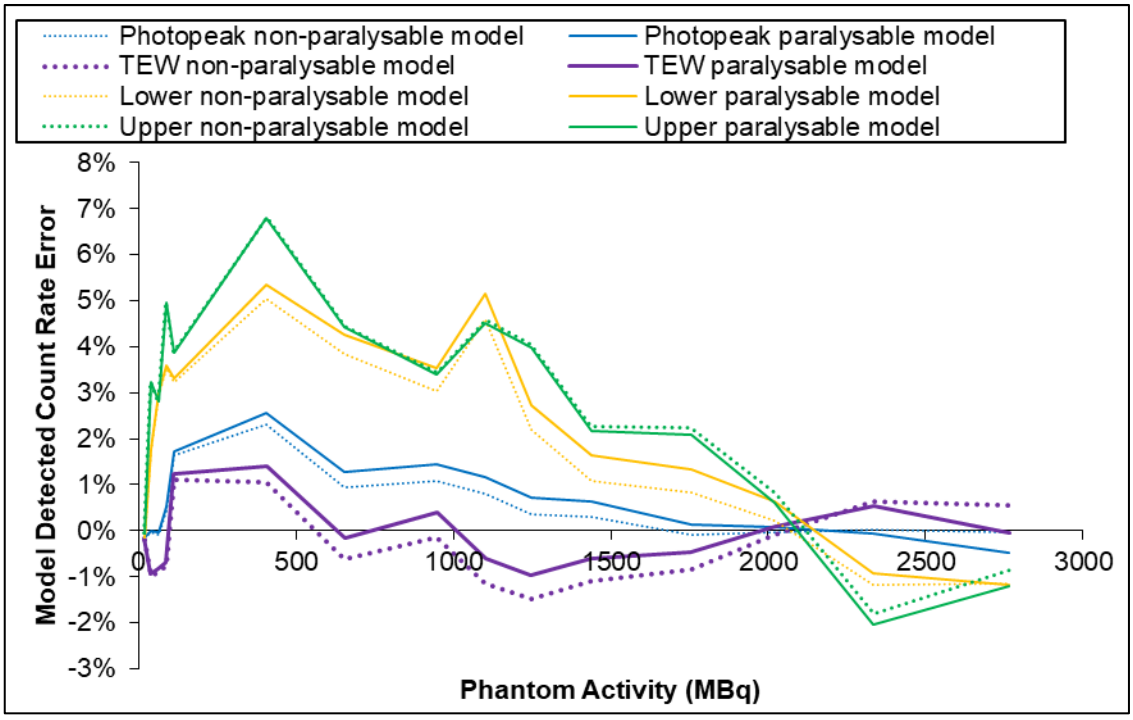

Figure 27 Error between measured and fit count rate for fast mode photopeak, upper scatter, lower scatter and TEW corrected Jaszczak phantom images.

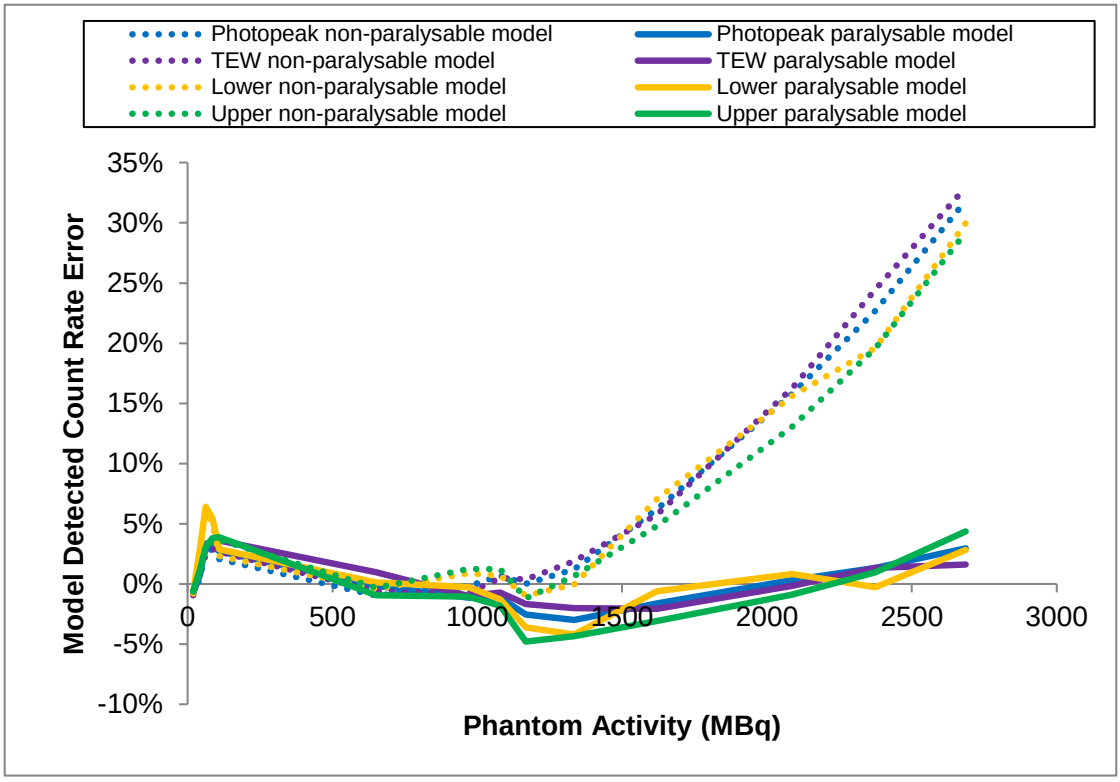

Figure 28 Error between measured and fit count rate for normal mode photopeak, upper scatter, lower scatter and TEW corrected Jaszczak phantom images.

4.3.3. Discussion

From Figure 25 it can be seen a turnover point was seen for normal mode at around 1.6GBq but that turn over points or plateaus in the count rates were not observed using the phantom activities of up to 2.7GBq in fast mode. Therefore fast mode should be used for I-131 dosimetry imaging as high activities are present, which agrees with the SEL-I-METRY trial findings [53]. While it is expected that the paralysable model would give the best approximation of the system with fast mode [65], [77] and this has been seen with normal mode, to prove this higher count rates would be required. Sanderson et al 2019 performed imaging of up to 12GBq I-131 with a GE Discovery 670 gamma camera and a plateau or turnover point was still not seen [122]. It is noted that Sanderson et al observed extreme non-uniformities within the images at increased count rates. However, following setup corrections by GE this was not seen in this work, with the exception of the Detector 1 upper scatter window, which was subsequently corrected. Therefore future work could investigate imaging with higher count rates to confirm the most appropriate model to use for the GE Optima in fast mode.

Figure 28 demonstrates that up to around 1100MBq, I-131 paralysable and non-paralysable fits gave good agreement with measured data for normal mode, however

above this greater deviations are seen. However from Figure 27 it can be seen that for fast mode both non-paralysable and paralysable models gave good agreement with the available photopeak and TEW data using fast mode, with low fit errors. As the non-paralysable model does not require iterative methods to calculate the true count rate from the observed count rates, this model will be used for the GE Optima in fast mode for activities under 2.7GBq.

Using the calculated deadtime for the TEW images, the non-paralysable and paralysable models give greater than 1% difference for activities above 3GBq. This indicates that the non-paralysable model should not be used to image activities greater than 3GBq to reduce errors. Patients are frequently administered with activities up to 5.5GBq, which would give a 6% difference between paralysable and non-paralysable models. Therefore there will need to be a delay between administration and imaging so the administered activity is not within a single field of view. Whole body half-lives of 12.6±1.8 h have been reported [111] and similar results were seen from the whole body retention measurements in this work. Therefore if 5500MBq was administered an 11 to 15 hour delay before imaging would be required for the whole body activity to be less than 3GBq. However, a stomach biological half-life of 0.54±0.32h was reported by Huang et al 2020 for from I-131 post therapy imaging in 9 thyroid cancer patients [111]. From the patient data given, it can be calculated that at 2h post administration a maximum of 16% of uptake was present in the stomach, 14% in the thyroid, 3% in the bladder and 70% within the blood. Therefore assuming a worst case scenario where the stomach, a thyroid tumour with 14% uptake and a quarter of the blood volume were in a single FOV, 47% of the administered activity would be seen. So for a 2h uptake period and a 5500MBq administered I-131 activity, less than 2.6GBq would be expected to be seen within a single FOV. Therefore after 2h post administration the deadtime should be appropriately modelled by the non-paralysable calibration, however the count rates should be checked for patient images.

The deadtime was calculated to be 3.62±0.03µs for photopeak imaging and 6.91±0.08µs for TEW imaging. In comparison, the fast mode photopeak non-paralysable deadtime for the GE Optima was reported to be 3.15±0.03µs by Gregory *et al*. 2019 [53], which is not within experimental uncertainties. However the lower deadtime calculated by Gregory *et al* is likely due to their different true count rate calculation, which could have been affected by deadtime. Using multiple measurements has the advantage of reducing experimental error, therefore to enable the true count rate to be calculated from multiple

measurements it is suggested that more measurements with low activities could be performed.

For fast mode the lower and upper windows gave poorer agreement with the models, with higher fit errors, however this was not seen so significantly with normal mode. From Figure 26 it can be seen that the fast mode deadtime factor for the lower and upper scatter window data initially increased faster with phantom activity than the photopeak window and TEW data. At around 406MBq the lower window fast mode deadtime factor appeared to stabilise, with the upper window deadtime factor increasing at a slower rate than previously. However for normal mode the deadtime factor for all energy windows increased smoothly with increasing phantom activity.

In literature, Guy et al 2002, Deplon et al 2002 and Schipper et all 2012 all reported a decrease in deadtime factor with I-131 activity for lower and upper scatter windows with an ADAC Vertex system with Epic heads, DST-Xli camera with fast electronic acquisition card and Siemens Symbia TruePoint respectively [71], [76], [77]. This effect was believed to be due to pulse pileup, therefore it is likely that the GE fast mode system deals with high count rates in a different way to the systems previously reported and so may not experience pulse pileup in a similar way. Further investigation is required into the energy window spectra dependence on activity with GE fast mode, as well as if the conventional pulse pileup artefacts as depicted in Figure 9 are seen with GE fast mode.

The reason for the changing deadtime factor-activity profiles for the scatter windows with GE fast mode is unclear and could be related to a change in the handling of counts from different energies. This is not thought to be significant for this work as the photopeak and TEW images appear to be fairly well characterised with non-paralysable models, however it is an area that requires further investigation.

4.4. SPECT Reconstruction Optimisation

4.4.1. Methods

Four 3D printed cylinders with lengths of 38mm and diameters of 7.5, 15.0, 30.0 and 60.0mm filled with I-131 were positioned within a water filled 21.6cm torso shaped phantom as shown in Figure 29. The cylinders were filled by Jill Wevrett in accordance with the MRTDosimetry protocol [101] two days prior to scanning. A 160ml stock solution containing 0.1 mol sodium hydroxide and 10 μg g^{-1} stable iodine was used to reduce

plating out of the I-131. The activity concentration in the cylinders at the time of scanning was 147kBq/ml. SPECT/CT acquisitions were performed in fast mode with a 128x128 matrix, 120 views and 15s/view.

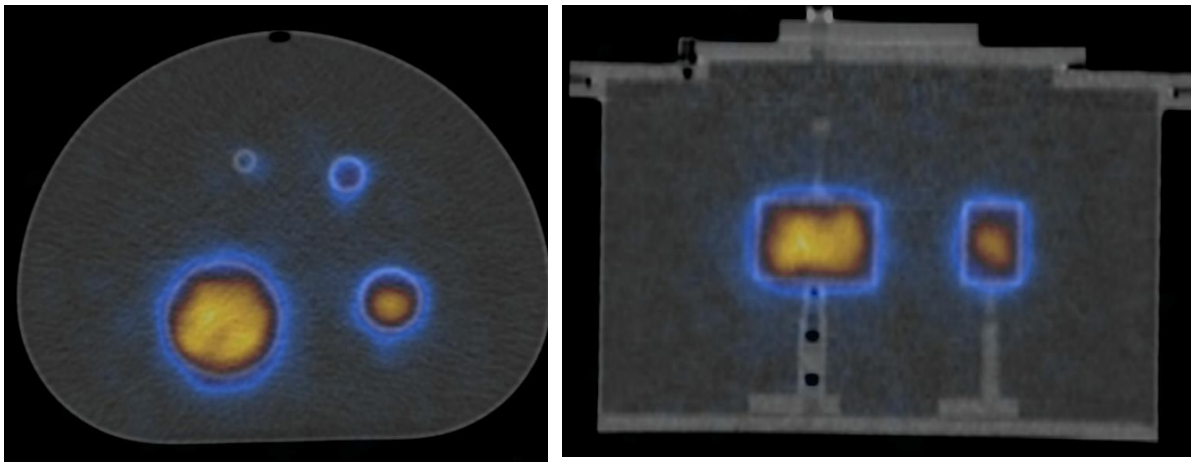

Figure 29. I-131 filled cylinder sources positioned within water filled torso phantom.

Within the GE Volumetrix software at RSCH, the SPECT reconstruction corrections available were CT attenuation correction (AC), TEW scatter correction (SC) and Gaussian CDR modelling (RR). To determine the optimum SPECT reconstruction parameters, the number of iterations and subsets were varied for AC with TEW correction and AC with TEW and RR correction using GE Volumetrix software with no smoothing filter. The maximum number of iterations allowed by the system was 100. The optimum number of subsets with 100 iterations was first determined for each reconstruction type, once this was found the number of iterations was varied for each reconstruction type. To assess the optimal reconstruction parameters, the reconstructed images were loaded into Amide [123] and VOI analysis performed. The CT was manually registered with the SPECT images based on the clinical reconstruction (2 iterations, 8 subsets and Butterworth filter with critical frequency of 0.48 and power of 10) and cylindrical VOIs were drawn based on the CT. The mean counts and standard deviation for each of cylinders were determined for each reconstruction. To enable graphical display of the mean counts for the different cylinders for different iterations, the "normalised" mean for cylinder diameter *d*, iteration *i* and subset *s*, were calculated using the Equations 28 and 29 given below.

$$Normalised\ mean_{s=2} = \frac{mean_{d,i,s}}{mean_{d,i,s=2}} \qquad (28)$$

$$Normalised\ mean_{i=100} = \frac{mean_{d,i,s}}{mean_{d,i=100,s}} \qquad (29)$$

4.4.2. Results

The number of subsets used resulted in different mean counts at the maximum of 100 iterations. A graph of mean counts in each of the cylinders as a function of subsets is given for each of the cylinders and reconstruction types in Figure 30. Approximately 80-90kcounts were seen in the slices containing the cylinders for ACSC reconstruction and around 4 times that seen with ACSCRR due to the projections multiplication factor of 4.

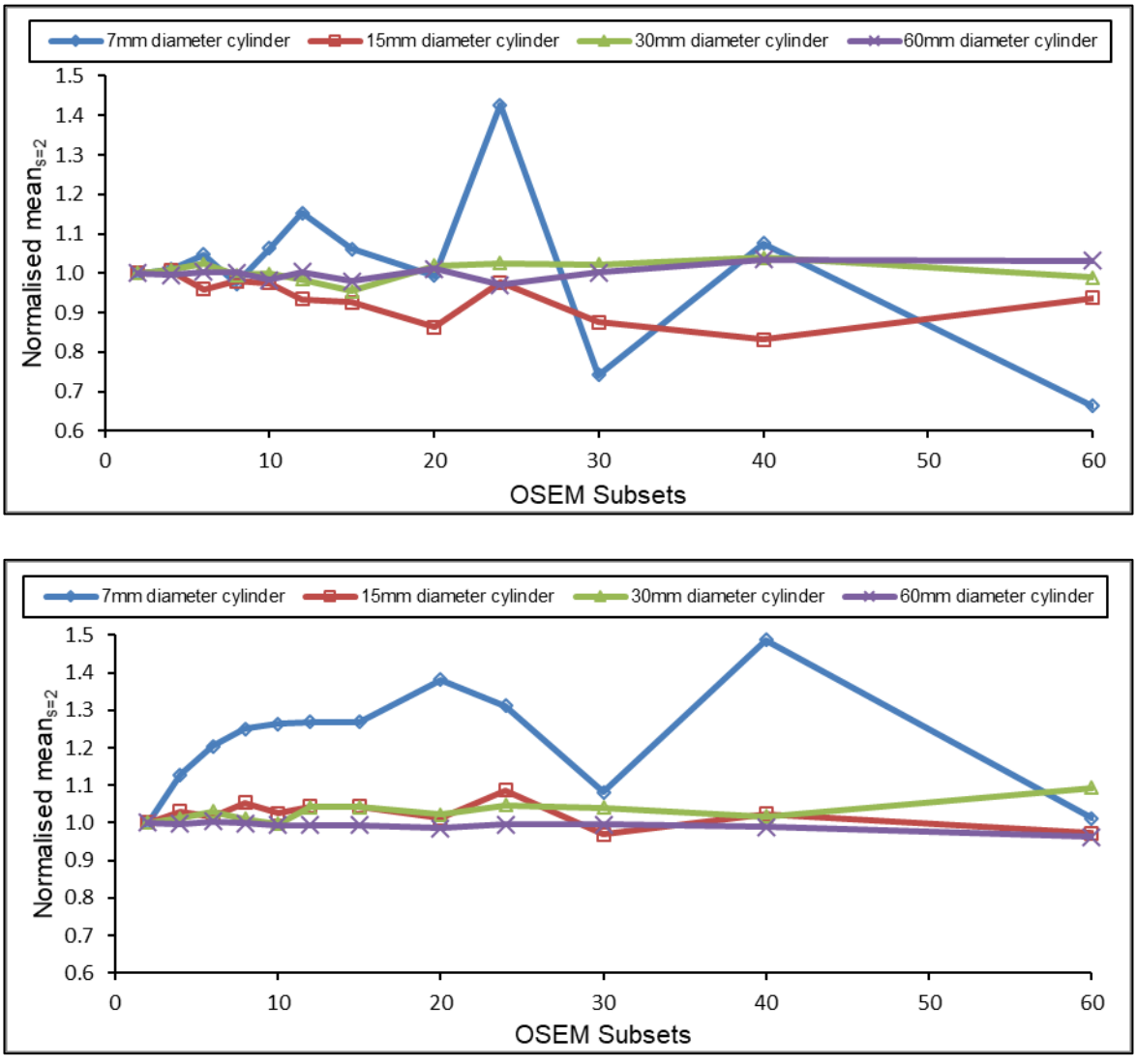

Figure 30. A graph of mean counts in the 7.5, 15.0, 30.0 and 60.0mm diameter cylinders as a function of subsets with 100 OSEM iterations. Given for AC + TEW (top) and AC + TEW +RR (bottom). Normalised to the mean counts for 2 subsets.

2 to 10 OSEM subsets and 10 to 15 OSEM subsets were found to give similar variation in mean counts for the cylinders for TEW and TEW+RR respectively. Therefore the optimum number of subsets was taken to be 10 for TEW and 15 for TEW+RR, to allow for faster convergence.

The optimum number of iterations with the previously found optimum number of subsets was investigated for TEW and TEW+RR, with plots of normalised mean cylinder counts

and standard deviation in cylinder counts as a function of iterations given for each of the cylinders and reconstruction types in Figure 31 and Figure 32 respectively.

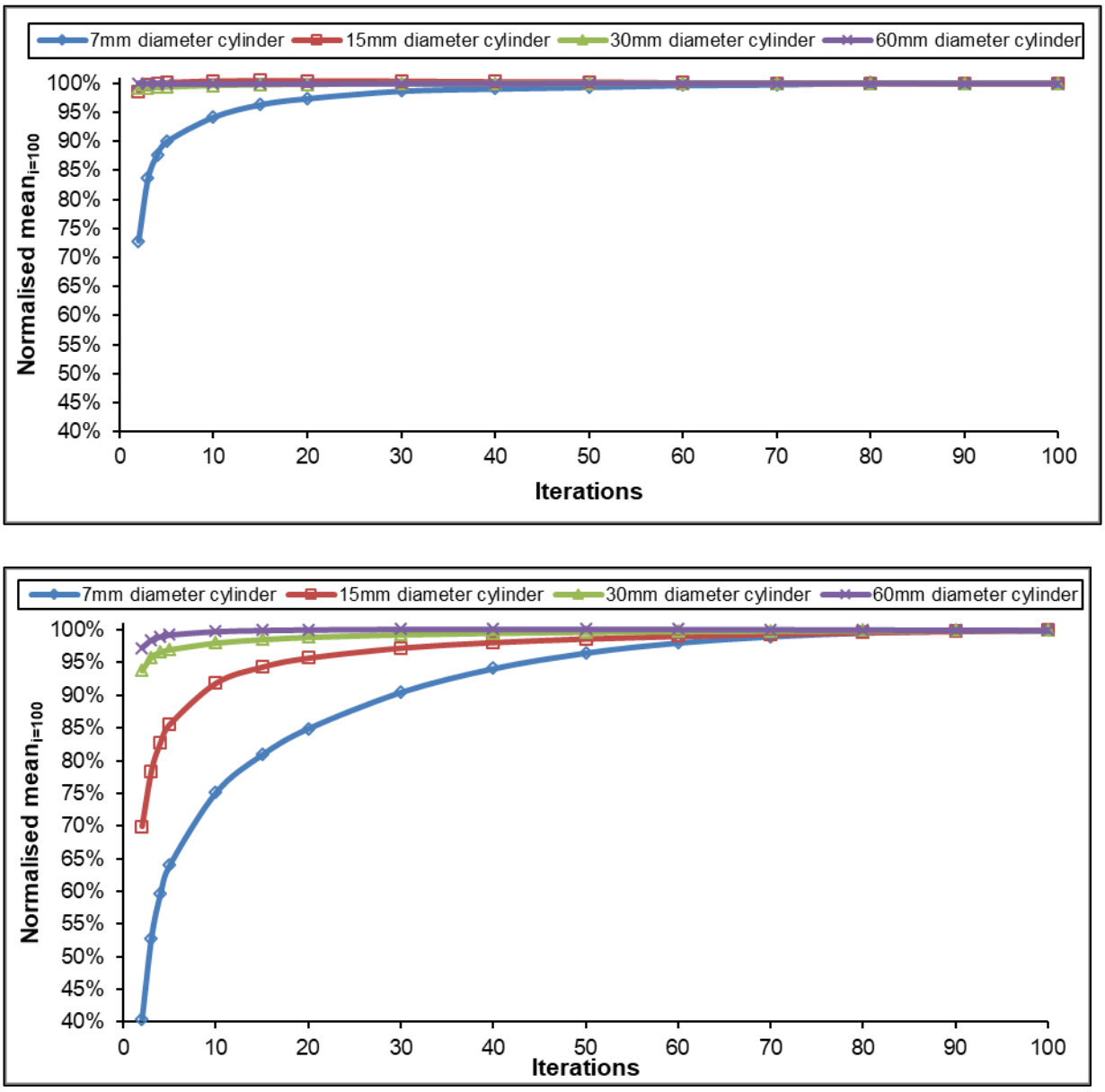

Figure 31. A graph of mean counts in the 7.5, 15.0, 30.0 and 60.0mm diameter cylinders as a function of iterations with 10 OSEM subsets. Given for AC + TEW (top) and AC + TEW +RR (bottom). Normalised to the mean counts for 100 iterations.

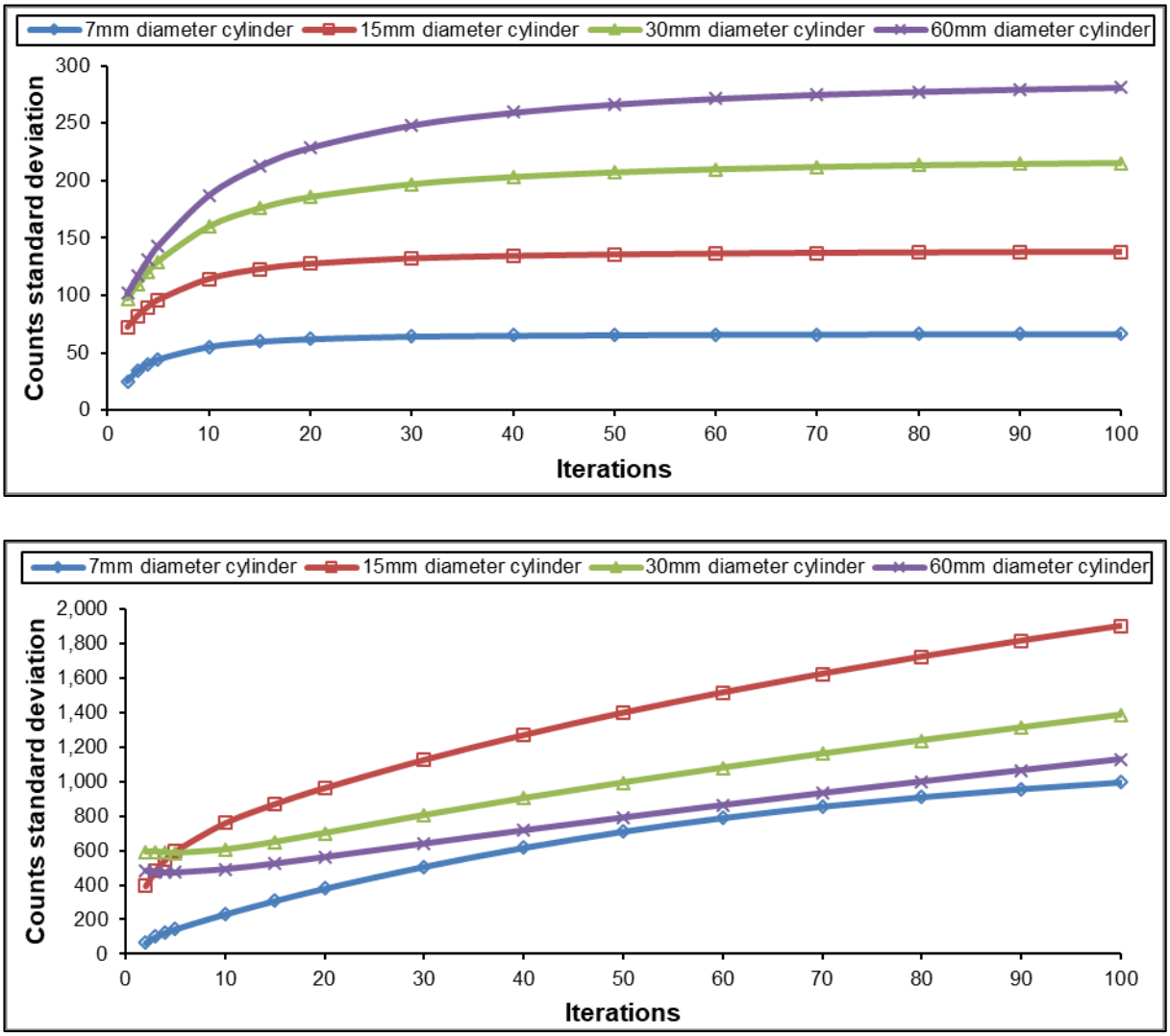

Figure 32. A graph of the standard deviation in counts for the 7.5, 15.0, 30.0 and 60.0mm diameter cylinders as a function of iterations. Given for AC + TEW with 10 OSEM subsets (top) and AC + TEW +RR with 15 OSEM subsets (bottom).

To enable visual assessment of the impact of the different reconstructions, a central transaxial slice through the cylinders is given in Figure 33 below.

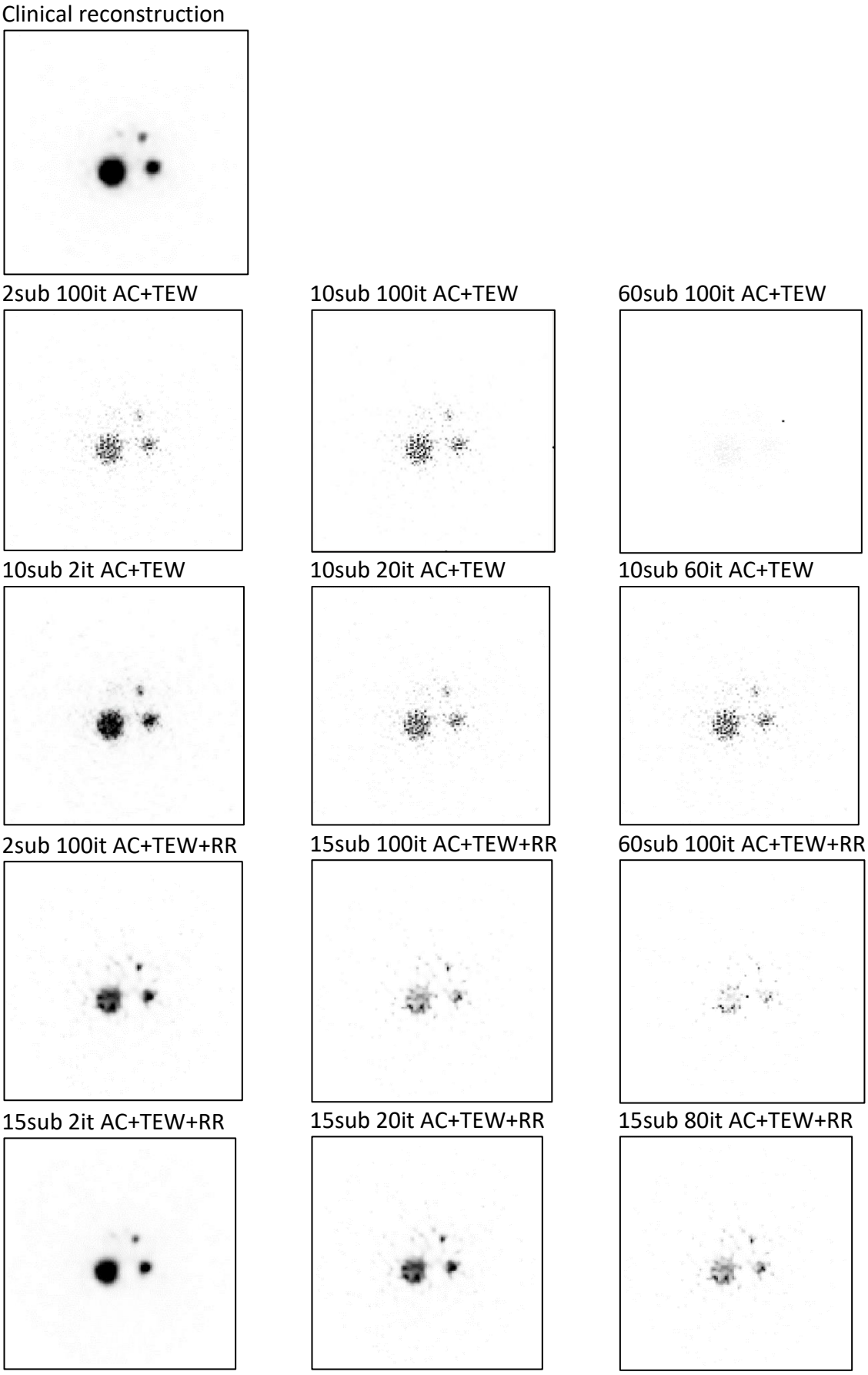

Figure 33. Central slice through cylinders with varying reconstruction parameters. A 60% window threshold was used for all images.

4.4.3. Discussion

For the ACSC 100 iterations data, from Figure 30 it can be seen that 2 to 10 OSEM subsets were found to give similar mean counts for the cylinders, with increased variation seen in the mean values for a greater number of subsets. From Figure 33 it can be seen that with larger numbers of subsets e.g. 60, artefacts were introduced into the images. This is likely due to the small number of projections used for each subset introducing noise artefacts into the images [124]. Therefore, the optimum number of subsets for ACSC reconstruction was taken to be 10, to allow for faster convergence while avoiding artefacts seen with high number of subsets. This gave 12 projections for each subset, well within the MIRD pamphlet 23 recommendation of 4 [56].

For the ACSCRR 100 iterations data, from Figure 30 it can be seen that the mean counts in the smallest cylinder increased with increasing subsets, stabilising at 10 to 15 subsets, then fluctuating for larger subsets. This indicates that convergence was not reached until 10 subsets. This agrees with previous literature which suggests an increased number of reconstruction updates are needed for RR [125]. Therefore the optimum number of subsets was taken to be 15 to allow for faster convergence, while avoiding artefacts seen with high number of subsets. This was also within the MIRD recommendations, with 8 projections per subset.

When increasing the number of iterations, from Figure 31 it can be seen that the mean counts converged, with smaller structures and RR requiring more iterations, as expected [29], [102], [106]. From Figure 32 and Figure 33, increasing the number of iterations was also found to increase the noise (standard deviation) within the images, with the standard deviation converging for high numbers of ACSC iterations and continuing to increase with ACSCRR. From Figure 33 artefactual substructures within the cylinders were noted with higher ACSCRR iterations, which were not seen with ACSC and has been noted previously [103], [105]. To reduce reconstruction time and noise artefacts within the ACSCRR images, the optimal number of iterations was taken to be the point at which 99.5% of convergence was reached. While a 95% convergence level is recommended in MIRD 26 [22], this threshold was picked to account for the potentially substantially lower counts that may be present for late time point imaging in patients. Therefore the optimum reconstruction parameters for organ level dosimetry were found to be 10 subsets and 60 iterations for ACSC and 15 subsets and 80 iterations for ACSCRR. Due to the artefacts seen with the ACSCRR reconstructions it was decided that the ACSC optimal reconstruction should be used for dosimetry purposes.

It should be noted that images with higher number of iterations and subsets appeared very noisy visually, with the smallest cylinder being almost impossible to visualise apart from with low numbers of updates. The smoothing in the clinical reconstruction also aided in visualisation (see Figure 33). Therefore for outlining of organs that cannot be determined from the CT alone, a reconstruction with a low number of updates and smoothing will also be required.

Other authors have also found that the number of reconstruction updates depends on the noise within the image and size of area of uptake, with smaller and noisier objects requiring more iterations for convergence [29], [102], [105]. This work investigated a range of object sizes, with a high convergence threshold and so it is unlikely that the optimal reconstruction parameters chosen would lead to errors in quantification. However, it is possible that less reconstruction updates could be required in clinical imaging, leading to reduced reconstruction time. Therefore future work could investigate using repeat acquisitions with different noise levels to determine the impact of image noise. Investigation into tailoring the number of updates based on the area of interest could also be performed using patient images. Due to the large amount of noise within the optimal reconstructions found, they are only applicable for organ level dosimetry; if voxel level dosimetry was to be performed further optimisation would be required.

4.5. SPECT Sensitivity

4.5.1.Methods

SPECT sensitivity phantom filling and normal mode acquisitions were performed by Jill Wevrett and James Scuffham in accordance with the MRTDosimetry protocol as part of the work for the project [126]. A Jaszczak cylindrical phantom with a 21.6cm internal diameter and 18.6cm internal length was filled sodium hydroxide (0.1 mol dm^{-3}), inactive iodine (10 µg g^{-1}) and ~39MBq I-131 at time of scanning. The phantom was weighed before and after filling, giving a volume of 6787.5±05 ml, assuming unit density. The activity in the phantom at the time of scanning, $A_{phantom}(T_{ref})$, was calculated using Equation 30, in accordance with the MRTDosimetry protocol [127].

$$A_{phantom}(T_{ref}) = \left(A_0 e^{-\lambda(t_{ref}-t_0)} - A_1 e^{-\lambda(t_{ref}-t_1)}\right)\left(1 - \frac{A_3 e^{-\lambda(t_{ref}-t_3)}}{A_2 e^{-\lambda(t_{ref}-t_2)}}\right) \qquad (30)$$

Where A_0 and A_1 are the activities in a 10R Schott vial with a standard volume of 4ml before and after drawing up at measurement times of t_0 and t_1 respectively; A_2 and A_3

are the syringe activities before and after injection into the phantom with a consistent volume at measurement times t_2 and t_3 respectively. Activity measurements were performed with a Fidelis radionuclide calibrator and the uncertainty in each activity measurement was taken to be 2% [128].

The phantom was positioned at the centre of the SPECT FOV and SPECT/CT acquisitions were performed in fast and normal mode with 60s/view. The uncertainty in the acquisition duration was taken to be 1s.

The TEW correction followed by non-paralysable deadtime correction was performed on the SPECT projections, using in house Aladdin software on the GE Xeleris developed for this work. The experimentally determined deadtimes of 6.9μs and 31.6 μs for fast and normal modes respectively were used for this correction (see Chapter 4.3). For each projection the software performed TEW correction with no pixel rounding, the TEW corrected total count rate for the projection was calculated and then non-paralysable deadtime correction was applied to each pixel within the projection. For fast mode the deadtime factor was low, however for normal mode a deadtime factor of around 1.02 was seen. The TEW and deadtime corrected projections were then reconstructed with GE Volumetrix software with no smoothing filter and CT attenuation correction using OSEM with the optimal 60 iterations and 10 subsets and no filter (see Chapter 4.4).

The fast and normal mode CT and SPECT images were loaded into Mirada General Oncology Review software and co-registered using automatic rigid registration. To investigate the use of the MRTDosimetry sensitivity calculation method [126], a VOI with 130% of the phantom radius and 120% of length was outlined manually using the fast mode CT image and then copied over to the normal mode images (See Figure 34 for VOI placement). To investigate the difference with the 131I-mIBG EANM dosimetry guidelines method a 75% of phantom size VOI [16] was also drawn and can be seen in Figure 34. To investigate the difference when the total counts were used, a VOI covering the whole FOV was used. The sensitivity Q, was calculated from the total counts within the VOI, C_{Total}, total effective acquisition duration T_{acq} and phantom activity within the VOI at time of scanning $A_{phantom}$, in accordance with Equation 31. For the MRTDosimetry and total counts methods $A_{phantom}$ was taken to be the total decay corrected injected activity, however for the EANM mIBG dosimetry methods $A_{phantom}$ was calculated by multiplying the phantom activity concentration by the VOI volume. The total effective acquisition

duration was calculated as the product of the number of projections and acquisition time per projection, matching the acquisition time given in the DICOM header.

$$Q = \frac{C_{Total}}{A_{phantom}\, T_{acq}} \qquad (31)$$

Due to need for co-registration between the fast and normal mode acquisitions and SPECT pixel size, while the VOIs were directly copied over from fast to normal mode the volumes were slightly different. The uncertainty in the VOI counts was taken to be due to Poisson noise.

To investigate the difference between the different methods, all transverse slices were summed and a 10 pixel thick horizontal line profile across the centre of the phantom was produced using the GE Xeleris software. Due to noise with the high number of iterations used for the optimal dosimetry acquisition, the analysis was also performed using the clinical reconstruction.

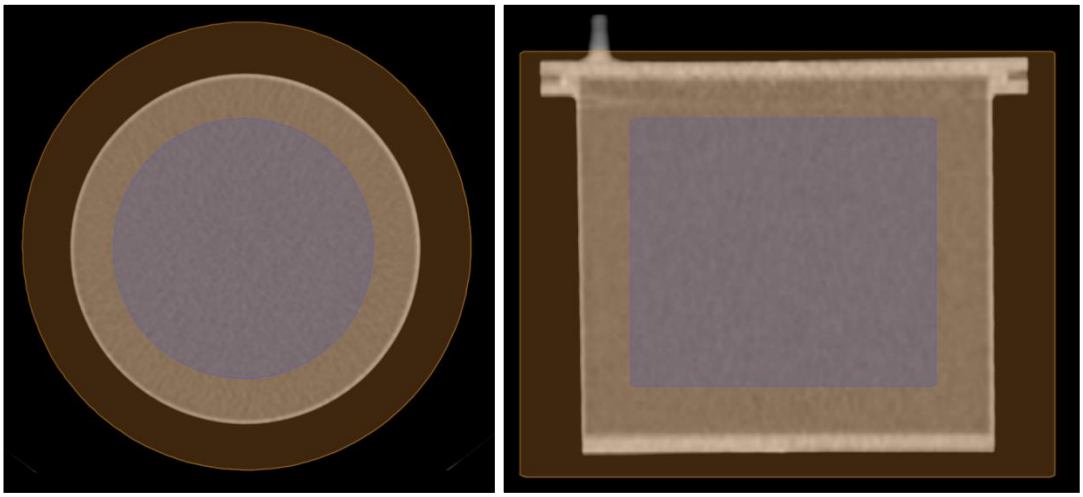

Figure 34. VOIs used for sensitivity analysis on CT image transverse (left) and coronal (right) central slices. The VOI using the MRTDosimetry Method is shown in orange and the small VOI using the EANM mIBG dosimetry method is shown in blue.

4.5.2.Results

The calculated sensitivities using the methods investigated are given in Table 5 and a profile across the centre of the Jaszczak phantom for summed transverse slices is given in Figure 35.

Table 5. Sensitivity calculated for I131 filled Jaszczak phantom imaged on GE Optima. Given for both fast and normal modes, with TEW and non-paralysable deadtime correction followed by OSEM reconstruction with 60 iterations 10 subsets and no filter.

Method		Mode	Sensitivity	
			cps/MBq	% difference
MRTDosimetry	130% of phantom radius, 120% of phantom length	Fast	22.3±0.9	6.3%
		Normal	23.7±0.9	
EANM mIBG dosimetry	75% of phantom size	Fast	21.7±0.9	9.1%
		Normal	23.7±0.9	
Total Counts		Fast	25.4±1.0	6.0%
		Normal	26.9±1.1	

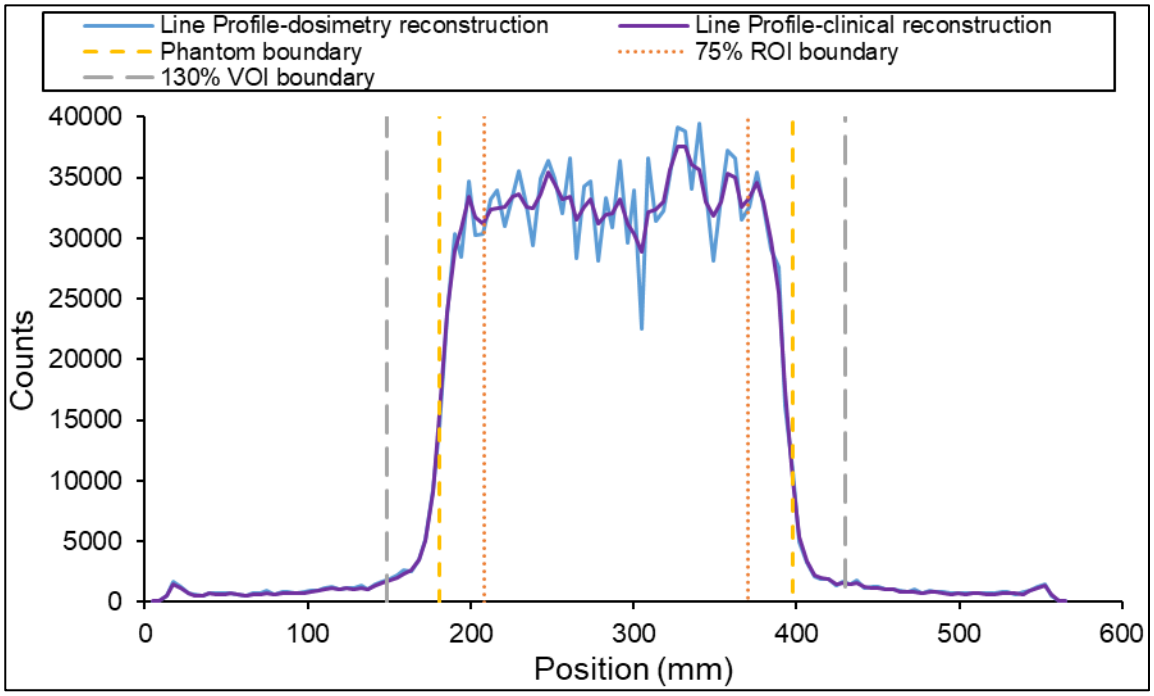

Figure 35. 10 pixel thick transverse fast mode SPECT slice line profiles across the centre of a Jaszczak phantom uniformly filled with I-131.

4.5.3.Discussion

EANM I-131 mIBG dosimetry method gave a lower sensitivity compared to the MRTDosimetry method (2.8% lower for "fast" mode and 0.1% lower for normal mode). However, the results lie within the uncertainty of the measurements, which suggests both VOI methods give similar results. The slightly higher sensitivity measured with the MRTDosimetry method may be due to the inclusion of additional scattered counts outside of the phantom field of view or because spill in and out of counts has not equalised for the 75% ROI. A 10 pixel thick horizontal line profile across the centre of the phantom transverse composite fast mode image appears to suggest that the spill in and

out should be balanced at the 75% ROI point but the 130% VOI might be including additional scatter. There are also additional counts outside of the 130% MRTDosimetry VOI boundary, meaning that it may be sensitive to VOI positioning. Further work could be performed to investigate the VOI position by performing multiple acquisitions as well as repeatedly drawing a VOI or perturbing a VOI to determine the potential positional error.

Using the total counts within the image resulted in substantially increased calculated sensitivity (14% higher than the MRTDosimetry method). This may be due to the inclusion of additional counts from scatter, septal penetration and background. GE recommend measuring sensitivity in accordance with the NEMA planar sensitivity method [73]. This involves a disc source positioned 10cm from each of the detector heads, using planar images acquired with 4 million counts in the photopeak and calculating the sensitivity based on the total counts [73]. Previous work at RSCH found the TEW corrected sensitivity using this method in normal mode was 26.9 cps/MBq using 10MBq I-131 [129], which agrees with the results seen when using the total counts SPECT method. This also agrees with findings by Zhao *et al* that SPECT and planar sensitivity give good agreement when total counts are used [130]. For clinical dosimetry VOIs covering the whole FOV would not be used to calculate tumour dose as this would include activity from surrounding tissues. Therefore the EANM and MRTDosimetry methods are more clinically relevant so it is suggested that these should be used rather than the total counts methods.

Normal counting mode was seen to have slightly higher calculated sensitivity compared with fast mode (6.3% and 9.1% higher with the MRTDosimetry and mIBG EANM methods respectively). This may be due to fast mode limiting the length of pulses analysed, causing fewer events to be detected than with normal mode at low count rates. Therefore different sensitivity factors should be used based on whether normal or fast mode are used. The deadtime factor for normal mode projections was around 1.02, therefore to reduce the need for deadtime correction lower activities should be considered for sensitivity calibration using this mode.

For the SEL-I-METRY trial Gregory et al reported a sensitivity per voxel of 10.64±0.53 MBq/ml/cps based on the plateau of the PVC curve plateau [53]. A different methodology was used and so the results cannot be directly compared with this work. It is noted that good accuracy was seen with validation using clinically realistic phantoms by Gregory *et al* [53]. This highlights that the key requirement for consistent methodology across

calibrations and patient measurements. However an investigation into the PVC calibrations was performed in Chapter 4.6, which found that if the plateau is unconstrained by the sensitivity then it can be highly dependent on range of volumes used for PVE calibration. Where there are large areas of uniform uptake a small VOI may be placed and no PVE corrections applied [22], which would not be appropriate if PVE method is used. Therefore it is suggested that the PVE calibration should not be used to define the sensitivity.

4.6. SPECT Partial Volume Effect Correction

4.6.1.Methods

Jaszczak cylinder phantoms with 10 to 31mm diameter fillable sphere inserts are commonly available in Nuclear Medicine departments for routine quality control testing and could be a practical option for PVC calibration. Jaszczak spheres with volumes of 0.5, 1, 2, 4, 8 and 16ml were filled by William Turner and James Scuffham, with an I-131 activity concentration of ~0.97MBq/ml at the time of scanning. SPECT/CT images were acquired with all the spheres positioned within a water filled Jaszczak phantom as seen in Figure 36(a), using both fast and normal mode. Each sphere was then scanned individually, without the other spheres present, in the same location within the phantom using fast mode.

Images were acquired in fast mode with the spheres together and individually to investigate the impact of imaging the spheres together. Images were acquired in normal mode to investigate the differences between the different modes and the spheres were acquired together due to time constraints. Longer acquisitions were performed for the smaller spheres due to their reduced activity, with 40s/view for the 0.5ml sphere, 30s/view for the 1ml sphere, 33s/view for all spheres together and 15s/view for the remaining spheres.

EANM I-131 mIBG dosimetry guidelines suggest a minimum sphere or cylinder diameter of 60mm for I-131 imaging [16]. Therefore to determine if larger spheres were required for partial volume effect calibration, additional spheres with diameters of 58, 66 and 73mm and volumes of 100, 150 and 200ml respectively were 3D printed by the National Physical Laboratory. These spheres were filled with ~0.10MBq/ml at the time of scanning and James Scuffham provided assistance with the phantom filling. A lower activity concentration was used for the larger spheres to reduce deadtime effects. The larger

spheres were then SPECT/CT scanned individually using both normal and fast mode, as shown in Figure 36(c), with a SPECT time per view of 15s. To investigate the impact of a large volume object on the partial volume correction model, the 6.8L uniform Jaszczak phantom fast and normal mode images described in Chapter 4.5.1 were also used.

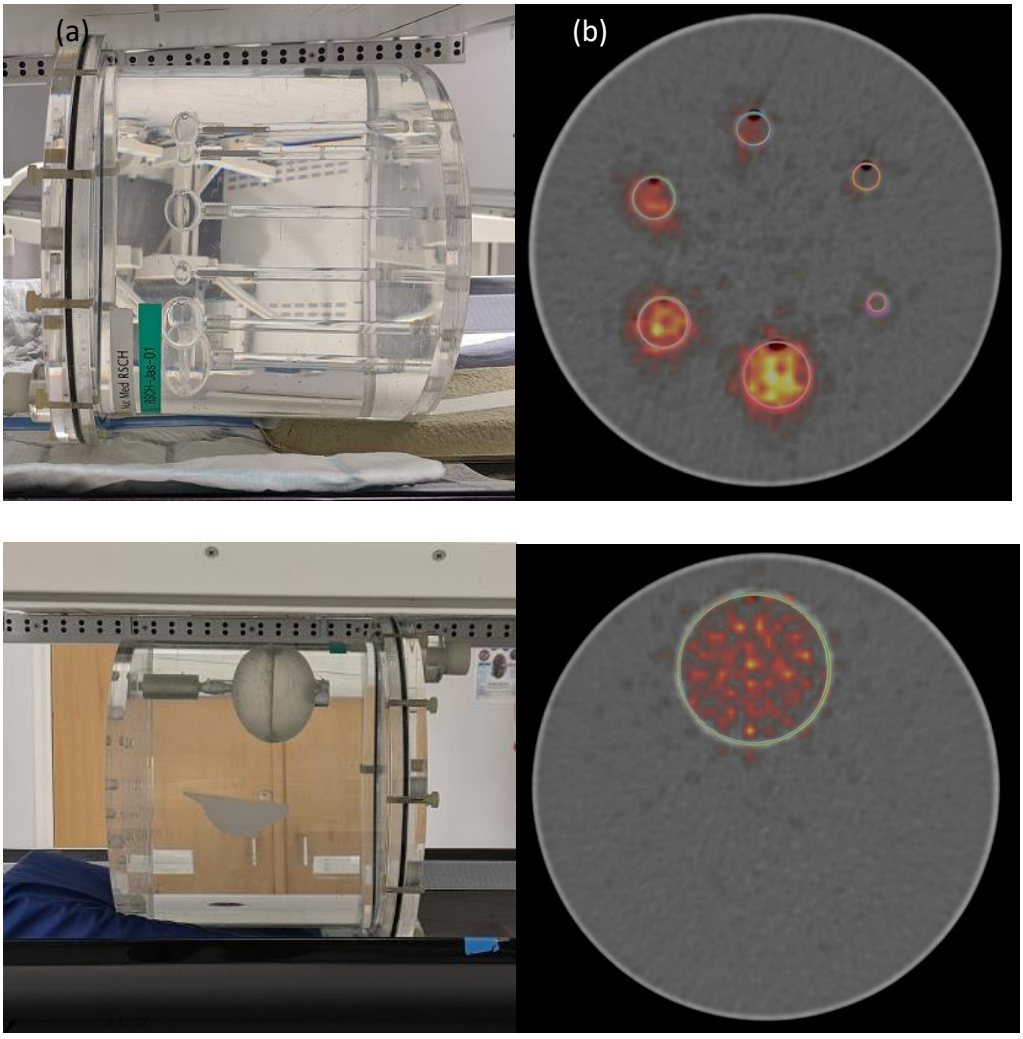

Figure 36. Phantoms and VOIs used for PVC calibration. Water filled Jaszczak phantom with (a-b) 0.5 to 16ml fillable sphere inserts (c-d) 200ml NPL printed fillable sphere insert. Examples of the VOIs used for analysis are given in (b) and (d) for the Jaszczak and 200ml NPL printed spheres respectively.

To investigate the difference between partial volume corrections performed using filled cylinders rather than spheres, the acquisitions of the cylinders described in Chapter 4.4.1 were performed in fast mode, with the cylinders scanned individually. The activity concentration was ~0.15MBq/ml at the time of scanning and 15s/view was used for the SPECT/CT scan.

All SPECT images were reconstructed as described in Chapter 4.5.1. Each set of fast and normal mode SPECT/CT images were loaded into Mirada General Oncology Review software and co-registered using the automatic rigid registration tool. VOIs were drawn using sphere/cylinders as appropriate on the fast mode acquisition, based on the CT with all spheres/cylinders present. They were then copied over to the other images with the spheres/cylinders and manually repositioned where required. 10 VOIs were drawn for each object to reduce potential VOI outlining errors, as shown in Figure 24. For the uniform Jaszczak images, the phantom had a significant downward tilt so a CT based threshold of -50HU to 50HU on the fast mode image was used to produce the VOIs instead.

For each VOI the mean counts per pixel and volume were exported from the Mirada software and the total counts per second, C_i, was calculated based on the known pixel size volume and acquisition time. The activity from the SPECT scan, $A_{SPECT,i}$, was then calculated using C_i, and the relevant MRTDosimetry method sensitivity, Q, given in Chapter 4.5.1. The sphere recovery coefficient, RC_i, was then calculated based on the activity determined from the radionuclide calibrator, $A_{calibrator,i}$, using Equation 32.

$$RC_i = \frac{C_i}{Q\ A_{calibrator,i}} = \frac{A_{SPECT,i}}{A_{calibrator,i}} \qquad (32)$$

The coefficients for Equation 13 were determined iteratively using OriginPro 2020b Simple Fit v3.00 tool, with non-weighted non-linear fitting. Graphs with the fitted functions displaying the 95% confidence band were also produced using OriginPro. To investigate the impact of setting the plateau (α) to 1, fits were performed with and without a constraint of 1. Fits were also performed using different sphere and Jaszczak combinations to determine the impact of using different phantoms. Weighting based on the measurement uncertainty was not used for the fitting, as this was not utilised in the EANM dosimetry uncertainty guidance [17].

Fit recovery coefficients (RC_{fit}) were calculated for each of the spheres and Jaszczak using their filled volumes and the fit parameters determined using different combinations of spheres and the Jaszczak. The difference between fit and measured RCs, ($\Delta RC = RC_{fit} - RC_{measured}$) was calculated, using the fast mode sphere and Jaszczak data with Jaszczak spheres imaged individually. The percentage difference between fit and measured RCs ($\Delta RC\% = (RC_{fit} - RC_{measured})/RC_{measured}$) was also calculated. Plots of ΔRC and ΔRC% as a function of volume was performed to investigate the errors introduced for the spheres

and Jaszczak using the different fitting methods. The RMSE for the fits performed was calculated based on the error in estimated recovery coefficients for the spheres and Jaszczak compared to the measured fast mode values with spheres acquired individually.

The standard uncertainty in the measured count rate was calculated using Equations 33 and 34 below, where a is the voxel length and d is the effective diameter of the object (assuming spherical volume, based on filled volume) and Equation 34 was taken from the EANM dosimetry uncertainty guidelines [17]. As the CT was used for outlining the volume uncertainty was taken to be due to voxelisation. The standard uncertainty in volume was taken from the balance precision.

$$\left[\frac{u(RC)}{RC}\right]^2 = \left[\frac{u(C)}{C}\right]^2 + \left[\frac{u(A_{calibrator})}{A_{calibrator}}\right]^2 + \left[\frac{u(Q)}{Q}\right]^2 \qquad (33)$$

$$\frac{u(C)}{C} = \frac{\varphi}{2RC}\frac{u(v)}{v} = \frac{\varphi}{2RC}\frac{3}{d}\left(\frac{a^2}{6}\right)^{0.5} = \left\{\mathrm{erf}\left(\frac{d}{\sigma\sqrt{2}}\right) - \frac{2\sigma}{r\sqrt{2}}\left[1 - e^{-\frac{d^2}{\sigma^2}}\right]\right\}\frac{1}{2RC}\frac{3}{d}\left(\frac{a^2}{6}\right)^{0.5} \qquad (34)$$

4.6.2. Results

The PVC calibration curve fit parameters for the different sphere, cylinder and Jaszczak combinations and GE acquisition modes investigated, with the fit plateau (α) unconstrained and set to 1 are given in Table 6.

Table 6. Partial volume correction curve fit parameters using the activity recovery coefficients from different combinations of phantom acquisitions for the fit. The phantoms used were Jaszczak "small" I-131 filled spheres with sizes of 0.5 to 16ml, "large" I-131 filled NPL printed spheres with 100 to 200ml volumes positioned and 1.7 to 100ml I-131 filled cylinders, all imaged within a water filled Jaszczak phantom. In addition a uniformly filled Jaszczak phantom was used. Imaging was performed with the "small" spheres "together" within the Jaszczak phantom or scanned individually. GE fast and normal modes were used.

GE Mode	Object Acquisition Method	Objects Included in Fit				PVC Fit Parameters, α unconstrained			
		Small Spheres	Large Spheres	Jaszczak	Cylinders	α	β	γ	RMSE
Fast	Individual	✓				0.58±0.07	0.86±0.08	9±3	0.045
		✓		✓		0.90±0.01	0.69±0.03	26±2	0.047
		✓	✓			0.72±0.02	0.74±0.04	16±2	0.008
		✓	✓	✓		0.92±0.03	0.56±0.03	42±7	0.017
					✓	0.63±0.02	0.79±0.05	9±1	0.026
	Small spheres together	✓				0.56±0.11	0.79±0.13	7±4	0.058
		✓	✓			0.75±0.03	0.65±0.04	16±3	0.017
Normal		✓	✓			0.89±0.04	0.60±0.03	22±4	22.407

GE Mode	Object Acquisition Method	Objects Included in Fit				PVC Fit Parameters α = 1		
		Small Spheres	Large Spheres	Jaszczak	Cylinders	β	γ	RMSE
Fast	Individual	✓				0.67±0.03	35±3	0.067
		✓		✓		0.51±0.05	60±15	0.020
		✓	✓			0.52±0.02	60±5	0.020
		✓	✓	✓		0.51±0.02	62±6	0.021

A graph of the differences between the measured and fit model recovery coefficients is given in Figure 37, given using different sphere and Jaszczak phantom combinations for the fit as well as with the fit plateau (α) unconstrained and also with it set to 1.

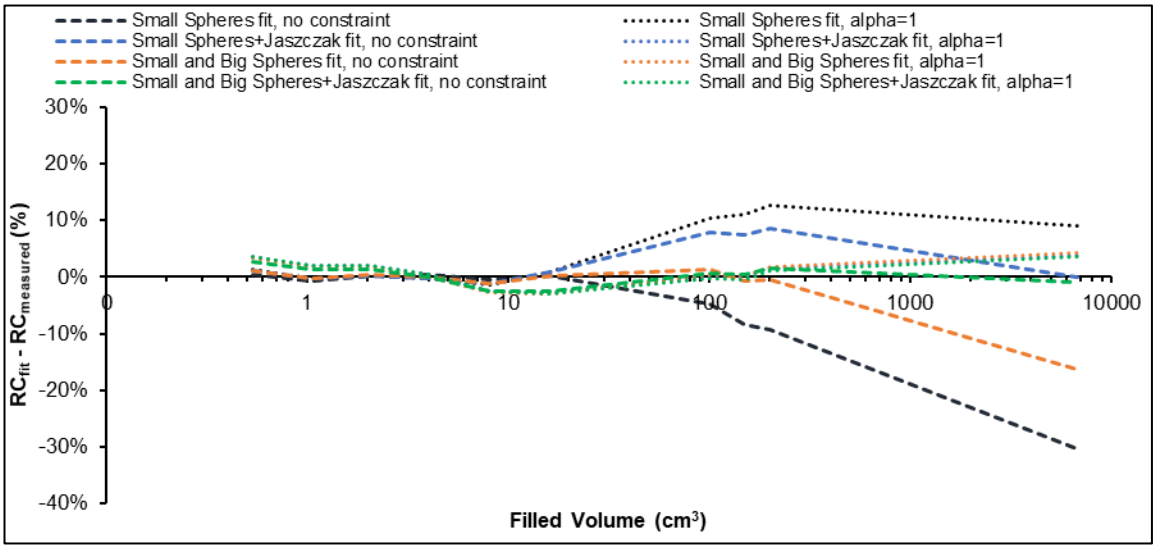

Figure 37 Difference between measured and model activity recovery co-efficients as a function of filled volume for different sphere and Jaszczak fitting methods investigated. Spheres were acquired indiviudally and all acquistions were performed in fast mode. The PVC fit was performed with no constraint on the plateua, alpha, and with it set to 1.

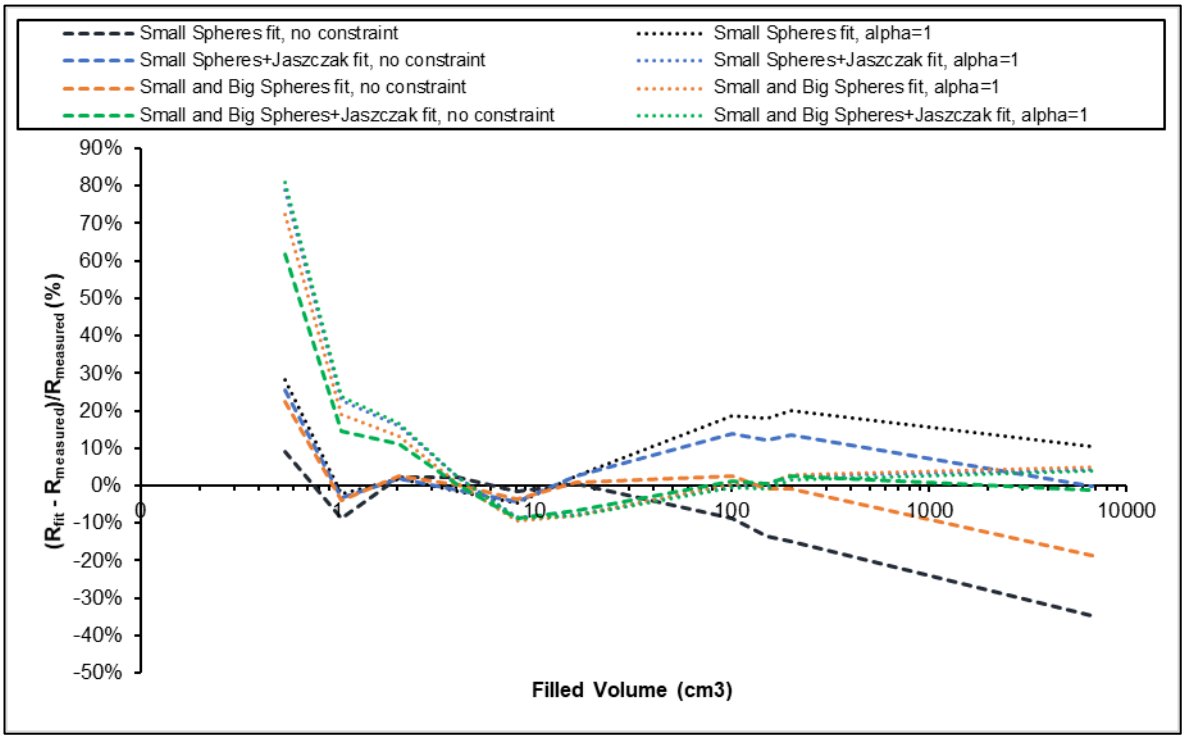

Figure 38 Percentage difference between measured and model activity recovery co-efficients as a function of filled volume for different sphere and Jaszczak fitting methods investigated. Spheres were acquired indiviudally and all acquistions were performed in fast mode. The PVC fit was performed with no constraint on the plateua, alpha, and with it set to 1.

Plots of recovery coefficients as a function of filled volume are given in Figure 39 to demonstrate the impact of the PVC fits for different imaging methods on objects of different sizes. This is given for the individually scanned spheres, cylinders and the

uniformly filled Jaszczak phantom in Figure 39(a), where the lines of best fit were plotted with the spheres or cylinder data and the Jaszczak data, with the plateau set to 1. In Figure 39(a) the impact of the 0.5 to 16ml Jaszczak spheres being imaged together or individually within a water filled Jaszczak phantom is demonstrated. The impact of fast and normal mode for the spheres and Jaszczak is demonstrated in Figure 39(c).

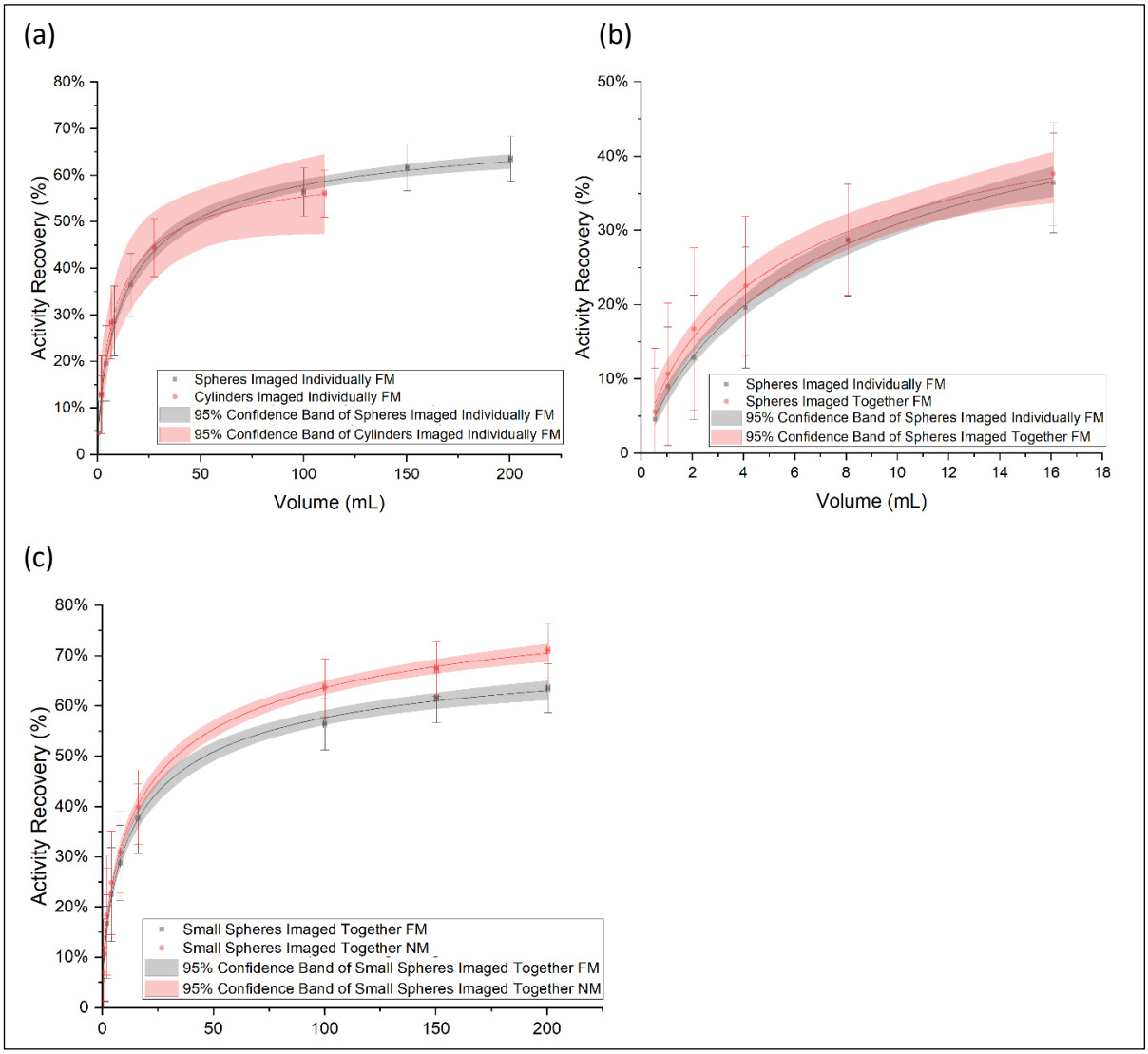

Figure 39. Plots of recovery coefficient as a function of object filled volume. Given for (a) fast mode individual acquisitions of spheres or cylinders; (b) fast mode acquisitions of the Jaszczak 0.5 to 16 ml spheres, imaged both together and individually; (c) fast and normal mode acquisitions with all spheres investigated, with the 0.5 to 16 ml spheres imaged together.

4.6.1. Discussion

Use of Jaszczak Spheres and Phantom for PVC Calibration

The impact of using the larger 3D printed spheres and Jaszczak, as well as choice of fit model can be seen through comparing the fit parameters in Table 6. Graphs of the difference and percentage difference between measured and fit recovery coefficients using the spheres data is given in Figure 37 and Figure 38 respectively. With α unconstrained it was seen that only using the small spheres for the model resulted in low differences between the modelled and measured recovery for the small spheres (ΔR = -0.8% to 0.4%, ΔR% = -8.9% to 9.0%), as expected. However this method was found to substantially underestimate the RC for the larger spheres (ΔR = -4.9% to -9.3%, ΔR% = -8.6% to -14.7%), while including the Jaszczak in the model caused the larger spheres to instead be overestimated (ΔR = 7.5% to 8.6%, ΔR% = 12.1% to 14.0%). Using the small and larger spheres for the fit model resulted in lower differences between model and measured RC for all spheres (ΔR = -1.1% to 1.4%), however the Jaszczak RC was substantially underestimated (ΔR = -16.4%). The percentage difference for the smallest sphere was high (ΔR% = 22.3%), but lower for the remaining spheres (ΔR% = -3.8% to 2.7%), which may be due to the higher uncertainty and relative impact due to size for the smallest sphere. Including all spheres and the Jaszczak in the model resulted in larger deviations between fit and measured RC for the spheres (ΔR = -2.5% to 2.8%) and large percentage deviations were seen for the smaller Jaszczak spheres (ΔR% = -8.7% to 61.8%).

Investigation into the impact of setting α to 1 found using small spheres only substantially overestimated the RC for the larger spheres and Jaszczak however for all other combinations, the fit parameters and difference between measured and fit recovery coefficients were largely similar. The difference in measured and fit RC was found to vary from -1.3% to 1.3% with small spheres only used for the model, with around -2.9% to 3.7% the other methods. However the percentage differences were much higher with α set to 1, with difference of 72.2% to 80.8% for the smallest sphere and -9.5% to 23.7% for the other spheres. This indicates that setting to plateau to 1 should not be performed where the objects of interest for dosimetry are typically small, as this could result in high errors.

From Figure 39 it can be seen that even when the 100-200ml spheres were included, a plateau in activity recovery does not appear to have been reached. This was also seen for non-resolution recovery data with cylinder volumes up to 200ml in the SEL-I-METRY trial [53] and in the example within the EANM mIBG dosimetry guidelines [16]. Without seeing

a plateau in activity recovery it is difficult to determine what the plateau should be. Setting the plateau to unity resulted high percentage errors in RCs for the Jaszczak spheres, which cover the typical size range of the thyroid and metastases [131]. This suggests that the poorer recovery is typically experienced and using a plateau of unity cannot be recommended. Using a uniformly filled Jaszczak phantom to simulate high volumes also gave high percentage errors in RCs. This suggests that the cylindrical Jaszczak shape cannot be seen as representative for the spheres or more data points are needed in between the volumes used to give a more representative curve.

With the plateau unconstrained and the 0.5 to 16 ml spheres used, high errors were seen for the 100 to 200ml volumes. However when the 100 to 200ml volumes were added the errors for the smaller spheres continued to be low. This suggests that PVC should not be performed with volumes greater than those for the calibration. Performing a PVC calibration with as many and as wide a range of sphere sizes as possible will reduce errors in the calculation. Therefore the calibration with 0.5 to 200ml spheres and no plateau constraint will be used as the optimal parameters.

However, if only thyroid residual tissue and metastases are to be investigated then the volumes will likely be less than 16ml [131] and therefore the Jaszczak spheres only could be used. As Jaszczak phantoms are typically available in Nuclear Medicine departments, this may help with the implementation of dosimetry for thyroid tumours. It is also noted that even with 100 to 200ml spheres full recovery was not seen and a plateau was not reached, therefore further work could be performed investigating the activity recovery for a wider range of sphere sizes. While resolution recovery was not used for this work due to the artefacts seen with high number of OSEM updates (see Chapter 4.4), further investigation could be performed with this reconstruction, possibly with lower updates than required for convergence.

Comparison of Spheres and Cylinders for the PVC Calibration

The impact of using spheres and cylinders can be seen Table 6, which gives the fit parameters using available spheres and cylinders. Figure 39(a) also gives of plot of activity recovery as a function of filled volume for the spheres and cylinders, as well as the PVC fit curves with 95% confidence bands. It can be seen that the fit curves for the spheres lie within uncertainties of the fit curve for the cylinders, therefore the choice of spheres or cylinders appears to give a similar PVC calibration. This supports to use of spheres or

cylinders being used for PVC calibrations in different literature sources [16], [17], [53]. However further investigation should be performed into use of cylinders with different lengths and on the PVC calibration and impact for patient dosimetry.

The curve 95% confidence limits appear to be larger for the cylinder data, therefore the sphere data will be used for the PVC calibration. The wider 95% confidence limits for the cylinder curve may be related to the use of a cylinder VOI to outline and some of the cylinders not being parallel to the axis of rotation. Further investigation into the impact of the method VOI outlining could be performed, for example use of CT or SPECT thresholding tools or impact of multiple operators for outlining. The wider 95% confidence limits could also be due to the smaller number of object sizes used for the calibration, therefore further work could investigate using more cylinder sizes. This work also only investigated 38mm long cylinders so further work could be performed to investigate the impact of cylinders of different diameters. It is expected that if the surface area was substantially different with spheres of the same volume then it is more likely that differences would be seen between cylinders and spheres.

Impact of Acquiring the Jaszczak Spheres within the Same Phantom

A graph of Jaszczak spheres imaged individually and together is given in Figure 39(b) and shows that the spheres imaged together were seen to have higher activity recovery, particularly for the smaller spheres. This may be expected due to scatter from other nearby objects being detected within the VOI, which will affect the smaller spheres used experimentally more due to their lower activity. For the SEL-I-METRY trial the PVC cylinders were imaged together and it was stated that this was representative of the trial patients who typically have multiple areas of nearby disease with I-131 uptake [53]. However for the broad case mix at RSCH, patients with small volumes of I-131 uptake can be seen at varying distances from areas with high uptake. For example, metastatic nodes could be near remnant thyroid tissue but equally in disease recurrence there could be no nearby areas with high uptake. Further work could investigate methods to correct for the impact of proximity to nearby areas with I-131 uptake and their relative I-131 activity. A simple method for correction could be background correction with a representative region. However identifying a representative region could be challenging where there are multiple nearby areas with high uptake as well as tissue uptake in the region. Alternatively, a model of the impact of nearby objects could be built experimentally using

SPECT images and used for correction. Improved scatter and CDR reconstruction corrections could be investigated. However for this work it will be assumed that the objects imaged individually give the best model of the PVE.

The difference between the activity recoveries using the different imaging methods is within the measurement uncertainties and the fitted curves for the Jaszczak spheres with α of 1 had overlapping 95% confidence intervals. Therefore imaging the Jaszczak spheres together appears to give similar PVC calibration results, compared to imaging them individually. This suggests if there is limited time for calibration measurements then the spheres could be imaged together. However as a small increase in activity recovery was seen with the spheres imaged together, it is recommended that the objects should be imaged individually if possible. Therefore the data with spheres imaged individually will be used for the PVC calibration in this work. As only one set of measurements was performed for the spheres imaged separately and together, further statistical analysis of the difference between the measurement methods could not be performed. Therefore further work could be performed with repeat imaging of the spheres individually and together, so this assessment could be performed. Cylinders are also frequently used for calibration, therefore to determine if these could be imaged together similar work should be performed.

Impact of Using GE Fast Mode Compared to Normal Mode

A graph of recovery coefficient as a function of filled volume of all Jaszczak spheres imaged together within a phantom using normal and fast GE acquisition mode is given in Figure 39(c). The activity recovery with normal mode was seen to be slightly higher than with fast mode for all objects. Therefore fast mode appears to operate differently from normal mode even with low deadtime conditions and based on this it should not be used for routine diagnostic scanning without further investigation. There is limited information available regarding the operation of GE “fast mode”, however it appears to limit the pulse length analysed and has been seen in Chapter 4.5 to reduce the SPECT sensitivity. This could be impacting on the scatter correction, giving worse contrast and activity recovery. However further work is required to investigate the clinical impact of fast mode, such as spatial resolution and ability to detect objects with varying signal to background ratios.

Due to the differences observed in sensitivity and activity recovery within the work it is also suggested that patient dosimetry imaging should not switch between fast and

normal modes unless full characterisation of both modes has been performed. As fast mode is required for early dosimetry imaging, the suggested dosimetry protocol for imaging will be using GE fast mode. Other systems such as those by Siemens and Philips switch between normal and high count rate modes automatically [16], [53], therefore the impact of the change on sensitivity and activity recovery could also be instigated.

4.7. Tumour S-factors calculation

4.7.1. Methods

Tumour self-irradiation S-factors were calculated using the OLINDA/EXM 1.0 unit density uniform sphere model for I-131 [26]. This model gave S-factors for discrete sphere masses in the range 0.01–6000g based on pre-calculated electron- and photon absorbed fractions [26].

The OLINDA/EXM 1.0 software supporting documentation suggests that "is best to fit a simple function through the results" [132] and literature suggest a power fit gives good agreement [16], [133]. Therefore a power fit was performed in OriginPro following Equation 35 using the OLINDA sphere data for I-131 and the fitting parameters obtained.

$$S = a\, m^{-b} \qquad (35)$$

4.7.2. Results

A graph the OLINDA S-factors for I-131 spheres self-irradiation as a function of mass is given in Figure 40. The fit parameters were a = 111.4±0.2 and b = 0.9697±0.0004.

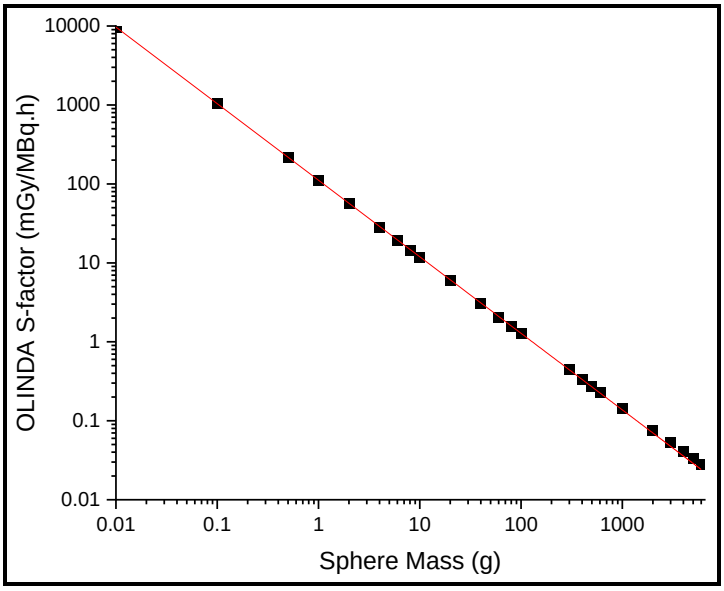

Figure 40 OLINDA S-factor for I-131 sphere self-irradiation as a function of mass.

4.7.3. Discussion

The formula for calculating I-131 self-irradiation S-factors for a sphere has been calculated from OLINDA 1.0 and will be used for calculating tumour self-irradiation dose. This method assumes patient tumours will be a homogeneous and spherical, while in reality uptake is likely to be heterogeneous and likely areas of tumour such as residual thyroid, lymph nodes and lung metastases are likely to be non-spherical. There may also be areas of nearby I-131 uptake which would provide cross-irradiation dose e.g. for a metastatic lymph node near the thyroid region. However this represents the best method for performing dosimetry that is practical for many sites who do not have specialist dosimetry software. Further work could investigate the use of Monte Carlo modelling with clinically relevant tumours and the comparative difference in S-factor.

5. Planned Dosimetry Procedure

5.1. Introduction

A method for performing post therapy verification dosimetry for I-131 NaI therapy in thyroid cancer patients was developed based on the literature review given in Chapter 2, experimental work performed in Chapters 3 and 4, as well as knowledge of what may be possible to implement at RSCH. Flow charts for the planned dosimetry procedure were produced and are given in Appendix 1. Further details regarding the planned method are given in the subsections within this Chapter.

5.2. Measurement Time Points

The literature review identified that for bone marrow dosimetry measurements at 2, 6, 24 and 96 and 144 hours post administration were recommended in EANM guidelines [115], with a 48 hour measurement also being common within literature. Work given within Chapter 3.6 found whole body retention measurements at 7 days post therapy gave up to a 6% increase in measured residence time and so late measurements around this point appear to be beneficial. For tumour dosimetry the literature review found gamma camera imaging with 3 to 4 time points was typically performed, with 24-48 hours commonly used for the first time point (deadtime allowing) and 72-216 hour for a late time point and maximal tumour uptake normally seen around the 24 hour time point, with imaging at 4±1 and 8±1 hours also suggested if possible [34], [53], [59], [77], [110], [111]. For the GE Optima system deadtime at greater than 2h post administration is not expected to be

an issue if fast mode is used [53] (see Chapter 4.3), therefore earlier measurements could be performed.

It was thought that ideally gamma camera scanning should also be performed at the end or start of the working day when the hospital is quieter, to reduce doses to members of the public and reduce disruption to the scanning department. Therefore it was decided that the first scan should be scheduled for the end of the working day, which will also likely be required to give sufficient time post treatment, with subsequent scans at the at start of working day following gamma camera QC testing. Imaging at the start of the working day also has the advantage that the gamma cameras are more likely to be available, due to delays between injection and imaging being required for most diagnostic studies. For I-131 thyroid cancer treatments at RSCH patients are typically administered with I-131 on a Monday. For radiation protection reasons those administered with 1.1GBq are discharged on a Tuesday, with other patients typically being discharged on a Wednesday based on their I-131 clearance. For logistical reasons, measurements when the patient would be likely to already be on site were planned, with blood sample and whole body retention measurements being performed at similar times to minimise disruption to the patient and staff. As whole body retention measurements require limited resources it was decided that these should also be performed at least twice a day during the inpatient stay. Therefore it was decided that the measurement time points given in Table 7 should be used.

Table 7. Planned measurement time points post I-131 administration

Planned measurement time point	Comment	Imaging	Blood sample	Whole body probe retention
0 (administration)	Monday 12:00-14:00 expected			
2h			✓	✓
4-6h	Schedule scan for Monday 18:00	✓	✓	✓
18-22h	Schedule scan for Tuesday 8:30	✓	✓	✓
26-30h	Around end of working day if still inpatient			✓
42-46h	Schedule scan for Wednesday 8:30	✓	✓	✓
Morning and evening while an inpatient				✓
162-166	Schedule scan for following Monday 8:30	✓	✓	✓

5.3. Blood and Bone Marrow Dosimetry

For bone marrow dosimetry it was decided that whole body residence time should be measured and calculated using the optimal methods determined in Chapter 3. This involved measurements using a Radhound positioned 3m away from the patient using a trolley, with three 60s anterior and posterior measurements performed for each measurement. For the residence time calculation, this involved an in house Excel spreadsheet using bi-exponential clearance fitting of the geometric mean data. As the patient would be leaving the therapy room for gamma camera scanning, background measurements could be performed at these points and interpolation between background measurements could be performed. If an inpatient background measurement was omitted this could cause an error of -2.2% to 3.8% in residence time and so should be added to the quoted uncertainty. Likewise, if only anterior whole body measurements were performed this could add an error of -6.3% to 5.0% and not performing an additional late time point at 7d post administration could add an error of -5.9% to -0.5%. Therefore these errors should be included in the whole body residence time uncertainty if relevant.

For blood residence time calculation it was decided that three 1ml samples should be taken for each time point, measured on one of the Wallac Wizard gamma counters within the department with background samples at the start and end of counting. The sample activity concentration could be calculated from the mean net count rate for each time point using the sensitivity factors of 432±22 cps/kBq for the Wallac Wizard 1480 counter and 425±21 cps/kBq for the Wizard2 2480 counter measured in Chapter 3.8. Previous work at RSCH had found the 1ml activities from early patient blood samples could result in large deadtime within the counter. Therefore the samples should be counted one week following administration, which could be performed just after the last planned blood sample. At this time point count rates of approximately 7,000cpm were seen, therefore in order to ensure good counting statistics it was decided that each sample should be counted for 20 minutes. Due to the delay between taking the samples and counting them, the sample activity concentrations should be decay corrected to the time each sample was taken. To calculate the blood time integrated activity it was decided that a bi-exponential fit to the data should be performed iteratively using Excel Solver with starting points determined through curve stripping, using the methodology described in Chapter 3.2.

Based on the literature review it was decided that the blood and bone marrow dose should be calculated using Equations 7 and 8, in line with the EANM guidelines [20], [21].

5.4. Tumour Dosimetry

Tumour dosimetry for I-131 can be performed using planar or SPECT/CT gamma camera imaging, as discussed in Chapter 2.4.1. As all gamma camera systems at RSCH have SPECT/CT capability it was decided that SPECT/CT should be used for improved quantitative accuracy.

For tumour dosimetry the patient acquisition method should match that used for the calibrations, therefore it was decided the acquisition parameters detailed in Chapter 4.2 should be used. In order to match the current post I-131 therapy SPECT acquisition duration used at RSCH, is was decided that 20s per projection should be used with 120 projections. To correct for deadtime and scatter, correction of the SPECT projections using the in house software detailed in Chapter 4.5.1 and TEW non-paralysable deadtime of 6.91±0.08 μs determined in Chapter 4.3 is planned. SPECT reconstruction of the corrected projections using GE Volumetrix software was planned with the optimal reconstruction OSEM parameters of 60 iterations, 10 subsets and no filter with CT attenuation correction, as determined in Chapter 4.4. It was found that noise within this reconstruction would make it difficult to use for tumour outlining so the current clinical reconstruction should also be produced for outlining purposes.

The GE Dosimetry Toolkit and Q.Volumetrix MI tools in Xeleris version 4 were also investigated for VOI analysis with the GE Healthcare applications specialist but were found to not be suitable for the dosimetry planned. Therefore it was decided that VOI outlining of the tumour should be performed using Mirada software, which was already in use within the hospital for radiotherapy treatment planning and for Y-90 microspheres therapies. It was decided that VOI outlining based on the CT and clinical SPECT reconstruction should be performed for the first scan or where the tumour is most visible, SPECT/CT images from all time points should be registered, VOIs copied over and positions adjusted as required.

Due to a specialist dosimetry software package not being available, the development of in house software to calculate the tumour dose from the VOI volumes, counts and scan was required and was performed using Excel. It was decided that partial volume correction of the total counts should be performed using Equation 13 based on the VOI volume and optimal parameters determined in Chapter 4.6 (α = 0.72±0.02, β = 0.74±0.04 and γ =

16±21). SPECT sphere activity could then be calculated based on the PV corrected total counts and fast mode sensitivity of 22.3±0.9MBq/ml (determined in Chapter 4.5) using Equation 31. It was decided that activity fit parameters should be calculated iteratively using Excel Solver to minimise the activity fit RMSE in a similar manner to that previously described for bone marrow dosimetry method. With this method the Solver starting points used curve stripping but for tumour dosimetry mono-exponential uptake and clearance was assumed. As this method involved curve stripping, rather than using the EANM method given in Equation 14, the activity, $A_{target}(t)$ and time integrated activity, $\tilde{A}_{target}$, were calculated using Equations 36 and 37 respectively [83]

$$A_{target}(t) = \mathrm{A}_1 exp(-\lambda_T t) - \mathrm{A}_2 exp(-\lambda_B t) \quad (36)$$

$$\tilde{A}_{target} = \int_0^\infty A_{target}(t)\, dt = \frac{A_1}{\lambda_T} - \frac{A_2}{\lambda_B} \quad (37)$$

where A_1 and A_2 are fitting parameters, and for the solver $\mathrm{A}_1 = \mathrm{A}_2$ and $A_1 = A_0\left(\frac{\lambda_t}{\lambda_B - \lambda_T}\right)$. This method also has the advantage that it does not require the measured administered activity when used for patients, removing an area of uncertainty. The clearance phase curve stripping parameters A_1 and λ_T were calculated from a linear fit of times post administration and natural logarithm of the activity, excluding measurements before the maximum activity was seen. The estimated activity from the clearance phase, $A_{cstrip}(t)$ was then calculated ($A_{cstrip}(t) = A_1 exp(-\lambda_T t)$) and the difference between the estimated and measured activities, ΔA, was then calculated ($\Delta A = A_{cstrip}(t) - A_{measured}(t)$). Uptake phase parameters A_2 and λ_B were calculated from a linear fit of times and natural logarithm of ΔA, excluding measurements after the maximum activity was seen or when negative ΔA values were calculated. The parameters $\mathrm{A}_1, A_2, \lambda_T$ and λ_B calculated using curve stripping were then used as starting points for the Excel solver iterative calculation, with conditions that the fitting parameters must be greater than or equal to 0.0001 and λ_T must be greater than the physical decay constant for I-131. The time integrated activity was then calculated using Equation 37 with these fit parameters. The S-factor was calculated based on the mean VOI volume using Equation 35 with parameters a = 111.4±0.2 and b = 0.9697±0.0004 (determined in Chapter 4.7) and the dose was calculated from the S-factor and time integrated activity using Equation 38.

$$D = \tilde{A} \times S \quad (38)$$

5.5. Other Factors for Consideration

While the dosimetry procedure has not yet been implemented there are a number of additional factors identified to enable dosimetry to be implemented. For example, the procedure requires blood samples and patient scans at approximately 6 hours following therapy administration and the RSCH Nuclear Medicine department closes at 7pm, so if scanning takes up to 1 hour then administration will need to occur at around 12pm. At RSCH the process prior to this work was for patients to attend the hospital for Thyrogen injections on the Saturday and Sunday prior to therapy on the Monday, then have blood samples taken on the Monday to determine if they were fit for treatment. This meant that patients were frequently not treated until around 5pm due to delays in blood sample processing and clinician availability to review the results. The process was reviewed and it was decided that the key blood tests to determine eligibility for treatment (e.g. TSH, eGFR) should be performed on the Sunday prior to therapy, which has brought the typical treatment times to between 11am and 2pm.

A radiation risk assessment needs to be performed prior to dosimetry implementation [15] and the large initial dose rates from these patients mean measures need to be taken to reduce dose to staff and members of the public. Procedures considered at RSCH were rehearsal of patient positioning on the gamma camera prior to treatment to reduce staff dose; patients changing into a gown in therapy room prior to scanning; giving patients overshoes when leaving the therapy room; methods for restricting access to the lift used by the patient to travel between the therapy and scanning rooms; patients to travel directly between the therapy and scanning rooms rather than staying in the waiting room; a lead barrier for taking blood samples and; access to EPDs for all staff that may come into contact with patient.

Methods to assist with reproducible patient scanning and translation of VOIs between different measurement time points should be considered, such as using vacuum bean bags or other immobilisation devices commonly used within external beam radiotherapy. However it would need to be ensured that these would not cause a significant increase in staff dose.

The use of in house software should be minimised where possible and where this is not possible it must have appropriate testing and documentation in line with the Medical Device Regulations [134], [135]. Therefore the amount and complexity of in house software was minimised with the planned dosimetry method wherever possible.

6. External Validation of Tumour Dosimetry Methodology

6.1. Introduction

Tumour dosimetry for molecular radiotherapy requires a number of calibrations and for many sites this will require the implementation of in house software for some of the calibrations and analysis. Within external beam radiotherapy the NPL have been performing dose audits for over 20 years [136]. A range of dose audits are performed within radiotherapy to give consistency, improve technique, provide assurance on technique and harmonise practice for clinical trials [136]–[138]. Metrology centres were involved in the investigation of molecular radiotherapy dosimetry techniques as part of the MetroMRT and MRTDosimetry projects [61], [139]. However, while it is common for metrology centres to provide services for radioactivity measurement [128], molecular radiotherapy audit and validation services have not yet been implemented. Therefore work was performed with NPL to develop a technique for external audit of molecular radiotherapy dosimetry technique, focussing on tumour dosimetry. This was then tested using the planned dosimetry method given in Chapter 5. This work focussed on tumour dosimetry as it requires multiple calibrations and therefore is most likely to benefit from external testing.

6.2. Tumour Dosimetry

6.2.1.Methods

In conjunction with the NPL a method was developed to validate the planned tumour dosimetry methodology, focussing on verification that the calibrations and fitting methods planned were applied correctly and gave reasonable results. As the PVC and S-factor calibrations are most commonly produced using spheres, it was decided that a test of these calibrations should be performed using a sphere. A clinically realistic tumour size, between the sphere sizes used for PVC and S-factor calculations was desirable. Therefore a 13ml sphere was chosen for the validation as it was between the 8 and 16ml Jaszczak sphere sizes used for PVC calibration, as well as the 10 and 20ml OLINDA sphere sizes using for the S-factor calibration. Multiple spheres with 13ml internal volume were 3D printed by NPL to be scanned within a water filled Jaszczak phantom, as shown in Figure 41. A biokinetic model and ground truth dose were calculated by Ana Denis-Bacelar from the NPL, who also provided software for uncertainty analysis. The spheres were filled with

I-131 and scanned on the RSCH Optima 640 scanner, with the target activities used corresponding to set biokinetic model time points. SPECT/CT scanning and dose calculation was performed in accordance with the procedures given in Chapter 5 and compared to the ground truth.

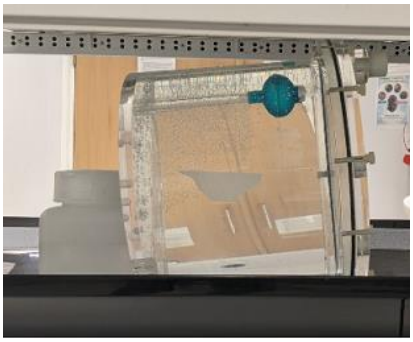

Figure 41. Positioning of 13ml 3D printed sphere within a water filled Jaszczak phantom. Shown with tub used for deadtime check present.

NPL Biokinetic and Dosimetry Model

A biokinetic model for thyroid remnant uptake and clearance within euthyroid patients was produced by NPL based on their review of available literature. This review found that most publications did not report sufficient information to enable the biokinetic model to be built. The most complete publication found was by Hänscheid et al, which gave remnant retention at 48h, effective half-life and residence time for 33 euthyroid cancer patients [140]. In this publication imaging started at 48h post administration [140], however the typical point of maximum uptake has been reported to occur at around 24h [109]–[111]. This was accounted for using a mono-exponential uptake and mono-exponential clearance. A lognormal distribution was then used to calculate the fitting parameters given in Equation 14 based on this data, giving λ_t = 3.4971E-04 h^{-1}, λ_T = 0.01268 h^{-1} and λ_B = 0.0771 h^{-1}.

For the validation exercise it was assumed 5500MBq I-131 was administered and scanning with sphere activities corresponding to set time points within the biokinetic model was planned. The planned time points matched those given in Chapter 5.2 and some additional times were included as a check of optimal time points. The fractional retentions and the sphere target activities supplied by NPL for the planned time points are given in Table 8. Using these fitting parameters and Equation 38 given in EANM 2013 benign thyroid disease pre-therapy dosimetry guidelines [18], the time integrated activity was calculated to be 1968.3 MBq.h by NPL.

A S-factor for the sphere was calculated to be 8.96882 mGy.MBq^{-1}.h^{-1} by NPL using EGS++ class of the EGSnrc general purpose radiation transport simulation Monte Carlo code [141], [142]. A homogeneous unit density water filled 13ml sphere containing 10MBq I-131 was modelled, within an infinite water medium and decay data from the RADTABS MIRD/ICRP 107 DECDATA was used [143]. The uncertainty in the measurement was calculated by EGSnrc based on the statistical uncertainty using a history-by-history method [144].

Table 8. Initial planned "tumour" fractional I-131 retention and activities for given time points post administration using the NPL biokinetic model and an administered activity of 5500MBq. Difference between planned and actual activity at scan is given for comparison.

Scan Time Point P.A. (h)	Fractional Retention	Sphere Activity	
		Planned (MBq)	Activity at scan deviation (%)
5	1.403E-03	7.717	-0.2%
20	3.051E-03	16.783	-5.8%
44	2.925E-03	16.090	-6.7%
72	2.158E-03	11.871	-2.0%
96	1.604E-03	8.825	-2.7%
120	1.186E-03	6.521	0.1%
144	8.749E-04	4.812	-3.8%
164	6.790E-04	3.735	-1.1%
196	4.526E-04	2.490	-2.5%
220	3.339E-04	1.837	-1.4%

Testing at RSCH

Six 3D printed 13ml spheres supplied by NPL were filled with I-131 at RSCH and scanned over the course of 8 days, to give as close as possible to the planned activities at scan time. The spheres were filled using two stock vials and the activity concentrations were later measured by NPL to reduce errors due to the local calibrator. The I-131 stock solution was drawn up and injected into the spheres using 1ml and 2.5ml syringes and the weight of stock solution drawn up, $w_{syringe}$, was calculated based on syringe measurements with a Kern ABJ-NM/ABS-N balance. The syringe activities before and after injection into the spheres were measured using a Capintec calibrator. The sphere I-131 activities, $A_{sphere}(T_{ref})$ at reference time T_{ref}, were then calculated using Equation 39, where C_{stock} is the activity concentration of the I-131 stock solution at time t_0, A_2 is the measured syringe activity before injection into the sphere at time t_2 and A_3 is the measured activity of the syringe after injection into the sphere, measured at time t_3.

$$A_{sphere}(T_{ref}) = \left(C_{\text{stock}} w_{syringe} e^{-\lambda(t_{ref}-t_0)}\right)\left(1 - \frac{A_3 e^{-\lambda(t_{ref}-t_3)}}{A_2 e^{-\lambda(t_{ref}-t_2)}}\right) \quad (39)$$

The spheres were scanned individually within a water filled Jaszczak phantom as shown in Figure 41. A radioactive background was not feasible due to the need to perform acquisitions with different sphere phantoms and a limit on the number of Jaszczak phantoms available. The same sphere could not be used for all acquisitions due to concerns regarding spheres leaking with time and gamma camera access for some of the acquisition times that would be required. Acquisitions were performed on the GE Optima gamma camera with acquisition parameters as given in Chapter 4.2, with an acquisition duration of 20s per projection.

The sphere activities were not sufficiently high to test the deadtime correction. Therefore to simulate the impact of a nearby area with high uptake and assess the deadtime correction a 355ml tub with 190MBq I-131 was positioned at the end of the Jaszczak phantom, as shown in Figure 41.

Table 9. 13ml sphere time points following adjustment by NPL and measured activities.

NPL adjusted time p.i. (h)	Sphere number	Calibrator Activity at scan (MBq)
4.10	4	6.57±0.10
14.74	1	15.19±0.76
44.72	1	15.99±0.80
73.50	2	11.66±0.17
98.01	3	8.61±0.13
106.30	4	7.75±0.12
146.60	5	4.66±0.07
164.37	4	3.72±0.06
195.75	7	2.50±0.04
218.86	7	1.86±0.03

Deviation between planned activity and decay corrected calibrator activity at time of scan was -6.7% to 0.1% (see Table 8) due to difficulties in preparing precise volume using the syringes available and delays in scanning. This would have resulted in additional errors

between site calculated dose and known dose calculated by NPL, which were not due to the planned patient dosimetry method. Therefore, to remove this source of error the calibrator activities at time of scan were reported to NPL and the "time points" were adjusted by NPL based on the biokinetic model to those given in Table 9.

The dose was then calculated using the planned dosimetry method outlined in Chapter 5.4. Sphere SPECT images were reconstructed using GE Xeleris software with the TEW and deadtime correction and 60 iterations 10 subsets, as described previously in Chapter 4.5.1. Spherical VOIs were outlined using Mirada software based on the CT and from this mean counts, total counts and volume from the VOI were determined. The mean VOI volume was 13.00 cm^3 (minimum of 12.76 cm^3 and maximum of 13.54 cm^3) and was 0.04% higher than the phantom internal volume of 13ml. Partial volume correction of the total counts was performed using Equation 13 for each acquisition based on the relevant VOI volume, and PVC factors α = 1, β = 0.51±0.02 and γ = 62±6 (optimal factors determined in Chapter 4.6). SPECT sphere activity was calculated based on the PV corrected total counts and fast mode sensitivity of 22.3±0.9MBq/ml (determined in Chapter 4.5) using Equation 31.

Activity fit parameters λ_t, λ_T and λ_B were calculated iteratively using the planned local method with Excel Solver to minimise the activity fit RMSE, assuming mono-exponential uptake and clearance (see Chapter 5.4). The time integrated activity was then calculated using Equation 37 with these fit parameters.

The mean VOI volume was then used to calculated the S-factor using Equation 35 with parameters a = 111.4±0.2 and b = 0.9697±0.0004 (determined in Chapter 4.7). The product of the S-factor and time integrated activity was then used to calculate the dose, as given in Equation 38.

The uncertainties in the activity fit parameters, time integrated activity and dose were calculated in accordance with the EANM uncertainty guidelines [17], using a program provided by NPL and run using Matlab (v2020b, MathWorks). The sensitivity, PVC calibration and 13ml sphere acquisition counts and volumes were inputted into the software. The dose was then calculated in a manner similar to the planned procedure and the uncertainty was calculated. The mean sphere volume was taken to be the standard deviation in the VOI measurements. The difference in calculated parameters using the Matlab NPL program was less than 0.3% compared to the RSCH Excel method.

Further investigation was then performed to investigate the errors introduced from the different components of the dose calculation using the planned method. The time integrated activity and dose were calculated using all measured SPECT data and with just the data from time points closest to those planned at RSCH (4.10, 14.74, 44.72, 164.37h). The biokinetic model activities for the planned dosimetry time points (6, 21, 45, 164h) were also used to calculate the time integrated activity and dose. To investigate the errors introduced from the sensitivity and PVC methods as well as deadtime correction, a graph of percentage difference between sphere activity calculated from the SPECT scans and the calibrator measurements, given as a function of calibrator activity was produced.

6.2.2. Results

A plot of percentage difference between sphere SPECT and calibrator calculated activity as a function of calibrator activity if given in Figure 42. The activity for individual spheres within the Jaszczak phantom can be seen to be 2.6 to 10.2% higher with the SPECT measurements compared to the radionuclide calibrator measurements. When a pot containing ~190MBq I-131 was positioned at the end of the Jaszczak phantom, the sphere SPECT activity measurement increased to 19.7% higher than the calibrator activity. However, for the deadtime pot the SPECT activity was calculated to be only 8.0% higher than the calibrator activity.

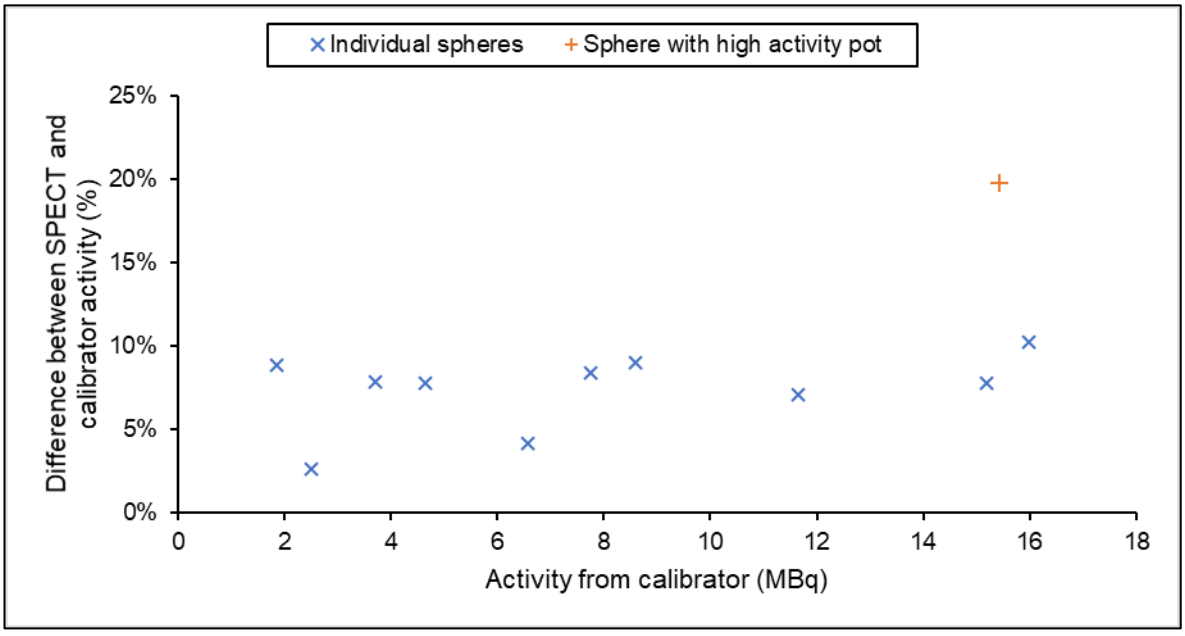

Figure 42. Difference between SPECT and calibrator calculated activities as a function of calibrator activities for 13ml spheres scanned individually within a Jaszczak phantom. Results are also given for a sphere when a tub containing 190MBq I-131 was placed at the end of the Jaszczak phantom.

The fit parameters, time integrated activity, S-factors and doses calculated using the different methods investigated are given in Table 10, along with the NPL results and differences between the local and NPL results.

Table 10. Fit parameters and doses calculated for 13ml sphere validation data.

Parameter	NPL	Local method			% difference between local and NPL results		
		Model activity data	Measured SPECT activity data		Model activity data	Measured SPECT activity data	
		Planned points	All points	Planned points	Planned points	All points	Planned points
λ_t [h^{-1}]	0.000350	0.000350 ±0.000001	0.00038 ±0.00001	0.00037 ±0.00001	-0.0002%	5.4%	4.4%
λ_T [h^{-1}]	0.01268	0.01267 ±0.00002	0.0130 ±0.0002	0.0130 ±0.0002	-0.0027%	2.6%	2.7%
λ_B [h^{-1}]	0.0771	0.0771 ±0.0001	0.073 ±0.001	0.072 ±0.001	0.0012%	-4.7%	-6.6%
$\tilde{A}_{target}$ [MBq.h]	1968	1967 ±268	2120 ±216	2140 ±387	-0.04%	7.7%	8.7%
Mean sphere volume (cm^3)	13	13	13.00 ±0.21	12.91 ±0.08	N/A	0.04%	-0.66%
$S_{target \to target}$ [mGy.MBq^{-1}.h^{-1}]	8.97 ±0.27	9.26 ±1.67	9.26 ±1.67	9.32 ±1.67	3.3%	3.2%	3.9%
D [Gy]	17.65 ±0.53	18.22 ±1.48	19.63 ±2.11	19.58 ±2.15	3.2%	11.2%	13.0%

6.2.3. Discussion

From Figure 42 it can be seen that the SPECT activity was overestimated by 2.6 to 10.2% for the 13ml spheres within a water filled Jaszczak phantom, with no dependence seen between activity at time of scan and SPECT error. This indicates that Poisson noise did not have a substantial impact on activity recovery with planned clinical acquisition duration. Adding a tub containing 190MBq I-131 to the end of the Jaszczak phantom caused the 13ml sphere SPECT activity to increase to 19.7% higher than that measured using a radionuclide calibrator. However, the activity within the tub was only 8.0% higher and within the uncertainty range seen for the lower activity 13ml spheres. It is likely that the 13ml sphere SPECT activity was overestimated due to errors with PV corrections for this small volume (RC = 34±8%) and due to scatter from the higher activity nearby pot. Therefore the deadtime correction appears to be appropriately corrected for. However,

the PV correction appears to be introducing errors of up to 10.2% in SPECT activity, with scatter adding a further error or ~10% when a high uptake area was placed nearby.

Using the planned time points for tumour dosimetry of 6, 21, 45 and 164h with biokinetic model activities gave a time integrated activity of 1967±268 MBq.h. The true time integrated activity value of 1968MBq.h was 0.04% higher and well within experimental errors. This indicates that for the biokinetic model used the planned time points should adequately sample the model. Using measured SPECT activity data for all measured time points, compared to using only the 4, 15, 45 and 164h points which best matched the planned method, gave a difference in time integrated activity which was 1.0% higher, which is within the expected experimental uncertainty. This suggest that the planned time points for tumour dosimetry scanning should be adequate for the biokinetic model used, however further investigation could be performed with other biokinetic models and with statistical noise added.

The S-factor calculated by NPL for the 13ml sphere was calculated to be 3.3% higher for a 13ml sphere using the local model and 3.2 to 3.9% higher using the mean VOI sizes. However personal communication with Ana Denis-Bacelar from NPL suggested that for the Monte Carlo model the number of bins defined and whether it is sampled from a continuous distribution or from a histogram can make a 5% difference to the S-factor, based on unpublished work. For comparison the research tool IDAC Dose 2.1 gave S-factors for a 13cm^3 sphere of 8.7962mGy/MBq and 9.1366mGy/MBq for thyroid (1.04g/cm^3) and water (0.998g/cm^3) respectively [145], [146]. These values are 5% to 1.3% lower than the planned model. The research tool MIRDcalc (MIRD, version 1.0.0.0) gave an S-factor of 8.73mGy/MBq for a 13ml soft tissue tumour, 5.7% lower than the planned model. Therefore the S-factor calculated using the local method appears to be within expected uncertainties. The sphere VOI was outlined based on the CT and showed close agreement with the true volume of 13ml, however it is expected that for patient tumour it will be difficult to differentiate the tumour from normal tissue based on the CT. Therefore a hybrid model using the CT and SPECT would be required and would likely lead to much higher volume uncertainties due to the poorer SPECT resolution [17].

The dose calculated with the model activity data at RSCH planned time points was 3.2% higher than that calculated by the validation model, with the primary cause for the difference seen being due to the different method of performing the S-factor calculation. The dose calculated was 13.0% higher using the measured SPECT data with the planned

local scan time points. The primary reason for this difference was due to the time integrated activity which was 8.7% higher than the NPL data, with the different method of calculating the S-factor causing a difference of 3.9%. Within literature errors of up to 20% have been reported for small organs [23], so the current results are within the expected range. Therefore the tumour dosimetry technique has been validated and the partial volume correction method has been identified as an area to investigate if further improvements can be made.

With this validation technique SPECT sphere measurements were performed for 10 time points within the biokinetic model, however the errors in SPECT activity estimation were not seen to change with activity. Filling the 6 spheres was time consuming and required over 3 hours gamma camera time, which is likely to be an issue for clinical sites. Therefore it is suggested that instead a single sphere should be scanned as a test of the sensitivity and PV calibrations. Multiple consecutive acquisitions could then be performed to test repeatability and allow uncertainties to be better estimated. To test the model fit calculations, it is instead suggested that simulated time point and activity data should be provided. This which would allow different biokinetic models and noise levels to be tested.

The model sphere activities were low, so an object which produced high deadtime was added to allow the deadtime model to be tested. If a single sphere was used it is suggested that this should initially be at a sufficiently high activity to allow the deadtime model to be tested. Two acquisition sessions could then be performed, one with a high sphere activity to test the deadtime and one following decay to an activity where the deadtime is likely to be low. However this would require thorough leak testing of the spheres and confirmation that the activity would not plate out. Alternatively, two spheres could be filled, with one containing a low activity and another with a high activity, which would also allow for scanning within the same session.

Issues were found with the ability to precisely fill spheres using available equipment at the hospital site and stock vials were sent to NPL to measure the activity concentration. However, the residual activity in the syringes still needed to be assayed at the hospital site. This introduced additional uncertainty which was not related to the planned local dosimetry process, therefore it is suggested that the metrology centre could instead send more accurately filled spheres to the test site.

For this method only uniformly filled spheres were measured for mean dose calculations, however this would not sufficiently challenge the systems for sites with voxel dosimetry capabilities. It will also not test the partial volume errors that would be observed with non-spherical objects. Therefore the addition of a heterogeneous tumour shaped phantom is suggested. This could also scanned together with the sphere phantom to assess the impact of scatter on image quantification.

The proposed method of validation requires the manufacture and distribution of 3D printed phantoms, accurate phantom filling and gamma camera scan time. The use of simulated or experimental data distributed by the site performing the validation could allow test sites to participate more easily. This will allow the general dosimetry methodology to be assessed and can be used for procedure standardisation [61], [147]. For the MRTDosimetry project experimental and simulated data for a system were used representing a Lu-177 DOTATAE therapy patient torso [61]. This enabled the results from a range of dosimetry systems to be compared. However for assessment of the sites gamma camera calibrations performed, the distributed data must be representative of the test sites equipment. The DosiTest project is aiming to produce Monte Carlo simulated Lu-177 DOTATATE patient images, for a range of gamma camera systems [147]–[149]. However this requires simulation of full range of systems in clinical use and may not be fully representative of the sites equipment, for example a 20% difference in sensitivity was reported for one Monte Carlo model produced [148]. Therefore the method proposed in this work represents a practical procedure for validating both the tumour dosimetry process and gamma camera calibrations.

7. Summary and Conclusions

This thesis has investigated methods for performing dosimetry in patients with thyroid carcinoma undergoing I-131 therapy which can be implemented in a standard hospital setting. Different whole body measurement techniques have been investigated using patient data to determine the impact on whole body residence time calculations for bone marrow dosimetry. Different calibrations have been investigated and performed for the RSCH GE Optima SPECT/CT system and Wizard gamma counters. A plan for practically performing tumour and bone marrow dosimetry within a standard hospital setting has been produced. The tumour dosimetry method has also been validated through collaboration with the National Physical Laboratory.

A literature review was performed in Chapter 2 which identified a number of areas for further investigation regarding whole body residence time estimation using probes, including impact of conjugate whole body probe measurements compared to anterior only; reduced numbers of background measurements; the impact of a late measurement time point and use of gamma camera imaging for this measurement. Different methods given in literature for performing deadtime, sensitivity and PVC calibrations for SPECT tumour dosimetry were also reviewed and practical methods determined, with a need for a comparison of these methods being identified. An investigation into practical methods of performing whole body retention measurements was performed and details are given in Chapter 3. This found Radhound SS404AL monitors, NaI(Tl) hand held probes commonly found within Nuclear Medicine departments for contamination monitoring, had sufficient range to cover the I-131 patient activities required for whole body retention monitoring over the 7 days post treatment. Radhound linearity testing using I-131 capsules within a thyroid neck phantom was performed and the non-paralysable default deadtime set of 10μs was found to not be sufficient for I-131. Therefore an additional non-paralysable deadtime correction of 9.89μs was found to be required. While the deadtime will be slightly different for every probe, these methods can be used to determine the deadtime, either through retrospective correction or through changing the deadtime correction on the system. A method of performing reproducible whole body retention measurements in therapy rooms and the imaging department was determined using a probe positioned on a trolley and position marks on the floors and walls.

The impact of using geometric mean compared to anterior whole body probe measurements was investigated using patient data. It was found that while the anterior count rates were typically higher, the difference between the anterior and geometric mean measurements remained similar across multiple time points. Statistically significant difference in whole body residence times using both methods was also not seen. However differences of up to 6% were seen in some patients so it was concluded that despite the extra time required for conjugate view measurements these should be used where possible and otherwise an uncertainty of 6% should be accounted for. This gives evidence for the use of conjugate view imaging recommended in guidelines [20], [21].

The impact of therapy room background on patient whole body residence time was investigated and it was found that the therapy room background correction methods investigated made a small difference to residence time (-2.2 to 3.8%). This was thought to be because the count rate from the patient prior to discharge is typically substantially

above background. However the work did highlight the need to give instructions to ensure background is as low as possible, such as for where worn clothes should be placed. Background measurements were not taken prior to every patient measurement, so the fluctuations in background over time could not be assessed. However, this work suggest that while ideally background measurements would be performed with every patient measurement, if this is not practical to do so for dose or contamination reasons then it is likely to only lead to an uncertainty of 3.8%.

The use of a gamma camera for a late time point whole body retention measurement in conjunction with whole body probe measurements was investigated due to potential difficulties in performing probe measurements once the patient has been discharged. However it was found this would produce significant errors and so was not feasible. Therefore matched systems would need to be used for all whole body retention measurements, either by using probes which can be moved or using cross-calibrated systems with measurements on both systems prior to discharge, as suggested within IDUG guidance [57]. The impact of late time point measurements at 7 days post therapy was investigated and was found to make up to a 6% increase in residence time. Only 8 patients could be included in this analysis and all were high risk patients receiving a 3.7GBq ablation administration. However, this work does indicate that while ideally late time point measurements would be done, if this is not possible for logistical reasons then the underestimate with early measurements could be accounted for to give a worst case. However further work with more patients and different cohorts should be performed to investigate this further.

Therefore this work suggests that if anterior only whole body measurements are performed instead of geometric mean this could add an error of -6.3% to 5.0% (-0.5% median) to the residence time, variation in inpatient background could give an error of -2.2% to 3.8% (0% median) and not performing an additional late time point at 7d post administration could add an error of -5.9% to -0.5% (-2.2% median). The largest area of error appears to be the use of anterior only measurements instead of geometric mean, therefore geometric mean measurements should be used where possible. The radionuclide calibrator accuracy uncertainty of 5%, will cause 5% uncertainties in the administered activity and sample counter sensitivity, giving an uncertainty of ~7% to the blood or bone marrow dose. A summary of the errors affecting the bone marrow and blood dosimetry calculation is given in

Table 11.

Table 11. Summary of key errors and uncertainties determined for dose calculations.

Relevant dose calculation	Parameter	Comment	Error/uncertainty
Blood/bone marrow	Whole body residence time	Anterior only measurements error	-6.3% to 5.0% (-0.5% median
		Variation in inpatient background error	-2.2% to 3.8% (0% median)
		Error if additional late time point at 7d post administration not performed	-5.9% to -0.5% (-2.2% median)
	Administered activity	Calibrator accuracy uncertainty	±5%
	Sample Counter Sensitivity	Calibrator accuracy uncertainty main contribution	±5%
	Blood/bone marrow dose	Calibrator accuracy uncertainty contribution	~±7%
Tumour, general	SPECT deadtime	Non-paralysable TEW corrected fast mode deadtime uncertainty	1.2% (6.91±0.08μs)
	SPECT sensitivity	MRTDosimetry method uncertainty	4.0% (22.3±0.9cps/MBq)
	Partial volume correction factor	Fit parameters, based on all spheres data and no constraints	α = 0.72±0.02 β = 0.74±0.04 γ = 16±2
		Recovery curve fit errors, ΔR%	-3.8%-23.7%
	S-factor	Fit parameters	a = 111.4±0.2 b = 0.9697±0.0004
Tumour, 13ml sphere NPL validation	Time integrated activity	Uncertainty, planned method	18%
	S-factor	Uncertainty, planned method	18%
	Dose	Uncertainty, planned method	11%

Deadtime, sensitivity and partial volume effect calibrations were performed and details are given in Chapter 4. GE “fast” counting mode was previously found to be required for early dosimetry imaging as part of the site set up for the SEL-I-METRY trial, where the photopeak window deadtime was measured [53]. Further investigation characterising fast mode through comparison with normal mode data was performed in this work. This found that while the deadtime with fast mode was substantially reduced compared normal mode, the scatter windows did not show the steady increase in deadtime factor seen with normal mode. Instead at 406MBq the lower window deadtime factor appeared

to stabilise, with the upper window deadtime factor increasing at a slower rate than previously seen. TEW scatter correction was planned and the deadtime factor seen with each of the scatter windows in fast mode differed from that seen with the photopeak window. Therefore, it was determined that deadtime correction based on the TEW corrected images should be used. This was found to be 6.91±0.08μs with a non-paralysable model and 6.2±0.04μs with a paralysable model, with both models found to give good agreement with the measured 20-2800MBq data.

SPECT sensitivity measurements were performed using fast and normal mode with a low deadtime cylindrical phantom, which found that normal mode gave a higher sensitivity compared to fast mode. Activity recovery measurements were also performed using fast and normal mode using spheres with 0.5 to 200ml volumes and a 6.8L cylindrical phantom, which found that normal mode gave slightly higher activity recovery. It was concluded that GE fast mode appears to behave differently from normal mode, affecting sensitivity and activity recovery even at low count rates. Therefore, mode specific calibrations should be used and switching between modes is not recommended for dosimetry purposes. The SEL-I-METRY analysis of the fast mode photopeak deadtime data found a deadtime of 3.15±0.03μs [53] while the analysis in this work gave 3.62±0.03 μs. This is believed to be due to the different method of calculating the true count rate, as the SEL-I-METRY method may be affected by deadtime in their calibration. While the difference is small this highlights the impact of different analysis methods and need for standardisation for dose comparisons in clinical trials.

SPECT sensitivity measurements were performed using a uniformly filled Jaszczak phantom and analysed using the different VOI sizes suggested in the EANM mIBG dosimetry guidelines and MRTDosimetry work [16], [61]. This found no significant difference between the two methods, therefore it was concluded that either method could be used. However the sensitivity results using the total SPECT counts and with the total counts from planar imaging of a disc source, as recommended by GE was found to give 16% higher results for normal mode and so the total counts method was not recommended.

Different methods of partial volume correction calibrations were investigated in Chapter 4.6 using 0.5 to 200ml spheres, 38mm long cylinders with volumes of 1.7 to 110ml and a uniformly filled 6.8L Jaszczak phantom. OSEM reconstruction with 60 iterations, 10 subsets, TEW and AC correction and no filter was used. This found that including a

uniformly filled Jaszczak phantom or setting the fit plateau to unity resulted in high percentage errors for the RCs for volumes less than 16ml, the typical sizes of thyroid tumours. Therefore these methods cannot be recommended for I-131 NaI thyroid cancer therapies based on this work. Using the 0.5 to 16 ml Jaszczak spheres resulted in high errors for larger object sizes, however if thyroid remnant and metastases are the only volumes of interest then these objects could be used. Therefore as these Jaszczak phantoms are widely available in a standard clinical setting this could remove the requirement for specialist additional phantoms with volumes up to 113ml (60mm diameter) given in guidelines [16]. However larger volumes should be imaged wherever possible to allow assessment of larger objects. The impact of scanning the Jaszczak spheres together within one phantom rather than individually was investigated and a small increase in activity recovery was seen with the spheres imaged together, likely due to scatter from neighbouring spheres. However this increase was within experimental uncertainties. Therefore it was concluded that while ideally the spheres would be imaged separately, they could be imaged together if required.

A procedure for practical implementation of dosimetry was determined based on the literature review and experimental work detailed within this thesis and is given in Chapter 5. This procedure involved SPECT/CT scanning, blood samples and whole body retention measurements at approximately 6, 20, 44 and 164 hour post I-131 administration. It also suggested additional blood and whole body measurements at 2 hours and whole body measurements at the start and end of the working day while the patients is an inpatient. Anterior and posterior geometric mean whole body measurements at 3m from the patient using a Radhound on a trolley for reproducible positioning were planned, with whole body measurements calculated from geometric mean net counts. Three 1ml blood were samples suggested, with measurements on a gamma counter with known I-131 sensitivity 7 days post therapy to reduce deadtime. Iterative calculation of blood and whole body residence times was suggested using bi-exponential clearance models and curve stripping to determine the starting points. EANM equations 7 and 8 were also suggested to calculate the bone marrow and blood dose from the residence times [20], [21].

For tumour dosimetry gamma camera imaging using I-131 fast mode was suggested, with TEW and deadtime correction being performed using in house software, SPECT reconstruction planned using GE Volumetrix software and VOI analysis using Mirada software. It identified that in house software was needed to apply the required

corrections and calculate dose. This software was developed and performed PV correction using the optimal parameters determined in Chapter 4.6, activity calculation using the sensitivity factor determined in Chapter 4.5 and iterative time activity curve fitting assuming mono-exponential uptake and clearance. The software then calculated the time integrated activity from the fit parameters using Equation 37 and S-factors from the mean VOI volume using Equation 35 and fit parameters given in Chapter 4.7. From the time integrated activity and S-factors the dose could then be calculated using Equation 36. A summary of the errors affecting the tumour dosimetry calculation is given in

Table 11.

A method for validation of the tumour dosimetry technique by a national metrology centre was developed. This was performed by imaging 13ml I-131 filled spheres within a water filled Jaszczak phantom, with activities covering the time points for a clinically realistic biokinetic model. This found the dose was overestimated by 13%, primarily due to the SPECT activities which were overestimated by 2.6 to 10.2%, likely due to PVC errors which are known to be high with small volumes [17]. The different method of performing S-factor calculation used by the national metrology centre compared to OLINDA v1.0 contributed a further error of around 3%. Using the planned time points and activities from the biokinetic model was found to give a -0.04% difference in time integrated activity compared to the true result, validating the use of the planned time points and fitting technique for that biokinetic model. Based on the site experience of using the validation technique, further developments were suggested to enable the validation process to be more widely used. Imaging a sphere and clinically realistic heterogonous tumour phantom with a high deadtime activity and then later with a low deadtime activity were suggested to test the deadtime, sensitivity and PVC corrections. The provision of simulated activity data using different biokinetic models and noise to test the fitting method and dose calculation was also suggested.

The uncertainty for tumour dosimetry will depend of the size of the object due to the partial volume effect, with larger volumes having a smaller fractional uncertainty. For the 13ml sphere validation the planned method dose had an 11% uncertainty, with an 18% uncertainty in time integrated activity and 18% uncertainty in S-factor. The SPECT sensitivity had a 4% uncertainty, therefore the uncertainties are primarily due to the small object volume causing difficulties with outlining, voxel fractionation and counts spill out.

Therefore, smaller voxel sizes could be considered along with methods of improving image resolution. A summary of the key areas of uncertainty in the 13ml tumour dose calculation is given in

Table 11.

8. Future Work

For this work a method has been developed for I-131 NaI thyroid cancer therapy dosimetry, calibrations have been performed for a single system and spreadsheets have been produced for analysis, however dosimetry was not able to be implemented for patients within this project. Therefore future work should focus on the implementation of this dosimetry method for patients, including a comparison of errors introduced with the hybrid SPECT/CT-planar method compared to SPECT/CT. The methodology used could be implemented for other sites performing the therapies and for different systems. Global calibration factors could also be produced for similar systems, reducing the need for extensive set-up testing and allowing harmonisation. The methodology could also be adapted for other forms of molecular radiotherapy such as Lu-177 DOTATATE. The dosimetry validation method suggested should be tested and if successful could be used to provide assurance and harmonisation in dosimetry.

Large scale clinical trials are required to investigate the correlation between patient dose, morbidity and outcome for molecular radiotherapy. This would provide clinical data regarding dosimetry based administered activities, so treatments can be optimised and patient outcomes improved. Investigation also should be performed to determine if cohort data can be used for calculating doses for a single time point for centres that are not able to perform full dosimetry. This is under investigation for ablation patients with no distant metastases as part of the Horizon 2020 MEDIRAD project [54].

For this work deadtime correction was performed for each projection, in line with MIRD SPECT guidelines [23], [56], however this required the development of in house software as deadtime correction was not available on the GE Xeleris system. Projection based deadtime correction has the advantage of accounting for the impact high uptake areas in the periphery of the patient (e.g. remnant thyroid) on certain projections. However, this may not be possible to implement for all sites and in some work the deadtime correction is instead applied to the reconstructed SPECT image [53]. Ideally the deadtime correction used would be included in the SPECT reconstruction and this is included in the latest Siemens xSPECT Quant reconstruction [79]. However there is a need for this form of

correction to become available for all commercial SPECT reconstruction systems. In the interim further work could be performed to investigate the impact of different methods of applying deadtime correction.

Commercial software for dosimetry was found to be prohibitively expensive for I-131 NaI therapies given the level of NHS reimbursement for these therapies, therefore costing of this software and reimbursement needs to be improved. Commercial dosimetry software was also found to not include many of the corrections required for dosimetry such as deadtime or partial volume corrections, therefore further work is required to develop this software. Voxel based dosimetry was not investigated as part of this work and further investigation is required into the impact of voxel based dosimetry compared to mean organ doses and S-factors. For voxel based dosimetry further work would be required to investigate the optimal SPECT reconstruction parameters.

Large errors in activity recovery were found with small volumes of I-131 using volume based PVC correction with calibrations performed using spheres. Therefore further investigation is required into methods of PVC correction, ideally with software that can be used clinically within a standard hospital setting and covering a wide range of object sizes. Methods of correcting for the impact of nearby areas with radionuclide uptake could also be investigated. The large error seen could potentially limit the utility of dosimetry for small volume tumours in clinical practice and for determining dose-response models. The dosimetry accuracy with more patient realistic phantoms also requires further investigation. The resolution of the system also resulted in low activity recovery for small volumes, therefore the use of CDR modelling could be investigated using different available systems.

GE fast counting mode has previously been found to be required to reduce deadtime for post therapy imaging in I-131 patients [53] and this work found that the different energy windows used for TEW correction appeared to experience different deadtime. Therefore further work is suggested to further characterise fast mode through looking at the impact over wider range of the energy spectrum. Significant difference in sensitivity and activity recovery between fast and normal mode were also seen in this work and therefore further investigation into the impact on clinical imaging is suggested.

SPECT calibrations were performed with 120 projections, however future work could investigate the impact of reducing this e.g. to the 72 or 60 projections used for the SEL-I-

METRY and MEDIRAD trials respectively [53], [72]. This would have the advantage of reducing scan time or allowing a larger number of counts per projection.

Late time point measurements were found to be beneficial for bone marrow dosimetry measurements which can be logistically challenging. Further work could investigate the impact of measurements at different late time points and with a larger cohort of patients. To assist with performing late time point measurements, methods which could be taken by the patient at home such as finger prick blood samples, TLDs or mobile phone Geiger attachments could be investigated.

There is still a large amount of work that can be performed to improve dosimetry methodology and enable dosimetry based treatment planning and post therapy dose verification. However, this work provides a practical method for implementing dosimetry. Once dosimetry can be more widely implemented it is likely to become better optimised in the same way that has been seen for external beam radiotherapy, enabling better patient outcomes.

9. References

[1] F. A. Verburg *et al.*, "The 'reset button' revisited: why high activity 131I therapy of advanced differentiated thyroid cancer after dosimetry is advantageous for patients," *Eur. J. Nucl. Med. Mol. Imaging*, vol. 44, no. 6, pp. 915–917, 2017, doi: 10.1007/s00259-017-3649-9.

[2] D. R. McGowan and M. J. Guy, "Time to demand dosimetry for molecular radiotherapy?," *Br. J. Radiol.*, vol. 88, no. 1047, pp. 3–5, 2015, doi: 10.1259/bjr.20140720.

[3] Cancer Research UK, "Thyroid cancer incidence statistics," 2014. http://www.cancerresearchuk.org/health-professional/cancer-statistics/statistics-by-cancer-type/thyroid-cancer (accessed Jan. 12, 2018).

[4] S. I. Sherman, "Thyroid carcinoma," *Lancet*, vol. 361, pp. 501–511, 2003, doi: 10.1016/s0140-6736(03)12488-9.

[5] P. Perros *et al.*, "Guidelines for the management of thyroid cancer," *Clin. Endocrinol. (Oxf).*, vol. 81, no. SUPPL. 1, pp. 1–136, 2014, doi: 10.1111/cen.12515.

[6] A. J. Craig, B. Rojas, J. L. Wevrett, E. Hamer, A. Fenwick, and R. Gregory, "IPEM topical report: Current molecular radiotherapy service provision and guidance on the implications of setting up a dosimetry service," *Phys. Med. Biol.*, vol. 65, no. 24, 2020, doi: 10.1088/1361-6560/abc707.

[7] D. V. Becker and C. T. Sawin, "Radioiodine and thyroid disease: The beginning," *Semin. Nucl. Med.*, vol. 26, no. 3, pp. 155–164, 1996, doi: 10.1016/S0001-2998(96)80020-1.

[8] P. M. Yen, "Physiological and molecular basis of thyroid hormone action.," *Physiol. Rev.*, vol. 81, no. 3, pp. 1097–1142, 2001, doi: 11427693.

[9] G. W. C. Kaye and T. H. Laby, *Tables of physical and chemical constants*, 16th ed. Horlow, UK: Longman, 1995.

[10] B. Rojas, D. R. McGowan, M. J. Guy, J. Tipping, M. Aldridge, and J. Gear, "Eighty per cent more patients in 10 years of UK molecular radiotherapy: Internal Dosimetry Users Group survey results from 2007 to 2017," *Nucl. Med. Commun.*, vol. 40, no. 7, pp. 657–661, 2019, doi: 10.1097/MNM.0000000000001020.

[11] C. Stokke *et al.*, "Dosimetry-based treatment planning for molecular radiotherapy: a summary of the 2017 report from the Internal Dosimetry Task Force," *EJNMMI Phys.*, vol. 4, no. 1, p. 27, 2017, doi: 10.1186/s40658-017-0194-3.

[12] A. Miranti, A. Giostra, E. Richetta, E. Gino, R. E. Pellerito, and M. Stasi, "Comparison of mathematical models for red marrow and blood absorbed dose estimation in the radioiodine treatment of advanced differentiated thyroid carcinoma," *Phys. Med. Biol.*, vol. 60, no. 3, pp. 1141–1157, 2015, doi: 10.1088/0031-9155/60/3/1141.

[13] P. Mínguez, G. Flux, J. Genollá, A. Delgado, E. Rodeno, and K. Sjögreen Gleisner, "Whole-remnant and maximum-voxel SPECT/CT dosimetry in 131 I-NaI treatments of differentiated thyroid cancer," *Med. Phys.*, vol. 43, no. 10, pp. 5279–5287, 2016, doi: 10.1118/1.4961742.

[14] Council of the European Union, "Council Directive 2013/59/EURATOM of 5 December 2013 laying down basic safety standards for protection against the dangers arising from exposure to ionising radiation, and repealing Directives

89/618/Euratom, 90/641/Euratom, 96/29/Euratom, 97/43/Euratom a," *Off. J. Eur. Union No. L*, vol. L13, no. 57, pp. 1–73, 2014.

[15] The Stationary Office, *The Ionising Radiation (Medical Exposure) Regulations 2017*. UK, 2018.

[16] J. Gear *et al.*, "EANM Dosimetry Committee series on standard operational procedures for internal dosimetry for 131I mIBG treatment of neuroendocrine tumours," *EJNMMI Phys.*, vol. 7, no. 1, 2020, doi: 10.1186/s40658-020-0282-7.

[17] J. I. Gear *et al.*, "EANM practical guidance on uncertainty analysis for molecular radiotherapy absorbed dose calculations," *Eur. J. Nucl. Med. Mol. Imaging*, vol. 45, no. 13, pp. 2456–2474, 2018, doi: 10.1007/s00259-018-4136-7.

[18] H. Hänscheid *et al.*, "EANM dosimetry committee series on standard operational procedures for pre-therapeutic dosimetry II. Dosimetry prior to radioiodine therapy of benign thyroid diseases," *Eur. J. Nucl. Med. Mol. Imaging*, vol. 40, no. 7, pp. 1126–1134, 2013, doi: 10.1007/s00259-013-2387-x.

[19] M. Lassmann, C. Chiesa, G. Flux, and M. Bardies, "EANM Dosimetry Committee guidance document: Good practice of clinical dosimetry reporting," *Eur. J. Nucl. Med. Mol. Imaging*, vol. 38, no. 1, pp. 192–200, 2011, doi: 10.1007/s00259-010-1549-3.

[20] C. Hindorf, G. Glatting, C. Chiesa, O. Lindén, and G. Flux, "EANM dosimetry committee guidelines for bone marrow and whole-body dosimetry," *Eur. J. Nucl. Med. Mol. Imaging*, vol. 37, no. 6, pp. 1238–1250, 2010, doi: 10.1007/s00259-010-1422-4.

[21] M. Lassmann, H. Hänscheid, C. Chiesa, C. Hindorf, and G. Flux, "EANM Dosimetry Committee series on standard operational procedures for pre-therapeutic dosimetry I: blood and bone marrow dosimetry in differentiated thyroid cancer therapy," *Eur. J. Nucl. Med. Mol. Imaging*, vol. 35, pp. 1405–1412, 2008, doi: 10.1007/s00259-008-0761-x.

[22] M. Ljungberg, A. Celler, M. W. Konijnenberg, K. F. Eckerman, Y. K. Dewaraja, and K. Sjögreen-Gleisner, "MIRD pamphlet no. 26: Joint EANM/MIRD guidelines for quantitative 177Lu SPECT applied for dosimetry of radiopharmaceutical therapy," *J. Nucl. Med.*, vol. 57, no. 1, pp. 151–162, 2016, doi: 10.2967/jnumed.115.159012.

[23] Y. K. Dewaraja *et al.*, "MIRD Pamphlet No. 24: Guidelines for quantitative 131I SPECT in dosimetry applications," *J. Nucl. Med.*, vol. 54, no. 12, pp. 2182–2188, 2013, doi: 10.2967/jnumed.113.122390.

[24] EANM Internal Dosimetry Task Force, "Internal Dosimetry Task Force report on treatment planning for molecular radiotherapy: potential and prospects," 2017.

[25] W. E. Bolch, K. F. Eckerman, G. Sgouros, and S. R. Thomas, "MIRD pamphlet No. 21: a generalized schema for radiopharmaceutical dosimetry--standardization of nomenclature.," *J. Nucl. Med.*, vol. 50, no. 21, pp. 477–484, 2009, doi: 10.2967/jnumed.108.056036.

[26] M. G. Stabin, R. B. Sparks, and E. Crowe, "OLINDA/EXM: The Second-Generation Personal Computer Software for Internal Dose Assessment in Nuclear Medicine," *J Nucl Med*, vol. 46, no. 6, pp. 1023–1027, 2005, doi: 46/6/1023 [pii].

[27] H. Zaidi and X. G. Xu, "Computational anthropomorphic models of the human anatomy: the path to realistic Monte Carlo modeling in radiological sciences.," *Annu. Rev. Biomed. Eng.*, vol. 9, pp. 471–500, 2007, doi:

10.1146/annurev.bioeng.9.060906.151934.

[28] M. G. Stabin *et al.*, "Mathematical models and specific absorbed fractions of photon energy in the nonpregnant adult female and at the end of each trimester of pregnancy," Oak Ridge, Tennassee, 1995. doi: 10.2172/91944.

[29] L. Cheng, R. F. Hobbs, P. W. Segars, G. Sgouros, and E. C. Frey, "Improved dose-volume histogram estimates for radiopharmaceutical therapy by optimizing quantitative SPECT reconstruction parameters," *Phys. Med. Biol.*, vol. 58, no. 11, pp. 3631–3647, 2013, doi: 10.1007/s10955-011-0269-9.Quantifying.

[30] E. T. Hippeläinen, M. J. Tenhunen, H. O. Mäenpää, J. J. Heikkonen, and A. O. Sohlberg, "Dosimetry software Hermes Internal Radiation Dosimetry: From quantitative image reconstruction to voxel-level absorbed dose distribution," *Nucl. Med. Commun.*, vol. 38, no. 5, pp. 357–365, 2017, doi: 10.1097/MNM.0000000000000662.

[31] L. Santoro *et al.*, "Clinical implementation of PLANET® Dose for dosimetric assessment after [177Lu]Lu-DOTA-TATE: comparison with Dosimetry Toolkit® and OLINDA/EXM® V1.0," *EJNMMI Res.*, vol. 11, no. 1, pp. 1–17, 2021, doi: 10.1186/s13550-020-00737-8.

[32] R. S. Benua, N. R. Cicale, M. Sonenberg, and R. W. Rawson, "The relation of radioiodine dosimetry to results and complications in the treatment of metastatic thyroid cancer," *Am. J. Roentgenol. Radium Ther. Nucl. Med.*, vol. 87, pp. 171–82, 1962.

[33] R. Wierts *et al.*, "Dose-response relationship in differentiated thyroid cancer patients undergoing radioiodine treatment assessed by means of 124I PET/CT," *J. Nucl. Med.*, vol. 57, no. 7, pp. 1027–1032, 2016, doi: 10.2967/jnumed.115.168799.

[34] G. D. Flux *et al.*, "A dose-effect correlation for radioiodine ablation in differentiated thyroid cancer," *Eur. J. Nucl. Med. Mol. Imaging*, vol. 37, no. 2, pp. 270–275, 2010, doi: 10.1007/s00259-009-1261-3.

[35] M. Lassmann, C. Reiners, and M. Luster, "Dosimetry and thyroid cancer: The individual dosage of radioiodine," *Endocr. Relat. Cancer*, vol. 17, no. 3, pp. 161–172, 2010, doi: 10.1677/ERC-10-0071.

[36] M. Ljungberg and P. H. Pretorius, "SPECT/CT: an update on technological developments and clinical applications," *Br. J. Radiol.*, vol. 91, no. 1081, 2018, doi: 10.1259/bjr.20160402.

[37] T. Ito *et al.*, "Experimental evaluation of the GE NM/CT 870 CZT clinical SPECT system equipped with WEHR and MEHRS collimator," *J. Appl. Clin. Med. Phys.*, vol. 22, no. 2, pp. 165–177, 2021, doi: 10.1002/acm2.13158.

[38] P. P. Bruyant, "Analytic and iterative reconstruction algorithms in SPECT," *J. Nucl. Med.*, vol. 43, no. 10, pp. 1343–1359, 2002.

[39] S. Cherry, J. Sorenson, and M. Phelphs, "Chapter 10: Pulse-Height Spectrometry," in *Physics in Nucelar Medicine*, Third., Philadelphia: Elsevier, 2003, pp. 157–160.

[40] F. Barrack, J. Scuffham, and S. McQuaid, "Septal penetration correction in I-131 imaging following thyroid cancer treatment," *Phys. Med. Biol.*, vol. 63, no. 7, 2018, doi: 10.1088/1361-6560/aab13a.

[41] P. Ritt, J. Sanders, and T. Kuwert, "SPECT/CT technology," *Clin. Transl. Imaging*, vol. 2, no. 6, pp. 445–457, 2014, doi: 10.1007/s40336-014-0086-7.

[42] K. Erlandsson, I. Buvat, P. H. Pretorius, B. a Thomas, and B. F. Hutton, “A review of partial volume correction techniques for emission tomography and their applications in neurology, cardiology and oncology,” *Phys. Med. Biol.*, vol. 57, no. 21, pp. R119–R159, 2012, doi: 10.1088/0031-9155/57/21/R119.

[43] M. Soret, S. L. Bacharach, and I. Buvat, “Partial-volume effect in PET tumor imaging,” *J. Nucl. Med.*, vol. 48, no. 6, pp. 932–945, 2007, doi: 10.2967/jnumed.106.035774.

[44] J. Prekeges, *Nuclear medicine instrumentation*, Second Edi. Burlington, MA: Jones and Bartlett Learning, 2013.

[45] S. Cherry, J. Sorenson, and M. Phelphs, “Chapter 11: Problems in Radiation Detection and Management,” in *Physics in Nucelar Medicine*, Third., Philadelphia: Elsevier, 2003, p. 179.

[46] ARSAC, “Notes for guidance on the clinical administration of radiopharmaceuticals and use of sealed radioactive sources. Administration of Radioactive Substances Advisory Committee.,” 2020.

[47] M. Konijnenberg *et al.*, “EANM position paper on article 56 of the Council Directive 2013/59/Euratom (basic safety standards) for nuclear medicine therapy,” *Eur. J. Nucl. Med. Mol. Imaging*, vol. 48, no. 1, pp. 67–72, 2021, doi: 10.1007/s00259-020-05038-9.

[48] J. Gear *et al.*, “The Internal Dosimetry User Group Position statement,” 2021. https://www.idug.org.uk/idug-position-statement-2021/ (accessed May 23, 2021).

[49] ARSAC, “Notes for guidance on the clinical administration of radiopharmaceuticals and use of sealed radioactive sources,” Didcot, 2019.

[50] General Electric Healthcare, “Summary of Product Characteristics: THERACAP131 37 MBq-5.55 GBq capsules, hard.” https://products.mhra.gov.uk/ (accessed May 25, 2021).

[51] Committee for Medicinal Products for Human Use, “Guideline on core SmPC and Package Leaflet for sodium iodide (131I) for therapeutic use,” 2016. https://www.ema.europa.eu/en/core-smpc-package-leaflet-sodium-iodide-131-i-therapeutic-use (accessed May 25, 2021).

[52] J. Wadsley, R. Gregory, and G. Flux, “SELIMETRY-a multicentre I-131 dosimetry trial: a clinical perspective,” *Br. J. Radiol.*, vol. 90, 2017, doi: 20160637.

[53] R. A. Gregory *et al.*, “Standardised quantitative radioiodine SPECT/CT Imaging for multicentre dosimetry trials in molecular radiotherapy,” *Phys. Med. Biol.*, vol. 64, no. 24, 2019, doi: 10.1088/1361-6560/ab5b6c.

[54] MEDIRAD, “MEDIRAD Work Packages.” http://www.medirad-project.eu/work-packages (accessed Jun. 05, 2021).

[55] B. E. Zimmerman *et al.*, “Multi-centre evaluation of accuracy and reproducibility of planar and SPECT image quantification: An IAEA phantom study,” *Med. Phys.*, vol. 27, no. 2, pp. 98–112, 2017, doi: 10.1016/j.physbeh.2017.03.040.

[56] Y. K. Dewaraja *et al.*, “MIRD Pamphlet No. 23: Quantitative SPECT for patient-Specific 3-dimensional dosimetry in internal radionuclide therapy,” *J. Nucl. Med.*, vol. 53, no. 8, pp. 1310–1325, 2012, doi: 10.2967/jnumed.111.100123.

[57] Internal Dosimetry Users Group, “Internal Dosimetry Users Group Whole Body Dosimetry Guidance,” 2017. [Online]. Available: http://www.idug.org.uk/wp-

content/uploads/2017/05/IDUGI-131-Whole-Body-Dosimetry-Final.pdf.

[58] J. Willegaignon, M. T. Sapienza, and C. A. Buchpiguel, “Comparison of different dosimetric methods for red marrow absorbed dose calculation in thyroid cancer therapy,” *Radiat. Prot. Dosimetry*, vol. 149, no. 2, pp. 138–146, 2012.

[59] G. Flux *et al.*, “MEDIRAD Deliverable 3.1: Imaging and data collection study protocols,” 2017. [Online]. Available: http://www.medirad-project.eu/storage/app/media/results/MEDIRAD D3.1_Imaging and data collection study protocols.pdf.

[60] F. Leek *et al.*, “MEDIRAD Deliverable 3.2: Report on validation of centres for imaging networks,” 2018.

[61] A. Robinson, “Final Publishable Report: Metrology for clinical implementation of dosimetry in molecular radiotherapy,” 2019. [Online]. Available: http://mrtdosimetry-empir.eu/wp-content/uploads/2019/08/15HLT06_Publishable_Report_M36_Final.pdf.

[62] A. Giostra *et al.*, “Red marrow and blood dosimetry in 131I treatment of metastatic thyroid carcinoma: Pre-treatment versus in-therapy results,” *Phys. Med. Biol.*, vol. 61, no. 11, pp. 4316–4326, 2016, doi: 10.1088/0031-9155/61/11/4316.

[63] E. Piruzan, M. Haghighatafshar, R. Faghihi, and S. M. Entezarmahdi, “Calculation of blood dose in patients treated with 131I using MIRD, imaging, and blood sampling methods,” *Med. (United States)*, vol. 95, no. 11, pp. 1–6, 2016, doi: 10.1097/MD.0000000000003154.

[64] E. C. Frey and B. M. W. Tsui, “Collimator-detector response compensation in SPECT,” in *Quantitative Analysis in Nuclear Medicine Imaging*, H. Zaidi, Ed. New York, NY: Springer, 2006, pp. 141–166.

[65] K. F. Koral, K. R. Zasadny, R. J. Ackermann, and E. P. Ficaro, “Deadtime correction for two multihead Anger cameras in 131I dual-energy-window-acquisition mode,” *Med. Phys.*, vol. 25, no. 1, pp. 85–91, 1998, doi: 10.1118/1.598162.

[66] B. He *et al.*, “Comparison of organ residence time estimation methods for radioimmunotherapy dosimetry and treatment planning-patient studies,” *Med. Phys.*, vol. 36, no. 5, pp. 1595–1601, 2009, doi: 10.1118/1.3100265.

[67] K. Assié, A. Dieudonné, I. Gardin, P. Véra, and I. Buvat, “A preliminary study of quantitative protocols in indium 111 SPECT using computational simulations and phantoms,” *IEEE Trans. Nucl. Sci.*, vol. 57, no. 3 PART 1, pp. 1096–1104, 2010, doi: 10.1109/TNS.2010.2041252.

[68] K. R. Zasadny, K. F. Koral, and F. M. Swailem, “Dead time of an anger camera in dual-energy-window-acquisition mode,” *Med. Phys.*, vol. 20, no. 4, pp. 1115–20, 1993, doi: 10.1118/1.597008.

[69] G. Freedman, T. Kinsela, and A. Dwyer, “A correction method for high-count-rate quantitative radionuclide angiography,” *Radiology*, vol. 104, no. 3, pp. 713–5, 1972, doi: 10.1148/104.3.713.

[70] C. Chiesa *et al.*, “A practical dead time correction method in planar activity quantification for dosimetry during radionuclide therapy,” *Q. J. Nucl. Med. Mol. Imaging*, vol. 53, no. 6, pp. 658–670, 2009.

[71] G. Delpon, L. Ferrer, A. Lisbona, and M. Bardiès, “Correction of count losses due to deadtime on a DST-XLi (SMVi-GE) camera during dosimetric studies in patients

injected with iodine-131," *Phys. Med. Biol.*, vol. 47, no. 7, 2002, doi: 10.1088/0031-9155/47/7/402.

[72] J. Taprogge *et al.*, "Setting up a quantitative SPECT imaging network for a European multi-centre dosimetry study of radioiodine treatment for thyroid cancer as part of the MEDIRAD project," *EJNMMI Phys.*, vol. 7, no. 1, 2020, doi: 10.1186/s40658-020-00332-9.

[73] NEMA, "NEMA NU 1-2007. Performance Measurements of Gamma Cameras." National Electrical Manufacturers Association, 2007.

[74] K. Cranley, R. Millar, and T. K. Bell, "Correction for deadtime losses in a gamma camera/data analysis system.," *Eur. J. Nucl. Med.*, vol. 5, no. 4, pp. 377–382, 1980, doi: 10.1007/BF00445626.

[75] N. Bates, "Uniformity testing of gamma cameras at high count-rates," 2017. http://mrtdosimetry-empir.eu/?p=1248 (accessed Mar. 28, 2018).

[76] M. J. Guy, G. D. Flux, M. A. Flower, R. J. Ott, P. Papavasileiou, and S. J. Chittenden, "Practical scatter-independent gamma camera dead-time correction for iodine-131," *2000 IEEE Nucl. Sci. Symp. Conf. Rec. (Cat. No.00CH37149)*, vol. 14, pp. 18/52-18/56, 2002, doi: 10.1109/nssmic.2000.949229.

[77] M. J. Schipper, K. F. Koral, A. M. Avram, M. S. Kaminski, and Y. K. Dewaraja, "Prediction of therapy tumor-absorbed dose estimates in I-131 radioimmunotherapy using tracer data via a mixed-model fit to time activity," *Cancer Biother. Radiopharm.*, vol. 27, no. 7, pp. 403–411, 2012, doi: 10.1089/cbr.2011.1053.

[78] S. Cherry, J. Sorenson, and M. Phelphs, "Chapter 14: The Gamma Camera: Performance Characteristics," in *Physics in Nucelar Medicine*, Third., Philadelphia: Elsevier, 2003, p. 233.

[79] A. H. Vija *et al.*, "White paper: Accurate, reproducible, and standardized quantification.," Malvern, PA, USA, 2019. [Online]. Available: https://static.healthcare.siemens.com/siemens_hwem-hwem_ssxa_websites-context-root/wcm/idc/groups/public/@global/@imaging/@molecular/documents/download/mda3/ntq3/~edisp/mi-3610_xspect_quant_wp.final-04691530.pdf.

[80] K. Willowson, D. L. Bailey, and C. Baldock, "Quantitative SPECT reconstruction using CT-derived corrections," *Phys. Med. Biol.*, vol. 53, no. 12, pp. 3099–3112, 2008, doi: 10.1088/0031-9155/53/12/002.

[81] L. T. Chang, "A method for attenuation correction in radionuclide computed tomography," *IEEE Trans. Nucl. Sci.*, vol. 25, no. 1, pp. 638–643, 1978, doi: 10.1109/TNS.1978.4329385.

[82] H. Zaidi, *Quantitative Analysis in Nuclear Medicine Imaging*. Singapore: Springer, 2006.

[83] J. A. Siegel *et al.*, "MIRD pamphlet no. 16: Techniques for quantitative radiopharmaceutical biodistribution data acquisition and analysis for use in human radiation dose estimates.," *J. Nucl. Med.*, vol. 40, pp. 37S-61S, 1999, doi: 10025848.

[84] H. Zaidi and K. F. Koral, "Scatter correction strategies in emission tomography," in *Quantitative Analysis in Nuclear Medicine Imaging*, H. Zaidi, Ed. New York, NY: Springer, 2006, pp. 205–235.

[85] R. J. Jaszczak, C. E. Floyd, and R. E. Coleman, “Scatter compensation techniques for spect,” *IEEE Trans. Nucl. Sci.*, vol. 32, no. 1, pp. 786–793, 1985, doi: 10.1109/TNS.1985.4336941.

[86] K. Ogawa, Y. Harata, T. Ichihara, A. Kubo, and S. Hashimoto, “A practical method for position-dependent Compton-scatter correction in single photon emission CT,” *IEEE Trans. Med. Imaging*, vol. 10, no. 3, pp. 408–412, 1991, doi: 10.1109/42.97591.

[87] E. C. Frey and B. M. W. Tsui, “A new method for modeling the spatially-variant, object-dependent scatter response function in SPECT,” *1996 IEEE Nucl. Sci. Symp. Conf. Rec.*, vol. 2, pp. 1082–1086, 1996, doi: 10.1109/NSSMIC.1996.591559.

[88] A. Sohlberg, H. Watabe, and H. Iida, “Acceleration of Monte Carlo-based scatter compensation for cardiac SPECT,” *Phys. Med. Biol.*, vol. 53, no. 14, pp. N277-285, 2008, doi: 10.1088/0031-9155/53/14/N02.

[89] M. A. King, D. J. Devries, T. S. Pan, P. H. Pretorias, and J. A. Case, “An investigation of the filtering of TEW scatter estimates used to compensate for scatter with ordered subset reconstructions,” *IEEE Trans. Nucl. Sci.*, vol. 44, no. 3 PART 2, pp. 1140–1145, 1997, doi: 10.1109/23.596978.

[90] C. A. J. Van Gils, C. Beijst, R. Van Rooij, and H. W. A. M. De Jong, “Impact of reconstruction parameters on quantitative I-131 SPECT,” *Phys. Med. Biol.*, vol. 61, no. 14, pp. 5166–5182, 2016, doi: 10.1088/0031-9155/61/14/5166.

[91] M. Ljungberg, K. Sjögreen, X. Liu, E. Frey, Y. Dewaraja, and S.-E. Strand, “A 3-dimensional absorbed dose calculation method based on quantitative SPECT for radionuclide therapy: evaluation for 131I using Monte Carlo simulation,” *J. Nucl. Med.*, vol. 43, no. 8, pp. 1101–1109, 2002.

[92] A. Seret, D. Nguyen, and C. Bernard, “Quantitative capabilities of four state-of-the-art SPECT-CT cameras,” *EJNMMI Res.*, vol. 2, no. 1, pp. 1–19, 2012, doi: 10.1186/2191-219X-2-45.

[93] F. J. Beekman, H. W. A. M. De Jong, and S. Van Geloven, “Efficient fully 3-D iterative SPECT reconstruction with Monte Carlo-based scatter compensation,” *IEEE Trans. Med. Imaging*, vol. 21, no. 8, pp. 867–877, 2002, doi: 10.1109/TMI.2002.803130.

[94] Y. K. Dewaraja, M. Ljungberg, and J. A. Fessier, “3-D Monte Carlo-based scatter compensation in quantitative I-131 SPECT reconstruction,” *IEEE Trans. Nucl. Sci.*, vol. 53, no. 1, pp. 181–188, 2006, doi: 10.1109/TNS.2005.862956.

[95] W. Woliner-van der Weg *et al.*, “A 3D-printed anatomical pancreas and kidney phantom for optimizing SPECT/CT reconstruction settings in beta cell imaging using 111In-exendin,” *EJNMMI Phys.*, vol. 3, no. 1, 2016, doi: 10.1186/s40658-016-0165-0.

[96] T. S. Kangasmaa, C. Constable, and A. O. Sohlberg, “Evaluation of quantitative 123 i and 131 i SPECT with Monte Carlo-based down-scatter compensation,” *Nucl. Med. Commun.*, vol. 39, no. 12, pp. 1097–1102, 2018, doi: 10.1097/MNM.0000000000000920.

[97] H. McMeekin, “Hermes Educational Series. SUV SPECT and Dosimetry: Standardise and Quantify SPECT,” 2020. https://www.youtube.com/watch?v=n3xPpGKv2C8 (accessed May 24, 2021).

[98] A. Vija, “Introduction to xSPECT* Technology: Evolving Multi-modal SPECT to Become Context-based and Quantitative,” *White Pap.*, pp. 1–28, 2013, [Online].

Available: http://www.healthcare.siemens.com/siemens_hwem-hwem_ssxa_websites-context-root/wcm/idc/groups/public/@global/@imaging/@molecular/documents/download/mdax/ote3/~edisp/xspect_technical_white_paper-00957532.pdf.

[99] D. L. Bailey and K. P. Willowson, "An evidence-based review of quantitative SPECT imaging and potential clinical applications," *J. Nucl. Med.*, vol. 54, no. 1, pp. 83–89, 2013, doi: 10.2967/jnumed.112.111476.

[100] W. Jentzen, L. Freudenberg, E. G. Eising, W. Sonnenschein, J. Knust, and A. Bockisch, "Optimized 124I PET dosimetry protocol for radioiodine therapy of differentiated thyroid cancer," *J. Nucl. Med.*, vol. 49, no. 6, pp. 1017–1023, 2008, doi: 10.2967/jnumed.107.047159.

[101] N. Calvert *et al.*, "Standard Operating Procedure for MRTDosimetry Comparison Exercise – Part 5: Liquid I-131 Sources."

[102] K. F. Koral, J. N. Kritzmaan, V. E. Rogers, R. J. Ackermann, and J. A Fessler, "Optimizing the number of equivalent iterations of 3D OSEM in SPECT reconstruction of I-131 focal activities," *Nucl. Instruments Methods Phys. Res. Sect. A Accel. Spectrometers, Detect. Assoc. Equip.*, vol. 579, no. 1, pp. 326–329, 2007, doi: 10.1016/j.nima.2007.04.070.

[103] B. M. W. Tsui, E. C. Frey, X. Zhao, D. S. Lalush, R. E. Johnston, and W. H. McCartney, "The importance and implementation of accurate 3D compensation methods for quantitative SPECT," *Phys. Med. Biol.*, vol. 39, no. 3, pp. 509–530, 1994, doi: 10.1088/0031-9155/39/3/015.

[104] T. Van den Wyngaert *et al.*, "The EANM practice guidelines for bone scintigraphy," *Eur. J. Nucl. Med. Mol. Imaging*, vol. 43, no. 9, pp. 1723–1738, 2016, doi: 10.1007/s00259-016-3415-4.

[105] K. F. Koral, A. Yendiki, and Y. K. Dewaraja, "Recovery of total I-131 activity within focal volumes using SPECT and 3D OSEM," *Phys. Med. Biol.*, vol. 52, no. 3, pp. 777–790, 2007, doi: 10.1088/0031-9155/52/3/017.

[106] Y. K. Dewaraja, S. J. Wilderman, M. Ljungberg, K. F. Koral, K. Zasadny, and M. S. Kaminiski, "Accurate dosimetry in 131I radionuclide therapy using patient-specific, 3-dimensional methods for SPECT reconstruction and absorbed dose calculation," *J. Nucl. Med.*, vol. 46, no. 5, pp. 840–849, 2005, doi: 46/5/840 [pii].

[107] J. Wevrett, A. Fenwick, J. Scuffham, and A. Nisbet, "Development of a calibration protocol for quantitative imaging for molecular radiotherapy dosimetry," *Radiat. Phys. Chem.*, vol. 140, no. November 2016, pp. 355–360, 2017, doi: 10.1016/j.radphyschem.2017.02.053.

[108] J. Tran-Gia and M. Lassmann, "Calibration and Verification of Quantitative Imaging using SPECT / CT: MRTDosimetry Workshop Teddington 20th & 21st May 2019," 2019. http://mrtdosimetry-empir.eu/wp-content/uploads/2019/06/07_M_Lassmann_and_J_Tran-Gia_Calibration_and_Verification_of_QI.pdf (accessed May 15, 2021).

[109] C. Pettinato *et al.*, "Pretherapeutic dosimetry in patients affected by metastatic thyroid cancer using 124I PET/CT sequential scans for 131I treatment planning," *Clin. Nucl. Med.*, vol. 39, no. 8, pp. 367–374, 2014, doi: 10.1097/RLU.0000000000000490.

[110] S. A. Gulec *et al.*, "124I PET/CT in patients with differentiated thyroid cancer:

Clinical and quantitative image analysis," *Thyroid*, vol. 26, no. 3, pp. 441–448, 2016, doi: 10.1089/thy.2015.0482.

[111] C. C. Huang, Y. H. Lin, S. Kittipayak, Y. S. Hwua, S. Y. Wang, and L. K. Pan, "Biokinetic model of radioiodine I-131 in nine thyroid cancer patients subjected to in-vivo gamma camera scanning: A simplified five-compartmental model," *PLoS One*, vol. 15, no. 5, pp. 1–11, 2020, doi: 10.1371/journal.pone.0232480.

[112] M. G. Stabin, "MIRDOSE: personal computer software for internal dose assessment in nuclear medicine.," *J. Nucl. Med.*, vol. 37, no. 3, pp. 538–546, 1996.

[113] M. Stabin and J. A. Siegel, "Radar dose estimate report: a compendium of radiopharmaceutical dose estimates based on OLINDA/EXM Version 2.0," *J. Nucl. Med.*, vol. 59, no. 1, pp. 154–160, 2018, doi: 10.2967/jnumed.117.196261.

[114] C. J. Lee and P. H. Burgess, *Good Practice Guide No. 14 Issue 2. The Examination, Testing and Calibration of Portable Radiation Protection Instruments*, no. 2. Teddington: National Physical Laboratory, 2014.

[115] H. Hänscheid *et al.*, "EANM Dosimetry Committee Series on Standard Operational Procedures for Pre-Therapeutic Dosimetry II. Dosimetry prior to radioiodine therapy of benign thyroid diseases: Supplement," *Eur. J. Nucl. Med. Mol. Imaging*, vol. 40, no. 7, p. Supplement, 2013.

[116] "Weight of human body parts as percentages of total body weight." http://robslink.com/SAS/democd79/body_part_weights.htm (accessed May 21, 2021).

[117] J. Fleming, N. Williams, J. Skrypniuk, P. Thorley, and M. Rose, *IPEM Report no 85: Radioactive sample counting — principles and practice*. The Institute of Physics and Engineering in Medicine, 2002.

[118] R. Gadd *et al.*, "National Good Practice Guide No. 93: Protocol for Establishing and Maintaining the Calibration of Medical Radionuclide Calibrators and their Quality Control.," no. 93, 2006.

[119] E. Eadie, *IPEM Report 111. Quality Control of Gamma Cameras and Nuclear Medicine Computer Systems*. York: IPEM, 2015.

[120] B. Hutton, "Angular Samplying Necessary for Clinical Spect: Letter to Editor," *J. Nucl. Med.*, vol. 37, no. 10, p. 1916.

[121] R. Gregory, "SEL-I-METRY Site Set-Up Visit Protocol, Version 2," 2015.

[122] T. Sanderson, M. Aldridge, J. Scuffham, and J. Dickson, "Imaging high activities of I-131 using fast mode and dead-time correction," *Nucl. Med. Commun. Conf. Pap.*, vol. 40, no. 4, pp. 393–453, 2019.

[123] A. M. Loening and S. S. Gambhir, "AMIDE: A Free Software Tool for Multimodality Medical Image Analysis," *Mol. Imaging*, vol. 2, no. 3, pp. 131–137, 2003, doi: 10.1162/153535003322556877.

[124] A. M. Morey and D. J. Kadrmas, "Effect of varying number of OSEM subsets on PET lesion detectability," *J. Nucl. Med. Technol.*, vol. 41, no. 4, pp. 268–273, 2013, doi: 10.2967/jnmt.113.131904.

[125] E. O'Mahoney and I. Murray, "Evaluation of a matched filter resolution recovery reconstruction algorithm for SPECT-CT imaging," *Nucl. Med. Commun.*, vol. 34, no. 3, pp. 240–248, 2013, doi: 10.1097/MNM.0b013e32835ce5b5.

[126] J. Tran-Gia *et al.*, "Standard Operating Procedure for MRTDosimetry Comparison

Exercise – Parts 1 & 4: Sensitivity I-131 and Lu-177."

[127] K. Ferreira, M. Lassmann, V. Smyth, J. Tran-gia, and J. Wevrett, "Protocol for Calibration of a Spect Camera for Traceable Quantitative Imaging. July 2019," 2019.

[128] R. Gadd *et al.*, "Protocol for establishing and maintaining the calibration of medical radionuclide calibrators and their quality control. Report No. 93," Teddington, Middlesex, 2006.

[129] W. Turner, "Deconvolution of septal penetration for assessment of quantification in I-131 planar imaging," King's College London, 2020.

[130] W. Zhao *et al.*, "Determination of gamma camera calibration factors for quantitation of therapeutic radioisotopes," *EJNMMI Phys.*, vol. 5, no. 8, pp. 1–16, 2018, doi: 10.1186/s40658-018-0208-9.

[131] A. Viduetsky and C. L. Herrejon, "Sonographic Evaluation of Thyroid Size: A Review of Important Measurement Parameters," *J. Diagnostic Med. Sonogr.*, vol. 35, no. 3, pp. 206–210, 2019, doi: 10.1177/8756479318824290.

[132] M. Stabin, "OLINDA 1.0 Documentation Package."

[133] A. Skanjeti *et al.*, "A simple and accurate dosimetry protocol to estimate activity for hyperthyroidism treatment," *Nucl. Med. Rev.*, vol. 18, no. 1, pp. 13–18, 2015, doi: 10.5603/NMR.2015.0004.

[134] The Stationery Office Limited, *The Medical Devices Regulations 2002*. UK, 2002, pp. 1–40.

[135] The Stationery Office Limited, *The Medical Devices (Amendment etc .) (EU Exit) Regulations 2020*, vol. 6. UK, 2020, pp. 1–234.

[136] R. A. S. Thomas *et al.*, "Radiotherapy reference dose audit in the United Kingdom by the National Physical Laboratory: 20 years of consistency and improvements," *Phys. Imaging Radiat. Oncol.*, vol. 3, pp. 21–27, 2017, doi: 10.1016/j.phro.2017.07.005.

[137] G. Distefano *et al.*, "A national dosimetry audit for stereotactic ablative radiotherapy in lung," *Radiother. Oncol.*, vol. 122, no. 3, pp. 406–410, 2017, doi: 10.1016/j.radonc.2016.12.016.

[138] D. J. Eaton *et al.*, "An external dosimetry audit programme to credential static and rotational IMRT delivery for clinical trials quality assurance," *Phys. Medica*, vol. 35, pp. 25–30, 2017, doi: 10.1016/j.ejmp.2017.02.012.

[139] V. Smyth, "Final publishable JRP report: HLT11, MetroMRT, Metrology for Molecular Radiotherapy v1.3," 2015. [Online]. Available: https://www.euramet.org/research-innovation/search-research-projects/details/project/metrology-for-molecular-radiotherapy.

[140] H. Hänscheid *et al.*, "Iodine biokinetics and dosimetry in radioiodine therapy of thyroid cancer: procedures and results of a prospective international controlled study of ablation after rhTSH or hormone withdrawal.," *J. Nucl. Med.*, vol. 47, no. 4, pp. 648–54, 2006, doi: 47/4/648.

[141] I. Kawrakow, D. Rogers, E. Mainegra-Hing, F. Tessier, R. Townson, and B. Walters, "The EGSnrc C++ class library. NRC Report PIRS-898 (rev A)," Ottowa, Canada, 2009.

[142] I. Kawrakow, "Accurate condensed history Monte Carlo simulation of electron transport. I. EGSnrc, the new EGS4 version," *Med. Phys.*, vol. 27, no. 3, pp. 485–498, 2000, doi: 10.1118/1.598917.

[143] K. Eckerman and A. Endo, “ICRP Publication 107. Nuclear decay data for dosimetric calculations,” *Ann. ICRP*, vol. 38, no. 3, pp. 7–96, 2008, doi: 10.1016/j.icrp.2008.10.004.

[144] B. R. B. Walters, I. Kawrakow, and D. W. O. Rogers, “History by history statistical estimators in the BEAM code system,” *Med. Phys.*, vol. 29, no. 12, pp. 2745–2752, 2002, doi: 10.1118/1.1517611.

[145] M. Andersson, L. Johansson, K. Eckerman, and S. Mattsson, “IDAC-Dose 2.1, an internal dosimetry program for diagnostic nuclear medicine based on the ICRP adult reference voxel phantoms,” *EJNMMI Res.*, vol. 7, pp. 1–10, 2017, doi: 10.1186/s13550-017-0339-3.

[146] “IDAC Dose.” https://www.idac-dose.org/#/idac-dose (accessed Jun. 10, 2021).

[147] DosiTest, “DosiTest Project.” http://www.dositest.fr (accessed Jun. 24, 2021).

[148] G. Kayal *et al.*, “Generation of clinical 177Lu SPECT/CT images based on Monte Carlo simulation with GATE,” *Phys. Medica*, vol. 85, no. May, pp. 24–31, 2021, doi: 10.1016/j.ejmp.2021.04.002.

[149] M. P. Garcia *et al.*, “TestDose: A nuclear medicine software based on Monte Carlo modeling for generating gamma camera acquisitions and dosimetry,” *Med. Phys.*, vol. 42, no. 12, pp. 6885–6894, 2015, doi: 10.1118/1.4934828.

Appendix 1 - Flow charts for the planned dosimetry technique.

Bone marrow and blood dosimetry – blood sample measurements

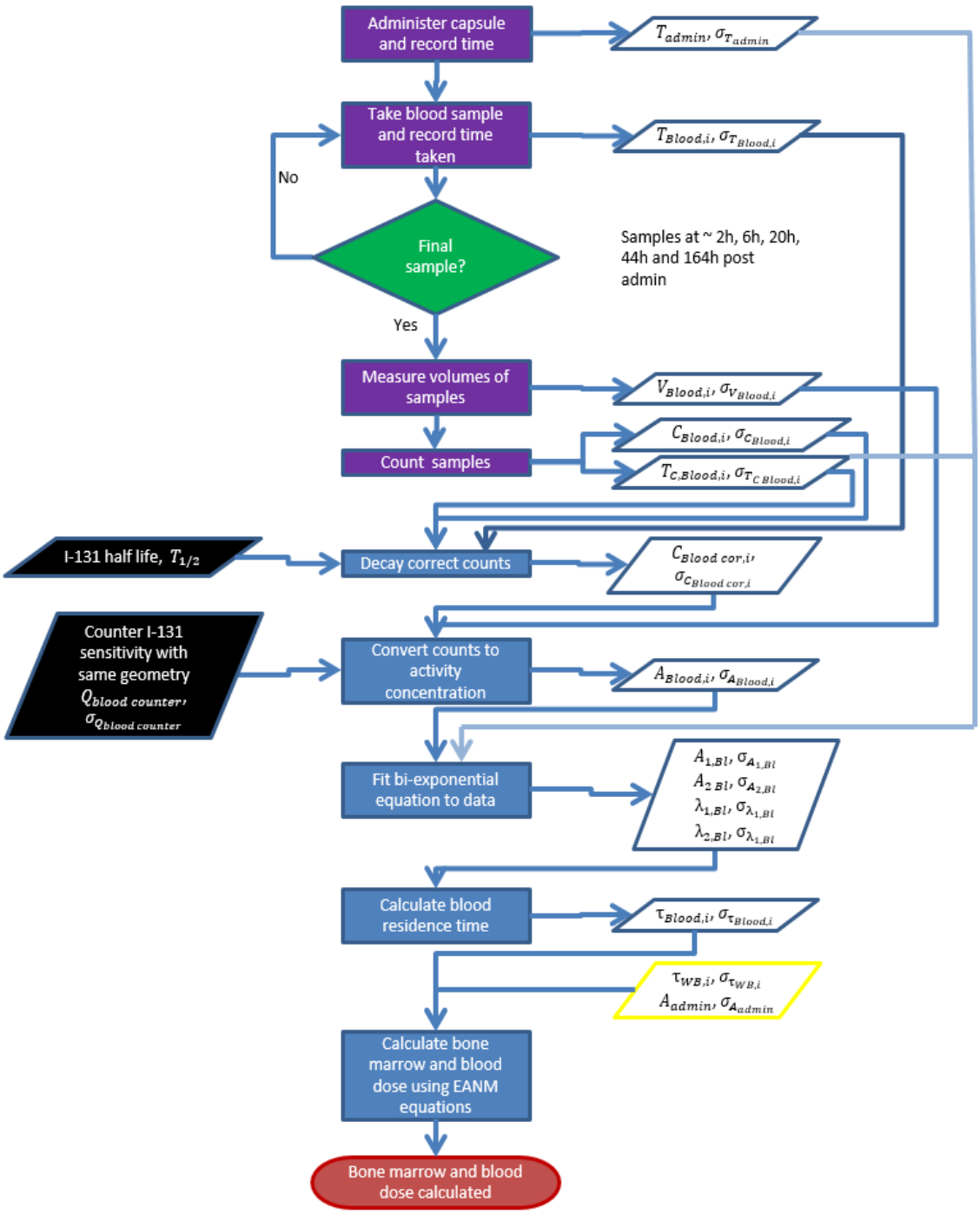

Bone marrow and blood dosimetry – whole body retention measurements

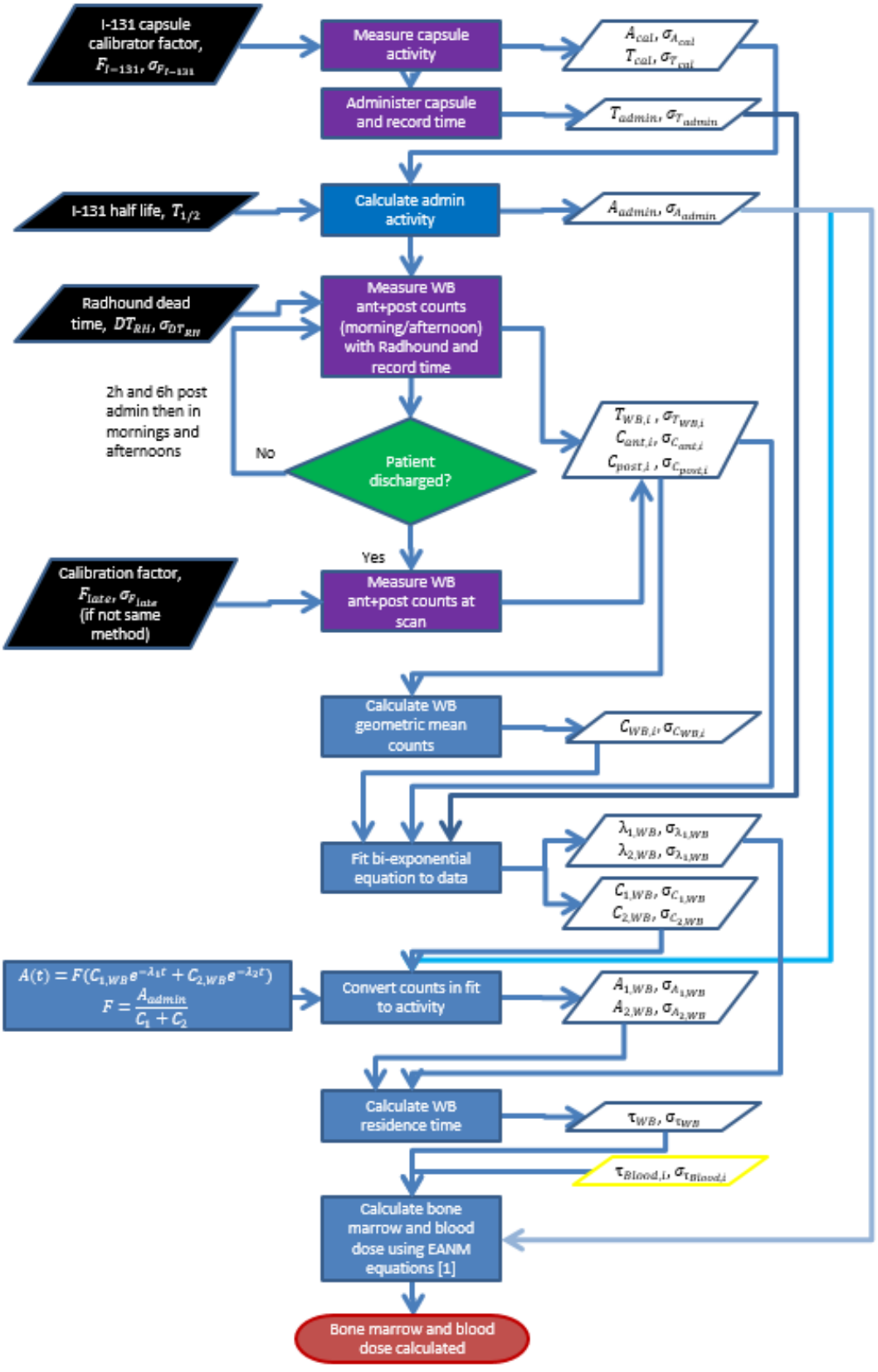

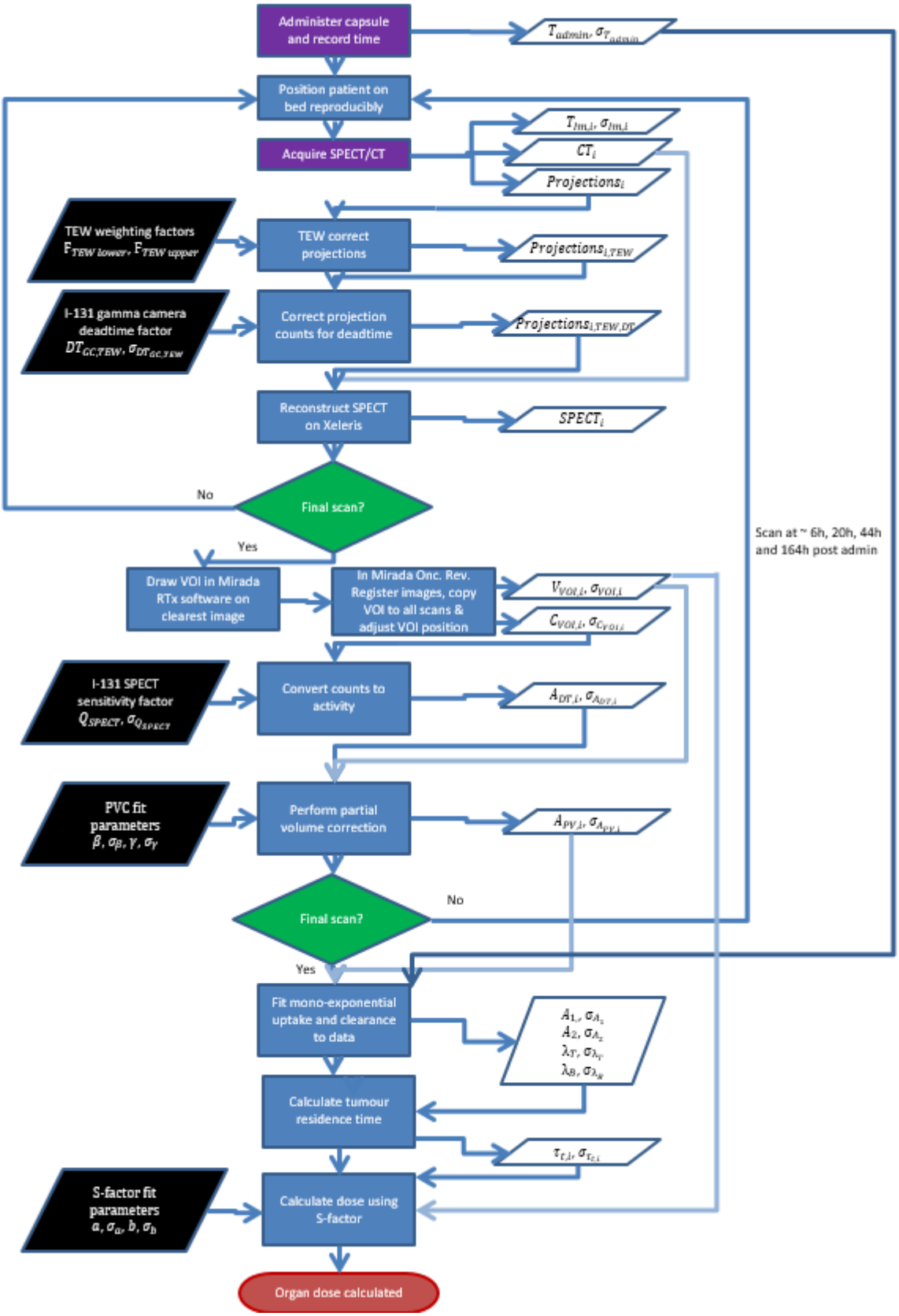
Administer capsule and record time
$T_{admin}, \sigma_{T_{admin}}$
Position patient on bed reproducibly
Acquire SPECT/CT
$T_{Im,i}, \sigma_{Im,i}$
CT_i
$Projections_i$
TEW weighting factors $F_{TEW\ lower}, F_{TEW\ upper}$
TEW correct projections
$Projections_{i,TEW}$
I-131 gamma camera deadtime factor $DT_{GC,TEW}, \sigma_{DT_{GC,TEW}}$
Correct projection counts for deadtime
$Projections_{i,TEW,DT}$
Reconstruct SPECT on Xeleris
$SPECT_i$
Final scan?
No
Yes
Scan at ~ 6h, 20h, 44h and 164h post admin
Draw VOI in Mirada RTx software on clearest image
In Mirada Onc. Rev. Register images, copy VOI to all scans & adjust VOI position
$V_{VOI,i}, \sigma_{VOI,i}$
$C_{VOI,i}, \sigma_{C_{VOI,i}}$
I-131 SPECT sensitivity factor $Q_{SPECT}, \sigma_{Q_{SPECT}}$
Convert counts to activity
$A_{DT,i}, \sigma_{A_{DT,i}}$
PVC fit parameters $\beta, \sigma_\beta, \gamma, \sigma_\gamma$
Perform partial volume correction
$A_{PV,i}, \sigma_{A_{PV,i}}$
Final scan?
No
Yes
Fit mono-exponential uptake and clearance to data
A_1, σ_{A_1}
A_2, σ_{A_2}
$\lambda_T, \sigma_{\lambda_T}$
$\lambda_B, \sigma_{\lambda_B}$
Calculate tumour residence time
$\tau_{t,i}, \sigma_{\tau_{t,i}}$
S-factor fit parameters a, σ_a, b, σ_b
Calculate dose using S-factor
Organ dose calculated

Appendix 2 – HSST C1 Innovation Proposal (March 2018)

Implementation of Dosimetry for Differentiated Thyroid Cancer for Planning and Verification of Treatment

Executive Summary

This innovation proposal evaluates the feasibility of implementing a routine clinical dosimetry service for radioiodine (I-131) therapies for thyroid cancer, both for personalising therapy treatments and for post-therapy verification of the dose received during therapy. Currently, fixed amounts of I-131 are given to patients, with patients having their first treatment receiving 1.1GBq if they are low risk and 3.7GBq if they are high risk, followed by 5.5GBq administrations if repeat treatments are required. This works well for most patients and typically does not cause significant damage to areas which can be sensitive to radiation such as the bone marrow[1]. However, at RSCH it has been found that 15% of the low risk patients and 45% of the high-risk patients have to come back for additional treatments, frequently due to inadequate treatment of any remaining thyroid tissue or metastases. Dosimetry involves calculating the energy deposited in the desired treatment areas and organs at risk. For I-131 therapy this would involve measuring the uptake and clearance of I-131 in the treatment areas and organs which are most likely to be damaged by the radiation. It can be used to decide on the optimal amount of I-131 to give to a patient to reduce their likelihood of retreatments while minimising side effects and may help to predict if a patient is likely to need retreatments. Currently dosimetry is not performed in the UK for I-131 thyroid carcinoma therapy but verification of exposures is now required under the new IR(ME)R 2017 legislation[2]. There is no consensus on the best methods to perform this dosimetry so published guidelines and relevant literature have been used to develop an implementation plan, involving calibration measurements, determination of the best data processing methods and changes to current clinical databases. Dosimetry has been standard practice for planning and verification of treatments using external beam radiotherapy and in the era of personalised medicine it is time that we started performing dosimetry to I-131 patients so we can start delivering the best care possible. As dosimetry is not currently performed in the UK for patients with thyroid cancer this will be an innovative project which could make a real difference to patients' lives, enabling retreatment rates to be reduced while gathering more data on doses received to target

areas and the likelihood of retreatments being required so treatments can be optimised further.

Background

Radioactive iodine (I-131) is used to treat differentiated thyroid cancer and is taken up within thyroid cells to produce thyroid hormones in the same way as dietary iodine. Currently empirical activities of 1.1GBq and 3.7GBq are administered for first treatments in patients who are low and high-risk respectively. An activity of 5.5GBq is administered for repeat treatments if required. Patients administered with the same amount of activity have been found to have large variations in the amount of uptake and clearance within thyroid tissue and hence have different treatment success rates[3], with retreatment being required in some cases. For patients at the Trust having their first treatments in 2013 and 2014, 15% (4/26) of the 1.1GBq patients required a re-treatment (mean=1.15 treatments), while 45% of the 3.7GBq patients (25/56) required retreatments, with four having three retreatments, one having four retreatments and one having five retreatments by the end of 2017 (mean=1.61 treatments).

Dosimetry involves calculating the energy deposited by the radiation per unit mass of tissue and is commonly used in radiotherapy to determine the method which will give the desired cell kill to the tumour, while sparing organs which can be easily damaged by the radiation. Despite the benefits dosimetry could bring for patients and its routine use for optimising external beam radiotherapy, it not currently performed in the UK for I-131 thyroid cancer treatments due to factors such as the complexity, lack of resources and lack of standardisation [4,5]. However the new Ionising Radiation (Medical Exposure) Regulations 2017 requires exposures to be individually planned and exposures to be verified[2] so gives increased incentive to start performing dosimetry. The current method of planning the activity to administer based on the risk stratification of the patient could be taken to meet the requirement of individually planning exposures. However, a more tailored approach has been recommended in which the maximum amount of I-131 which could be administered without causing damage to the bone marrow (the organ most likely to be damaged) is estimated from patient measurements using a small amount of I-131 before therapy[6]. A study comparing patients administered with empirical activities against those with activities based on dosimetry found similar retreatments rates to RSCH for high risk patients (mean=1.59), while using dosimetry reduced the retreatment rates

to 1.41 [1]. Performing "verification" dosimetry, where the dose to the thyroid and radiosensitive organs is calculated could inform clinicians of the likelihood of the patient needing retreatment and long term follow up of these patients could help determine the optimal tumour dose required.

While there are guidelines by groups such as the European Nuclear Medicine Society and Medical Internal Radiation Dose Committee on how to perform dosimetry for radionuclide therapies, there is no consensus on the best method and as dosimetry is not currently performed in the UK for this patient group the application would be innovative. Methods based on published guidelines and literature are outlined below, focussing on the dose to the target thyroid tissue and the bone marrow which is typically the key organ at risk of damage from I-131 therapy. If dosimetry can be practically implemented within our Trust, then the knowledge gained could be used to assist other hospitals in implementing dosimetry, improving patient lives and our knowledge of I-131 treatment throughout the NHS.

Proposed Options

Proposed options are given below and a summary of their costs is given in the Appendix. Dosimetry options are given for high risk 3.7GBq patients as they are the highest cost group who are most likely to require repeat treatments and so would benefit more from dosimetry. In addition to this they are also more likely have longer inpatient stays following therapy, allowing for more dosimetry measurements to be taken at a reduced cost. Oncologist stakeholder engagement found that while they would like dosimetry for all I-131 patients, they agreed that the focus should initially be on the 3.7GBq patients.

Option 1 – do nothing

With this method no additional staffing or equipment would be needed, however doses to the thyroid tissue and organs at risk are not calculated. Patients referred for radioiodine therapies typically come to the ward on the Saturday and Sunday for thyrogen injections prior to a Monday treatment, to increase I-131 uptake in the thyroid cells. They have blood tests to check their thyroid, kidney and bone marrow function as well as test for pregnancy if required and are reviewed by the ward doctors. Following the I-131 administration, the patients must stay in shielded isolation rooms to reduce potential doses to their family and members of the public. Administration is performed by a physicist, who also performs external probe measurements twice a day to estimate the

I-131 clearance and discharge the patient when the estimated dose to the public would be sufficiently low. SPECT/CT and whole body gamma camera imaging is performed on the Monday following therapy to visualise the uptake of the I-131 and assess if any future treatments are required

Option 2 – whole body and bone marrow post therapy dosimetry

The bone marrow is typically the organ which limits the amount of radioiodine that can be administered, therefore measuring this could give clinicians an idea of whether the patient could tolerate higher activities of I-131. Hence this data would be useful even if it is not used to plan treatments and it is thought that this would be the minimum level of post therapy verification dosimetry that could be performed to meet the new regulations. Literature suggests that bone marrow dosimetry can be performed using blood sampling and whole-body measurements. Additional blood samples would need to be taken from the patient at regular time points and the amount of radioiodine in the samples measured using a gamma counter, which the department already owns. The retention measurements currently performed to estimate when a patient could be discharged following therapy could be used to estimate the whole-body contribution to bone marrow dose and give an estimate of the total dose that the patient receives. The optimal time points for these measurements has not been fully investigated, however they are most commonly performed at 2, 6, 24, 48, 72 and 96 hours post administration. 3.7GBq and 5.5GBq patients are typically discharged on Wednesdays following a Monday treatment, therefore blood sample and probe measurements could feasibly be performed at 2, 6, 24 and 48 hours post administration while they are an inpatient. Additional late time point blood sample and retention measurements could be taken when the patient comes for gamma camera imaging at around 120 hours post administration. The measurements made could also be used to calculate whole body dose.

Option 3 - whole body, bone marrow, thyroid and organs at risk post therapy dosimetry

This would be the same as Option 2 but with 3 additional SPECT/CT acquisitions of the thyroid and any metastases at 6, 24, 48 hours post administration in addition to the acquisitions normally performed at 120 hours post administration. A clinician would be required to outline the areas of interest on a SPECT/CT scan, taking an estimated 30 minutes and these regions would need to be copied over to the other imaging time points by a physicist, with the activity at each time point calculated using the measured counts data. The measured activities at each time point would then be inputted into specialist

software to calculate the dose to the thyroid. The previously open source OLINDA/EXM 1.0 software is already available in the department and can be used to calculate the average dose in the region to a "standard man". More patient specific dosimetry can be performed at a voxel level if specialist software was purchased and this could also enable the images to be more accurately co-registered and 3D dose distributions calculated, however this would add an estimated additional cost of around £200 per patient and so cannot be recommended at present. Prior to implementation of Option 3, a calibration process would need to be performed by a physicist to enable the conversion of image counts data into radioiodine activity.

Option 4 – pre-therapy bone marrow dosimetry for treatment planning with whole body, bone marrow, thyroid and organs at risk post therapy dosimetry

This would be the same as for Option 3, but a few weeks prior to the planned therapy date the patient will receive two thyrogen injections followed by a small amount of I-131 and dosimetry as described in Option 2 will be performed to determine the amount of I-131 to be administered for therapy. The method of performing retention measurements would need further investigation prior to implementation but it is thought that this could be performed using the Radhound contamination monitors and lead shielding already available in the department. For this option, more optimal treatments could be administered and the treatment delivered could be verified.

Discussion

A detailed costing model of each option is presented in the Appendix. Option 1 (do nothing) has an estimated cost of £4,224 and requires no additional staffing but does not provide dosimetry information, therefore RSCH may be contravening IRMER17[2] and so doing nothing cannot be recommended. Option 2 requires the addition of blood sampling, which can be easily incorporated with the current staffing and equipment, with a small additional cost of £23.90 for consumables. The additional blood sampling is an extra set of procedures that patients would have to undergo, however 6 patients were surveyed to get their feedback on the implementation of dosimetry and all stated that they would like dosimetry to be performed and 5 stated that they would be prepared to have additional blood samples taken to do this (one was experiencing pain during therapy but said they would be happy to have blood samples taken if they weren't in pain). Option 3 requires 3 additional SPECT/CT images and an estimated additional 2 hours processing time by a physicist and 30 minutes processing time for a clinician but would

also allow the dose to the target area to be calculated. Stakeholder engagement with the Nuclear Medicine physicists found that they would be prepared to absorb the additional 4 hours a week (assuming both I-131 isolation rooms are used) to process the dosimetry data at the expense of their research as one staff member suggested “dosimetry is the future of Nuclear Medicine therapies, something we all feel should be done and are prepared to lose some of our development work time for”. Therefore, additional physics staff should not be required. It should also be noted that once staff are more familiar with the processing methods the time taken to do this should decrease. Stakeholder engagement with Nuclear Medicine imaging staff found that once the new SPECT/CT scanner is installed they would be happy to scan these patients in the mornings after quality control testing is performed while they are waiting for tracer uptake from their standard imaging patients, which would result in a low additional cost to the Trust. Therefore, while Option 3 initially appears to be around £650 more expensive than Options 1 and 2 due to staff time and imaging costs, the actual cost to the Trust is likely to not be substantially different. Option 4 requires an additional diagnostic administration of 30MBq I-131 (~£80/treatment) for estimation of the bone marrow dose, additional thyrogen injections to stimulate the I-131 uptake (~£699/treatment), with the patients attending the hospital for additional blood samples and whole-body retention measurements. Options 3 and 4 would result in additional CT and I-131 dose to the patient, however stakeholder engagement with the thyroid oncologists found that they felt the risk from the additional radiation dose was low for these patients and the benefit of performing dosimetry would outweigh the risks. Including the expected lower retreatment rate Option 4 has an estimated cost of £5,575 which is around £1,350 more Option 1 (or £998 more if staff time and imaging costs are removed), with the difference in price primarily due to the additional administration of thyrogen for pre-therapy dosimetry. Option 4 appears to be substantially more expensive however, due to the innovative nature of the proposal a full QUALY assessment cannot be performed, but small-scale studies have shown benefits such as 70% reduction in disease progression in dosimetry-based treatment compared to empirical methods as well as higher likelihoods of obtaining complete response and survival[1]. Therefore Option 4 is recommended as it is an innovative method with potential benefits for patients in terms of both a reduction in retreatment rates and increased survival.

Implementation plan for preferred option (Option 4)

The majority of the development work required to implement the preferred option would be performed by a Band 8a physicist on the Higher Scientist Specialist Training scheme, as part of their one day a week training allocation and so would not require additional staffing costs or take away support for the routine clinical service. Whole body and bone marrow dosimetry implementation would require some additional retention measurements in the Nuclear Medicine for therapy planning and during the therapy after patients have been discharged. The Geiger detectors in the ceiling of the isolation rooms normally used for retention measurements cannot easily be moved and additional Geiger detectors are not available in the department. However, there are a number of Radhound contamination monitors in the department and while they would typically saturate at the high dose rates near I-131 patients, it is thought that using lead already in the department to attenuate the photons could allow these detectors to be used. Measurements would need to be performed after the standard Geiger detector measurements to check for saturation and produce calibration factors. It is expected that this would take around 3 days with a Band 8a HSST physicist supervising a physics trainee, at no additional cost to the Trust. If this could not be performed in a reproducible, effective manner then gamma camera calibration could be investigated or an additional Geiger detector would need to be purchased. Performing measurements at 2, 6 hours post administration would require the administration to be performed in the morning, which currently doesn't occur however discussions are already underway with the oncologists to streamline the process and this is expected to allow for morning administrations in the majority of cases. If the patient could not be treated in the morning, they would have to wait to be treated the next day. The current clinical database for radioiodine therapies would also need to include additional fields for inputting blood sampling measurements and the chosen method for additional retention measurements. The Nuclear Medicine department has a year in industry computing student who is likely to be able to do this in a couple of days as part of his role at no additional cost to the Trust. The current spreadsheet for radioiodine therapies would need to be adapted to incorporate the additional blood and retention measurements as well as calculate the whole body and bone marrow dose – literature already exists on how to calculate the dose form this data and adapting the spreadsheet could be done in a day by a Band 8a physicist on HSST.

In order to implement thyroid and other organ at risk dosimetry, the following calibrations/corrections for SPECT/CT would have to be performed for more accurate

patient activity estimation: dead-time correction, collimator-detector response correction, partial volume effect correction, and counts to activity conversion. A deadtime model of the GE Optima 640 system has already been produced as part of the SEL-I-METRY trial, where a cylinder phantom was filled with increasing amounts of I-131 up to 2.7GBq of I-131 and imaged using fast mode at multiple time points as the source underwent radioactive decay. The department has GE Evolution SPECT reconstruction software which can be used to correct for the changing resolution with collimator distance. However, it has not been used within this department and so optimisation of the SPECT reconstruction parameters would be required to give the optimum balance of recovery of the source distribution, while reducing noise amplification. A number of reconstructions would be required on phantom and patient images and it is expected that this would take around 4 days by a Band 8a physicist on HSST, with assistance from a physics trainee. Partial volume effect correction accounts for the underestimation in activity that can occur with small volumes due to the low spatial resolution of gamma camera systems. The elliptical image quality phantom containing spheres of different diameters would need to be filled with around 37 MBq of I-131, costing £80. Methods of correction would be investigated by a Band 8a physicist on HSST. There are a number of different methods that could be used, with differing levels of accuracy, with the simplest and quickest to implement being using the phantom to create volume-based correction factors. As this does not involve the use of open source non-CE marked software or the creation of complex local software that would require extensive local validation, the volume-based lookup tables will be used initially and are expected to take around 2 days to create by a Band 8a physicist on HSST. Counts to activity conversion can also be performed using the acquisition of the image quality phantom required for partial volume correction and is expected to take around 2 days to create by a Band 8a physicist on HSST. Updating the existing patient database and spreadsheet to be used as a medical device for dosimetry would also require extensive local validation which could be time consuming. The key barrier to implementation is likely to be access to the SPECT/CT scanner for patient scans, which currently has a high workload. However, the department is planning to get an additional SPECT/CT scanner which should enable this to be performed.

References

1. Klubo-Gwiezdzinska, J. *et al.* Efficacy of dosimetric versus empiric prescribed activity of 131I for therapy of differentiated thyroid cancer. *J. Clin. Endocrinol. Metab.* **96,** 3217–3225 (2011).
2. The Stationary Office. The Ionising Radiation (Medical Exposure) Regulations 2017. (2018).
3. Flux, G. D. *et al.* A dose-effect correlation for radioiodine ablation in differentiated thyroid cancer. *Eur. J. Nucl. Med. Mol. Imaging* **37,** 270–275 (2010).
4. McGowan, D. R. & Guy, M. J. Time to demand dosimetry for molecular radiotherapy? *Br. J. Radiol.* **88,** 3–5 (2015).
5. EANM Internal Dosimetry Task Force. Internal Dosimetry Task Force report on treatment planning for molecular radiotherapy: potential and prospects. (2017).
6. Lassmann, M., Reiners, C. & Luster, M. Dosimetry and thyroid cancer: The individual dosage of radioiodine. *Endocr. Relat. Cancer* **17,** 161–172 (2010).

Appendix

Table 1. Estimated I-131 therapy costs for Options 1 to 4 for high risk patients receiving 3.7MBq I-131 on their first treatment and 5.5GBq on future treatments. The second treatment patient averaged cost is taken to be the cost for a repeat treatment multiplied by the likelihood of retreatment (taken from Klubo-Gwiezdzinska et al. (2011)[1]).

		Option 1	Option 2	Option 3	Option 4
First Treatment	Staff cost	£ 310.36	£ 342.37	£ 434.95	£ 497.62
	Consumables cost	£ 4.96	£ 19.80	£ 19.80	£ 34.64
	Medicines cost	£ 818.91	£ 818.91	£ 818.91	£ 1,597.90
	Imaging cost	£ 150.32	£ 150.32	£ 450.97	£ 450.97
	Inpatient stay cost	£ 1,329.00	£ 1,329.00	£ 1,329.00	£ 1,329.00
	Total cost	£ 2,613.55	£ 2,660.40	£ 3,053.63	£ 3,910.13

Likelihood of a retreatment		61%	61%	61%	61%
Second treatment patient averaged cost	Staff cost	£ 189.32	£ 208.85	£ 265.32	£ 209.00
	Consumables cost	£ 3.02	£ 12.08	£ 12.08	£ 14.55
	Medicines cost	£ 515.93	£ 515.93	£ 515.93	£ 693.70
	Imaging cost	£ 91.70	£ 91.70	£ 275.09	£ 189.41
	Inpatient stay cost	£ 810.69	£ 810.69	£ 810.69	£ 558.18
	Total cost	£ 1,610.66	£ 1,639.24	£ 1,879.11	£ 1,664.83
Overall patient averaged cost	Staff cost	£ 499.69	£ 551.22	£ 700.27	£ 706.62
	Consumables cost	£ 7.98	£ 31.87	£ 31.87	£ 49.19
	Medicines cost	£ 1,334.84	£ 1,334.84	£ 1,334.84	£ 2,291.60
	Imaging cost	£ 242.02	£ 242.02	£ 726.06	£ 640.37
	Inpatient stay cost	£ 2,139.69	£ 2,139.69	£ 2,139.69	£ 1,887.18
	Total cost	£ 4,224.22	£ 4,299.65	£ 4,932.73	£ 5,574.96

Appendix 3 – DClinSci List of AMBS A Units and Medical Physics B Units Together with Assignments

AMBS – A Units		
Unit title	**Credits**	**Assignment word count**
A1: Professionalism and professional development in the healthcare environment	30	Practice paper – 2000 words A1 – assignment 1 – 1500 words A1 – assignment 2 – 4000 words
A2: Theoretical foundations of leadership	20	A2 – assignment 1 – 3000 words A2 – assignment 2 – 3000 words
A3: Personal and professional development to enhance performance	30	A3 – assignment 1 – 1500 words A3 – assignment 2 – 4000 words
A4: Leadership and quality improvement in the clinical and scientific environment	20	A4 – assignment 1 – 3000 words A4 – assignment 2 – 3000 words
A5: Research and innovation in health and social care	20	A5 – assignment 1 – 3000 words A5 – assignment 2 – 3000 words
Medical Physics – B Units		
B1: Medical Equipment Management	10	2000 word assignment
B2: Clinical and Scientific Computing	10	2000 word assignment
B3: Dosimetry	10	Group presentation 1500 word assignment
B4: Optimisation in Radiotherapy and Imaging	10	Group presentation 1500 word assignment
B6: Medical statistics in medical physics	10	3000 word assignment
B8: Health technology assessment	10	3000 word assignment
B9: Clinical applications of medical imaging technologies in radiotherapy physics	20	Group presentation 2000 word assignment
B10b: Assessment of Image Quality	10	1500 word report
B10f: Radiation Protection Advice	10	1500 word report/piece of evidence for portfolio
B10g: Radiation Waste Advice	10	1500 word report/piece of evidence for portfolio
Generic B Units		
B5: Contemporary issues in healthcare science	20	1500 word assignment + creative project
B7: Teaching Learning Assessment	20	20 minute group presentation